FEDERAL HIGHWAY ADMINISTRATION
TURNER-FAIRBANK HIGHWAY RESEARCH CENTER REPORT

Finite Element Modeling of I-35W Bridge Collapse

Final Report

Justin M. Ocel, PhD
Professional Service Industries (PSI)

William J. Wright, PhD
Federal Highway Administration

OCTOBER 2008

TABLE OF CONTENTS

LIST OF FIGURES

LIST OF TABLES

ACKNOWLEDGEMENTS

The authors would like to thank those whom assisted in the development of this work as it could not be done in a timely fashion without their efforts. Early in the development of the global model Gary Greene calculated all the gross and net section properties of the truss members, Fassil Beshah constructed solid element models to determine the structural effect of access holes in the box sections, and Professor Don White provided an external peer review. A significant effort was also performed by Marshall Davis and Gary Greene in determining the steel weight by reviewing over 400 pages of shop drawings.

CHAPTER 1. INTRODUCTION

The Federal Highway Administration (FHWA) undertook this modeling effort to assist the National Transportation Safety Board (NTSB) investigation into the August 1, 2007 collapse of the I-35W bridge over the Mississippi River in Minneapolis, Minnesota. All modeling at the FHWA was performed at the Turner-Fairbank Highway Research Center using Abaqus version 6.6 and 6.7 software. In total, seven separate models were constructed at the FHWA to investigate different aspects of the failure. In addition, several models were constructed independently by other parties to the investigation.

The I-35W bridge consists of a three span (266 feet-456 feet-266 feet) continuous Warren deck truss spanning across the Mississippi River. The north approach is made from a three span continuous multi-girder bridge abutting to a three span continuous voided slab span whereas the south approach is made from a two-span butting to a three-span continuous, multi-girder structure. Both approaches rest upon the back spans of the deck truss. The total length of the approaches and deck truss is 1907 feet.

The models are based primarily on the original design plans and shop drawings for the bridge.[1,2] With one exception that will be described later, the NTSB was able to verify that the bridge was correctly built according to the original shop drawings. Therefore there is no substantial difference between the original as-designed and as-built structures. Several retrofit projects were performed during the service life of the bridge that significantly altered the concrete deck and crash barrier details. For the purpose of this investigation, models were constructed to analyze the bridge at two points in its life as follows:

1) **Designed (1965)** These models were constructed with the geometry based entirely on the design plans for the bridge. The only exception noted at the wreckage site was the top and bottom chords of the floor trusses were ultimately not fabricated as they were designed. Instead, the fabricator opted to carry the larger W-sections across the entire width of the floor truss between the main trusses rather than transition to smaller shape sizes with shop splices. Typical designer assumptions were used for the steel and concrete densities. The primary purpose of these models was to verify the member axial forces used in design.

2) **As-Built (2007)** These models were constructed to analyze the bridge as it existed just prior to collapse. The original bridge model was modified to reflect all changes made during the service life of the bridge. Measurements of deck and crash barrier geometry and weight were included in these models.

The FHWA developed six separate "Global" finite element models to study the structural response of the bridge. To promote computational efficiency, separate models were constructed for the North Approach Spans, South Approach Spans, and Main Truss Spans. Each of the three models had two configurations corresponding to the designed conditions assumed in 1965 and what really existed in 2007. All steel members were represented by beam elements connected together at the appropriate geometric location in the bridge. These models were constructed to add weight and loading in steps that simulate the construction sequence of the bridge.

A seventh "Detailed" model was constructed to add connection details at the U10 and L11 locations in both the east and west trusses. These corresponded to areas where gusset plate failures were observed in the wreckage. Detailed shell element assemblies were constructed of these joints where each plate was discretely modeled and connected together at fastener locations. These detailed joint assemblies were then imbedded in the As-Built (2007) main truss global model. The forces in the members framing into the detailed joints were therefore automatically determined from the global model.

In addition to the FHWA models, several other parties constructed independent models to look at various aspects of bridge performance. Comparisons are made between these models and the FHWA models later in this report as appropriate. The following models will be henceforth referred to in this report:

- **NTSB Model**
  The NTSB is performing a parallel modeling effort to develop an enhanced understanding of detail elements that failed during the bridge collapse. Starting with the As-Built (2007) global model developed by the FHWA, detailed solid models are being imbedded at the failure locations to study various aspects of the failure. The FHWA and NTSB teams interacted significantly in this effort, but the results are being independently documented in a separate report.

- **BSDI Model**
  Bridge Software Development Inc. (BSDI) was contracted by the FHWA to model the Designed (1965) bridge and to verify the original design loads for the bridge. The model geometry was independently constructed from the design and shop drawings using somewhat different assumptions and modeling techniques. The BSDI proprietary software was utilized for this purpose. Comparisons were made between this model and the FHWA models to help calibrate the dead load weight of the structure. The BSDI model was also able to generate live-load force envelopes using the truck loading model used by the original bridge designers.

- **URS Model**
  URS Corporation performed a detailed finite element modeling project on the I-35W bridge in 2006 for the Minnesota Department of Transportation (Mn/DOT). The primary purpose was to perform a fatigue and redundancy evaluation of the structure. Comparisons were made to these results as appropriate.

- **WJE Model**
  Wiss Janney Elstner, Assoc. (WJE) is conducting an independent modeling effort under sponsorship of Mn/DOT. Results from this effort are not available for inclusion in this report at the time of writing.

CHAPTER 2. FHWA MODEL DESCRIPTION

The primary FHWA global models considered only the three-span deck truss portion of the bridge. Both the north and south approach span sections of the bridge were connected to the deck truss through bearings at the ends of the truss. Post-collapse inspections performed by FHWA and NTSB personnel found the reaction bearings of the approach spans to be in generally good working order. The approach spans apply their load to the main truss span through two rocker bearings at each end of the main truss at locations U0 and U0'. Therefore each approach span could be removed from the main truss model, modeled independently, and integrated into the main truss model as point loads and simple springs to represent the stiffness of the approach span. This greatly reduces the size of the bridge model and allows all of the available computing power to be focused on details in the deck truss. Both of the approach spans abutting the deck truss consisted of multi-span, continuous girder units. The forces applied to the deck truss through the bearings are therefore indeterminant and depend on the structural response of the approach span unit. To accurately predict these reactions, separate models were developed to accurately derive the equivalent point loads and springs. This effort required four separate models to obtain both the Designed (1965) and As-Built (2007) conditions for both the north and south approach spans

ACCUMULATION OF LOADING

Abaqus has the advantage of running a multi-stepped analysis where elements can be added/removed and boundary conditions can be changed where the stresses/forces from the preceding step are considered to be initial stresses in the current step. An eight-step analysis was originally used to model the accumulation of loads through the construction sequence of the bridge. This starts with the original steel erection, four concrete deck pour sequences, application of barriers, change in deck thickness and barriers through retrofits, and finally the application of construction loading. The internal member forces produced by the four-step deck pour sequence were essentially the same as those produced by assuming all elements had instant gravity. Therefore, the modeling sequence was reduced to the following four steps:

- **Step 1**
  The concrete deck elements were deactived from the model and gravity was turned on for all the steel elements. Point loads were applied to the stringer elements to represent the weight of the wet concrete deck. Four vertical point loads are added at the ends of the main truss cantilevers representing the reactions from the two approach spans. Ideal boundary conditions (pins and rollers) are assigned to the eight nodes of the main truss intersecting the tops of the Piers 5, 6, 7, and 8.

- **Step 2**
  The point loads on the stringers were deactivated and the concrete deck elements were activated. The four vertical point loads at the ends of the main truss cantilevers were carried over from Step 1. In addition, vertical line loads are added to the edges of the

slabs representing the weight of the interior and exterior barriers. The boundary conditions are retained from Step 1.

- **Step 3**
  Vertical distributed pressure is applied to the all the concrete deck elements representing the additional concrete thickness that occurred through the life of the bridge. The line loads at the edge of the slab were altered to represent the weights of the modified barriers that were changed in 1999. These same loads were applied to the approach span models and reaction forces applied at the truss cantilevers were modified.

- **Step 4**
  The construction and traffic loads are applied to the truss and approach spans based on the NTSB 07-115 document.[4] The ideal boundary conditions were switched off and fixed boundary conditions were added to the foundation level of the piers. In addition, the bases of the trusses were pin-connected to the pier tops. This assumes the bearings were frozen but still allowed to translate by being restrained by the pier stiffness.

BARRIERS

The exterior and interior median barriers contain a significant amount of concrete and cannot be neglected when calculating the dead load of the main truss. Figure 1 shows a schematic of the originally designed exterior barriers which were calculated to be **516 lb/ft**. These barriers were upgraded by removing the steel guardrail and adding an additional concrete wall. The original exterior barrier was never removed and the concrete deck thickness increased around the original barrier. Since the deck thickness increased for the entire deck area in the model via pressure distributions, a weight adjustment for the modified exterior barrier was required to avoid double-counting concrete weight. Therefore, part of the parapet cross-section had to be ignored. Shown in Figure 2 is the exterior parapet present in the As-Built (2007) bridge, specifically showing the hatch marks not extending through the entire parapet cross-section. This resulted in a total weight of **778 lb/ft**.

The interior median was originally just a curb with a steel post and guardrail. This is shown in Figure 3 and was calculated to be **507 lb/ft**. In 1999, this median was completely replaced with two Jersey-style barriers with a pre-cast top. This was done to comply with federal crash regulations and because of the corrosion issues caused by the open longitudinal joint in the original design allowing chlorides to drip onto the floor trusses. The modified design shown in Figure 4 was much heavier at **1055 lb/ft**.

CONCRETE DECK THICKNESS

WJE retrieved cores from the deck after the collapse and produced a report outlining the thickness and positions of the cores. This data was analyzed at TFHRC to look for trends in the data. No systematic trend in deck thickness variation could be determined related to location in the bridge. Since each two-lane portion of the bridge deck was independently resurfaced between expansion joints it was assumed that the deck thickness is constant for each of these regions. As shown in Figure 5, a uniform deck thickness was calculated for each region. Any deck thickness over 6.5 inches was applied in Step 3 as a pressure load to the deck elements. The resulting deck still has the same stiffness as the original 6.5 inch deck, but since the deck is not fully composite with the stringers this has no effect on load distribution in the bridge. Few cores were taken from the approach span so it was assumed the deck thickness increased uniformly to 8.5 inches on each of the approach spans.

WALKWAYS

The catwalk weight was determined through inspection of the shop drawings. The open steel grating was only specified on the construction plans to have a minimum weight of 12.2 lb/ft^2. To remove the uncertainty of the true weight of the steel grating, a piece was shipped back from Minneapolis to TFHRC. What was delivered had plan dimensions of 20.125 inches by 36.0625 inches and had a weight of 67.1 pounds. This works out to an area weight density of 13.31 lb/ft^2. The shop drawings detail two types of walkways, one that runs in the longitudinal direction of the truss and three transverse walkways at Floor Truss 8, 10, and 8'. The longitudinal walkway with grating weighed **108.6 lb/ft**. The three transverse walkways were a heavier **117.4 lb/ft**.

The transverse walkway loads were applied to the bottom chords of the three floor trusses as distributed line loads. The longitudinal walkway loads were applied as single point loads to each bottom chord of the floor trusses.

STEEL DENSITY

The steel density was initially assumed to be 490 lb/ft^3 for the steel elements of the truss. However, the total weight of the steel produced by the models was much lower than the weight of steel reported in the construction drawings or by that reported by the fabricator. This is because the computer model calculates weight based on the volume of elements used in the stiffness formulation and neglects the extra weight of gusset plates, stiffeners, and welds, particularly since the main truss members were given net section properties. In addition, the weight estimate on the first page of the shop drawings was 505.3 kips heavier than that shown on the construction plans. To verify the weight of the truss, the shop drawing bill of materials (BOM) was independently calculated page by page using a modern spreadsheet. At the time of fabrication, cost was based on weight of steel, not labor. Therefore the shop drawing BOM kept track of both bid items and built items since sometimes the fabricator would substitute larger cross-sections than specified. It became easy for the spreadsheet to keep track of the bid weight (to verify the weight in the construction plans) and the built weight. The comparison of the steel weight is shown in Table 1. Considering just the main truss, the bid weight was 111.0 kips lighter than that reported in the construction plans and the built weight was only 53.8 kips lighter. The built weight of 6322.9 kips calculated in the spreadsheet was considered to be the best estimate of true bridge weight. The steel density in the model was adjusted so the total weight of the model matched this best estimate.

The weight of the walkways was not tallied as part of the steel weight because they were exclusively integrated into the model as described in the previous section, however, the ladders were included in weight estimate.

Table 2 outlines the weight of all structural steel reported in the construction plans, shop drawings and from the FHWA models. The steel density was modified for the North Approach, South Approach, and Truss models to match the weights reported in either the construction plans or spreadsheet to represent the true weight from all the miscellaneous steel plate attachments. For comparison, the modified steel density entered into the FHWA models is reported in Table 3. The density is higher than 490 lbs/ft^3 because Abaqus calculates weight based on member volume only. The modified density accounts for all the miscellaneous attachments such as gusset plates and stiffeners that are present in the actual bridge.

The original steel weight estimate was derived early into the investigation, however, as will be described in later chapters, stability divergence of the models occurred at load levels slightly higher than those known to be on the bridge at the time of collapse. There were known oversights in the original estimate but were concluded at the time to be of little significance. Specifically, materials listed in the BOM encompass all that is needed to construct the bridge. Therefore, the original weight estimate from the BOM could be higher than the real weight because some steel is scrapped from stiffener snipes or in the case of I35W, all the access holes cut into the built-up box members. At the same time, the BOM does not include the weight of weld material, rivet heads, or paint. In the first estimation, overestimating the weight by including the access holes was thought to offset ignoring the rivet heads, weld and paint within a tolerance for this investigation. Late into the investigation, another spread sheet was employed to track the weight of all the access holes and rivet heads in the main trusses in order to derive a tolerance as to which the steel weight was known. The refined calculations found that the original steel weight estimate was 89 kips heavy because the access holes were not subtracted, but light by 48.7 kips because rivet heads in the main trusses were not counted. Paint was also neglected in the steel weight estimate. Typically, the weight of paint is ~1% of the steel weight and for the I-35W bridge this was estimated to be 60 kips. The smaller rivet heads used for attaching the floor trusses and upper/lower lateral braces to the main truss were not tallied. In final, the original steel weight estimate was probably light by approximately 40 kips. The steel densities were not updated within the models to account for the extra 40 kips of steel weight because it was time-prohibitive to rerun all the models

CONCRETE DENSITY

For the evaluation of design conditions

Initially, the concrete density for all elements with concrete material properties was assumed to have a weight density of 150 lb/ft^3 in the FHWA models. This includes the density specified for the deck, barriers, and the additional deck thickness added to the bridge. Table 4 compares the weight of concrete shown in the construction plans to that produced by the global Designed (1965) model after Analysis Step 2. For helpful comparison to other models, Table 5 outlines a detailed breakdown of the concrete weight of the deck, original barriers, increased weight of new deck thickness, and increased weight of modified barriers.

For the evaluation of the collapse investigation

In the evaluation of the concrete deck cylinder properties the density of the original deck concrete (minus any rebar) was 150 lb/ft^3 and that the overlay was 140 lb/ft^3.[5] The deck was heavily reinforced with transverse rebar which would add to the aggregate concrete density that should be entered into the model since the model represents the original 6.5 inch thick deck as a shell element and the added thickness over time as a pressure applied to the shell element. Shown in the Appendix are two MathCad sheets that calculate the bulk density of the original concrete deck with steel reinforcement using an absolute volume approach. These calculations were performed for two different sections of the deck and on average were found to be 160.56 lb/ft^3. Considering that the original deck thickness is not precisely known, the original 6.5 inch deck was assumed to be 160 lb/ft^3 . The additional deck thickness added over time was assumed to be 140 lb/ft^3 based on the measurements of the deck cylinders.[5] The barriers were assumed to be 150 lb/ft^3.

UNCERTAINTY OF DEAD LOADS

Knowingly there was some dead weight that was ambiguous or difficult to account for in the bridge. The following are sources of potential error in the dead load estimate:

- The steel weight was light by approximately 40 kips because the steel weight audit did not account for paint, rivet heads in the floor trusses, rivet heads in the sway frames, rivet heads in the lateral bracing, bolt heads, nuts and washers in the stringer connections, and weld.

- The steel expansion joints were not exclusively counted, but probably weighed on the order of 100-200 lbs/ft. However, the shell elements used to represent the 6.5 inch deck were carried into the region of the expansion joints and the difference in weight was assumed to be negligible

- There were miscellaneous attachments to the bottom of the deck. Particularly, there were electrical boxes and conduit for the navigation light systems as well as the de-icing system. These two systems are very difficult to account for, but are estimated to be approximately 15 kips.

- Variations in concrete dimensions of the deck and barriers. The weight calculations used average measurements and/or designed dimensions. It would take very little dimension change to significantly change the weight because of the large deck area. Therefore, the concrete weight can be estimated to vary by plus/minus 200 kips.

In conclusion, given the sources of possible error in the calculations, the total dead load may be up to 300 kips light.

TRUSS SPAN MODELS

A view of the global stick model is shown in Figure 6. The truss was modeled using the geometries and members sizes outlined in the design plans.[1] All main truss, floor truss, stringer, and cross-girders were modeled with beam elements (mostly Abaqus B33 and some B31 elements) using the Abaqus *BEAM GENERAL SECTION command to define the cross-sectional properties. The deck was modeled with linear shell elements (Abaqus S4R). All the joints between members were considered perfectly rigid unless noted otherwise.

The geometry of the model tried to represent the as-built bridge as closely as possible without adding excessive complication. The model included the super-elevation and horizontal curve present at the south end of the truss, along with the deck flare at the north end of the bridge. In some cases, the geometry was not perfectly captured in the model and those differences will be discussed in the following section.

All main truss and floor truss members were modeled with 5 elements along their length to ensure any P-δ effects that might occur could be captured. The stringers were modeled with 10 elements between the floor trusses because they were modeled with lower order linear elements (B31).

Main Truss

The main truss members were welded, built-up box or I-shapes. The members were rigidly connected together at each truss node to simulate the moment restraint of the truss gusset plate connections. Rigid offsets were not used to represent the main truss members within the gusset plate because this would produce an overly stiff model.

All of the built-up box members in the main truss have regularly spaced access holes that will have an effect on member stiffness. This effect was determined by constructing a detailed finite element model of a typical box member (U10-L9) with solid elements. The analysis compared the deformation of the U10-L9 member modeled with and without access holes under unit loads. Table 6 shows the net section to gross section stiffness ratios for axial force, bending and torsion determined from the finite element model of member U10-L9. For comparison, the second column shows the average net section to gross section stiffness ratios calculated for 29 main truss members. There is a close match between the FEA results and the calculated properties, indicating that net section properties dominate member deformation. Therefore, all box members with access holes were modeled with net section axial and bending stiffness and 47% of the torsional moment of inertia of the closed section.

Floor Trusses and Sway Braces

Figures 7-9 show cross-sectional views of a typical floor-truss system and how it was idealized within the model. For the most part, the centroid of the model elements coincides with that of the members. There are some cases, however, where the model slightly differs from the member geometry. To simplify the modeling, member offsets were not used for many of the secondary members. For instance, the bottom horizontal of the sway brace was not modeled as it was built because the nodal location was determined by the bottom chord of the main truss. It was considered more important to the have the main truss chord location correct and sacrifice the correct centroidal location of the lower horizontal of the sway brace. Figure 7 shows the location of member centroids and nodes used in the global models for typical bridge cross sections

Figure 8 shows the location of member centroids and nodes used in the detailed model for the bridge cross section at FT10. The only difference from the global model is that rigid offsets were added to correct the centroid location of the two floor-truss diagonals framing into the main truss vertical members. The rigid offsets were added to correctly capture any moment transfer into the U10 joint, since this became the focus of the collapse investigation. The rigid offset was modeled using the Abaqus *MPC RIGID element.

Figure 9 shows a typical view of the model idealization at the center of the floor truss. The upper lateral bracing framed into the floor truss at its proper location. To do this, fictitious elements had to be incorporated in order to create a node at the correct location. In Figure 9 these elements are labeled as “Stringer Rigid Links”. These elements were given cross-sectional area of 50 in^2 and moments of inertia of 50 in^4. Stringer Rigid Links were also used to properly offset the centroidal location of the stringers from the top chord of the floor truss. Additional fictitious elements termed “Composite Deck Connector” and “Axial Deck Connector” were used to properly model the centroidal distance of the concrete deck relative to the stringers. Both of these elements were assigned areas of 50 in^2, but the composite deck connectors were given moments of inertia of 30 in^4 and the axial connectors assigned a moment of inertia of 3 in^4. The deck was only compositely connected to the stringers within 30 ft. of the deck expansion joints using shear studs. Stiffer Composite Deck Connectors were used to attach the deck to the stringers in these regions to reflect the presence of shear studs. Elsewhere, the deck was floating and connected to the stingers with the softer Axial Deck Connectors. All these fictitious elements were used in place of centroidal and rigid offsets because they introduce some flexibility into the system that can be calibrated to make the model match live load strain gauge data.

Also shown in Figure 9 are the moment releases used in the model. The end of the Stringer Rigid Links that framed into the stringers had all three moments released to prevent moment transfer from the stringers into the floor truss. In addition, weak axis moments on each end of the diaphragms (members between the stringers) were released because the connection plate details are not able to transfer significant moment.

Figure 10 shows how the details of the floor truss bracing system were represented in the model. These diagonal members provided a connection between the lower floor truss chord and the stringer at two locations. The diagonal members were connected with pinned joints, therefore moment releases were added to the model as shown.

Stringers

All stringers were modeled with Abaqus B31 beam elements. These elements are formulated using a linear shape function compared to the conventional cubic shape function used for most beam elements. This was intentionally done to provide compatible displacement fields between the deck and stinger elements. The S4R shell elements used for the deck are also formulated with linear shape functions.

At certain locations, the stringers were discontinuous and allowed to axially move relative to each other. Shown in Figure 11 is typical detailing of a stringer expansion joint as it passes over the floor truss top chord. In this example, the left stinger is fixed to the floor truss chord because they are bolted together. The stringer on the right side of the floor truss sits upon the floor truss, but is allowed to slide in the longitudinal direction by means of a slotted bearing. This expansion joint is present in every stinger at floor truss lines 4, 8, 14, 8' and 4' , corresponding to the locations of the deck expansion joints. The stringer expansion joints are also present at every floor truss on the stringer S3 and S12 lines which are directly over the main trusses. The stringer expansion joint could not be modeled with axial releases since Abaqus does not support axial and shear releases for beam elements. However, Abaqus does provide a library of kinematic constraints, referred to as connector elements that could be used to model the axial release. In particular, the TRANSLATOR element allows for axial motion between two nodes while coupling all remaining degrees of freedom. Since no moment can transfer between the left and right stringers in Figure 11, a moment release was provided on the stringer element fixed to the floor truss. In Step 3 of the analysis, 300 kip/inch axial springs were placed in parallel to the connector elements to simulate friction effects. This will be fully explained in the "Calibration" section.

Floor Beams

There were two deep floor beams at the north and south ends of the bridge to transfer stringer reactions out to the two main trusses. Later into the investigation when the model was being used to actually model the collapse condition, Abaqus ran into convergence issues with some of the floor beam elements. The convergence issue arose because as the bridge deflected, the support bearings would move as the bridge elongated. This motion caused the stringers to put out-of-plane force on the floor beams that was causing lateral-torsional buckling. Since this failure mode was fictitious (because it was occurring in the model at loads less than present on the bridge at the time of collapse), moment releases were added to alleviate this issue. Shown in Figure 12 is a partial view of the north floor beam from the model. The first fix was to release all three moments from the stringer elements at the end they frame into the floor beam links. The second fix was to provide one moment release on the top end of the link between the main truss and the floor beam. This single moment release allowed for the floor beam to rotate about its longitudinal axis on the link element.

Piers

The piers were included in the model because the live load calibration showed, at least under live loads, that the bearings were probably locked. This forced the piers to move in place of the bearings. The piers were modeled with a mix of beam and shell elements because the two interior piers had large cast infill walls that were better modeled with shell elements. All three moments were released on the pier element ends intersecting the main truss. In the first three steps of the analysis, the bridge was assumed to be supported on ideal pin and roller boundary conditions as designed. However, as the live load calibration showed, the bearings were locked and engaged the piers for the final step of the analysis.

For the first three steps of the analysis, the eight nodes representing the support points of the main trusses were assigned the appropriate pin and roller boundary conditions. However, as the bridge expands under applied load, the piers must translate so they are in their proper location when they are fully engaged. With a moment release at the top of the pier, and using ideal boundary conditions at the base of the truss, the pier could undergo rigid-body rotation as the bridge expands through the first three steps of the analysis. In order to prevent rigid-body rotation, a rotation constraint was added at the foundation level of the piers to prevent them from rotating in the north/south direction. At the beginning of Step 4, the boundary conditions were changed such that all degrees of freedom were restrained at the foundation of the piers and the ideal boundary conditions were removed from the main truss support nodes. This is illustrated in Figure 13.

The piers were assigned a modulus value of 5400 ksi based entirely on measurements from cores removed from the wreckage site.[5] This material was also given “massless” density such that the weight of the piers would not factor into any of the reaction output summaries.

Approach Spans

Each of the approach spans was modeled separately using 3D frame elements for the girders and shell elements for the deck. The deck was assumed to be composite with the beams. However, since line elements were used for the girders and shells for the deck, the same link elements used in the truss spans were used in the approach span models. In the truss span, there were composite and non-composite link elements. Since there was no live load data to calibrate the “compositeness” of the approach spans, the link stiffness in the model was assumed to be the same as the Composite Deck Connectors used in the main truss model.

When the approach span models were run, the output of interest was the two vertical reactions at the end of the cross-girder where they set upon the main truss cantilevers. Tables 7 through 9 outline the reaction forces imparted onto the main truss by the two approach spans through loading steps 1-4 for the Designed (1965), As-Built (2007) , and Detailed models.

The approach span models also provided the equivalent spring stiffness that needs to be applied to the ends of the main trusses. As the truss deflects under load, the cantilever ends will undergo slight upward vertical deflection. This causes an increase in reaction force on the truss because the approach span girders want to resist this uplift. On the other hand, downward vertical deflection of the cantilever truss ends tends to lighten the approach span reactions. To determine equivalent spring stiffness for the approach spans, unit displacements were applied at the end reactions in the approach span models. The additional reaction force then represents the spring stiffness. Table 10 outlines the equivalent spring stiffness that was added at the four main truss cantilevers. Cross-coupling of the spring stiffness between the East and West sides was minimal, on the order of 0.1-0.3 kip/inch, and was therefore neglected.

CALIBRATION

Live load data collected by the University of Minnesota (UofM) in 1999 was used to calibrate the model to further ensure its correctness[6]. The UofM ran four loading configurations with nine sand trucks, each weighing 51 kips. Only the "Test 4" configuration was used to calibrate the FHWA model because it provided the best data quality. The UofM applied two strain gauges to each of the U10-U9, U10-L9, and L10-L9 main truss members. In the Test 4 loading scenario, three trucks ran side-by-side in the three leftmost lanes and made three consecutive passings across the bridge going southbound and northbound at normal traffic speed (between 45-55 mph). The raw data was post-processed at TFHRC and each of the southbound passings were averaged together to reduce noise-levels in the data. The same truck load configuration was applied to the model. Figures 14-19 show the influence lines for member axial force that were derived from the strain gauge data. For comparison, influence lines from the model are shown based on three different boundary condition assumptions.

The calibration provided insight that went into the development of the model. Good correlation occurred when the link elements between the floor truss and the stringers were extremely stiff. However, when these elements have extremely high stiffness the deck provided an artificial compositeness and the upper chord forces were extremely low. Since the bridge was detailed to decouple the floor system from the main truss, having this deck absorb some the axial force from the main truss chords did not seem appropriate. To make the chord forces match the construction plans and the independent BSDI model, these link elements had to have their stiffness reduced. However, the peak forces no longer matched, particularly for the west truss lower chord influence line (Figure 18). To further synchronize the model output with the live load data, it was found that using elastic springs across the stringer expansion joints helped to match the live load data with the model output. The best results were attained with a spring stiffness of 300 kip/inch. In the collapse modeling, these springs were only activated in step 4 of the analysis and should be thought to represent the stiffness due to friction within the stringer expansion joints.

The final conclusion found through the calibration showed that the live load data fell in-between the assumption of ideal and completely fixed boundary conditions. As the graphs show, once the pier stiffness is taken into account, the model output agrees very well with the live load data. This conclusion only assumes the bearings behave frozen (and hence force the piers to displace) under live loads only, hence why the piers were engaged only in step 4. This conclusion is not meant to derive the bearings do not move under thermal loadings.

MEMBER FORCES AND REACTIONS

Tables 11-14 show the internal axial force for the main truss members after step 2 of the analysis (original steel, deck and barrier weight). This data was tabulated for both the Designed (1965) and As-Built (2007) FHWA models. For comparison, results from the BSDI model (Designed 1965) and the URS model (Designed 2003)[8] are shown in the tables. Shaded cells in these tables represent members where the force was more than 10% different from the member forces shown in the original design plans.[1]

Tables 15-18 make direct comparisons of the axial member forces due to dead load reported on sheet 20 of the original design plans[1] to the forces produced from the FHWA Designed (1965) model after Step 2. Many of the members compare quite reasonably with differences less than 5%. However, many of the outlier members are verticals which are supposed to be zero-force members and it is not clear how exactly the designer arrived at those forces. Other outlier members were located in the back-spans away from the U10 location critical to this investigation.

Table 19 compares the vertical reaction forces produced by the three FHWA models after Step 2 to the reactions reported on sheet 20 of the design plans. The values are close, but indicate the model is lighter in the back-spans than the designer assumed, perhaps explaining why the member forces differ more in this area too.

Tables 20-22 report the vertical reactions from the three models for steps 1-4 of the analysis, which would be representative of how the loads changed through time. These tables clearly show that the reactions due to dead load increased by an average of 24% over time because of the modified barriers and increased deck thickness.

Since the U10 node became critical to the investigation, Table 23 outlines the axial forces in the five members framing into the U10 node. Also shown in this table are the design forces from sheet 20 of the design plans.[1] These member forces were plotted in Figure 20 to show how they changed over time as the analysis progressed. The graph shows that the force in the tension diagonal (U10L11) comes very close to the original design force when the construction load is on the bridge. The U10L9 compression diagonal actually exceeds the original design force with the construction load in place. Actual member capacities were not calculated.

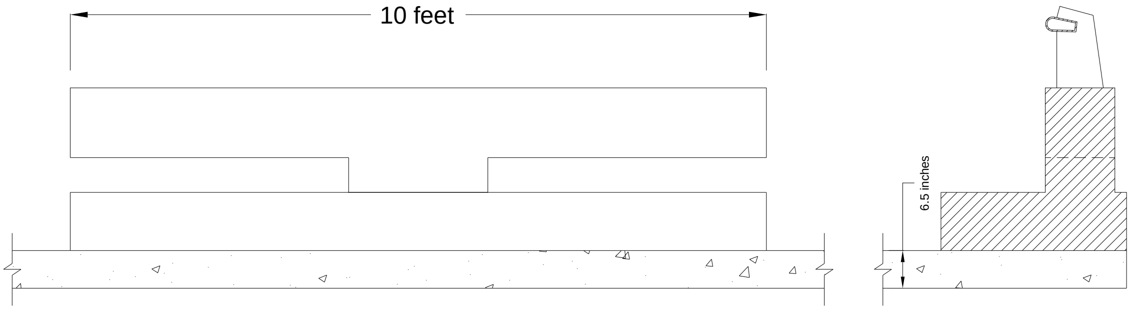

On average over a 10 foot length
4983.33 lb in concrete
111.2 lb for rail
70 lb for base

Total Weight (516 lb/ft)

Figure 1. Originally designed exterior parapet in 1965.

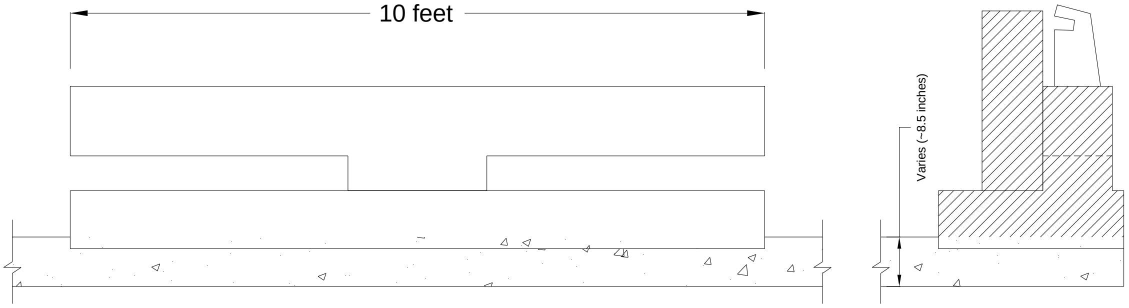

On average over a 10 foot length
7707.3 lb in concrete
70 lb for base

Total Weight (778 lb/ft)

Figure 2. Existing parapet at time of collapse in 2007.

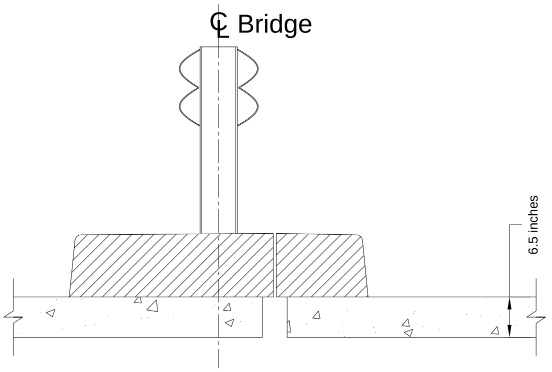

On average over a 10 foot length
Concrete (490.08 lb/ft)
Two steel guardrails (16.65 lb/ft)
Steel post (37 lbs)

Total Weight - 507 lb/ft

Figure 3. Original median barrier in 1965.

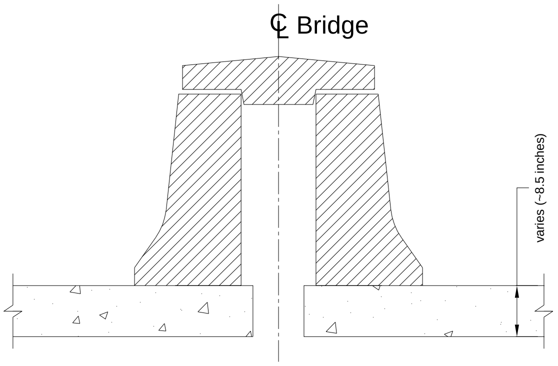

Type F Median Barrier (432.69 lb/ft ea.)
Precast Topper (189.58 lb/ft)

Total Weight - 1055 lb/ft

Figure 4. Existing median barrier at time of collapse in 2007.

U0' U4' U8' U14 U8 U4 U0

9.44 inches	8.13 inches	8.79 inches	8.93 inches	8.75 inches	9.21 inches
8.56 inches	8.25 inches	8.72 inches	8.63 inches	8.63 inches	8.67 inches
6.75 inches	6.88 inches	6.83 inches	6.69 inches	6.94 inches	7.70 inches
8.63 inches	8.56 inches	8.72 inches	8.92 inches	9.25 inches	9.38 inches

Figure 5. Deck thicknesses at the time of collapse in 2007 based on concrete core thickness measurements.

Table 1 Steel Weights Estimates

	Steel Weight Estimates (kips)			
	Design Plans[1] (sheet 63)	Shop Drawing Estimates [a]	Spreadsheet Bid Weight [a]	Spreadsheet Built Weight [a]
South Approach	1174.0	1206.3	n/a	n/a
Truss Span	6376.7	6882.0	6265.7	6322.9
North Approach	1257.1	1274.0	n/a	n/a

n/a – Approach span fabrication appears to have been subcontracted by the prime fabricator (Allied Structural Steel) and those drawings did not include a bill of materials. It was deemed to require too much effort to calculate these weights with the spreadsheet.

[a] – Weights do not include the weight of the bearings, expansion joints, and walkways.

Table 2 Total Steel Weight from FHWA Models with Modified Steel Density

	Total Steel Weight (kips)				
	Bridge Weight (Best Estimate)		FHWA Models		
	Bid Weight	Built Weight	Designed (1965)	As-Built (2007)	Detailed As-Built (2007)
South Approach	1174.0	1206.3	1174.0	1206.3	1206.3
Truss Span	6265.7	6322.9	6266.6	6323.6	6321.3 [a]
North Approach	1257.1	1274.0	1257.0	1274.1	1274.1

[a] - this model used the modified steel density for all beam elements, however all the shell elements in the U10 and L11 joint models used regular steel density, hence the slightly lower weight over the As-Built model

Table 3 Modified Steel Density from FHWA Models

Model	Modified Steel Density (lb/ft^3)		
	Designed (1965)	As-Built (2007)	Detailed As-Built (2007)
North Approach	546.0	553.4	553.4
South Approach	551.4	566.6	566.6
Main Truss	551.9	555.7	555.7

Table 4 Design Deck and Barrier Weight Comparisons

	Concrete Weight Estimates (kips)	
	Design Plans[1] (sheet 63) [a]	Designed (1965) Model [b]
South Approach	4633.2 (1144 yd^3)	4422.0
Truss Span	11429.1 (2822 yd^3)	11324.8
North Approach	3612.6 (892 yd^3)	3586.0

[a] - Concrete weight in construction plans is for the concrete only, not including the steel rail systems from the interior median.
[b] - Concrete weight from the Abaqus model includes the weight of all steel railings.

Table 5 Total Concrete Weight from the FHWA Models

	Concrete Weight Estimates (kips)		
	Designed (1965) Model	As-Built (2007) Models	Detailed As-Built (2007) Model
Weight of Original 6.5 inch Concrete Deck	9696.8 (sum = 9696.8)	9696.8 (sum = 9696.8)	10342.7 [a] (sum = 10342.7)
Weight of Original Barriers	1628.0 (sum = 11324.0)	1628.0 (sum = 11324.0)	1628.0 (sum = 11970.7)
Additional Weight due to Added Deck Thickness	3312.7 (sum = 14637.5)	3312.7 (sum = 14637.5)	3139.0 [b] (sum = 15109.7)
Additional Weight due to Modified Barriers	1132.9 (sum = 15770.4)	1132.9 (sum = 15770.4)	1132.6 (sum = 16242.3)

[a] – increased weight in detailed model is due to heavier 160 lb/ft^3 concrete density accounting for heavy reinforcement ratios

[b] – decreased weight in detailed model is due to using a lighter 140 lb/ft^3 density for the overlay based on physical measurements of cores.

Table 6 Net/Gross Section Properties of Main Truss Box Members

Deformation	Net/Gross Section Stiffness Ratio from FEA [a]	Net/Gross Cross-Section Property Ratio [b]
Axial	0.87	0.85
X-axis bending [c]	0.96	0.98
Y-axis Bending [d]	0.78	0.72
Torsion	0.47	Not Applicable

[a] – From a solid element model of the U10-L9 member.

[b] – Ratios represent the average from 29 main truss members.

[c] – X-axis bending has the perforations at the neutral axis of bending.

[d] – Y-axis bending has the perforations at the extreme bending fiber.

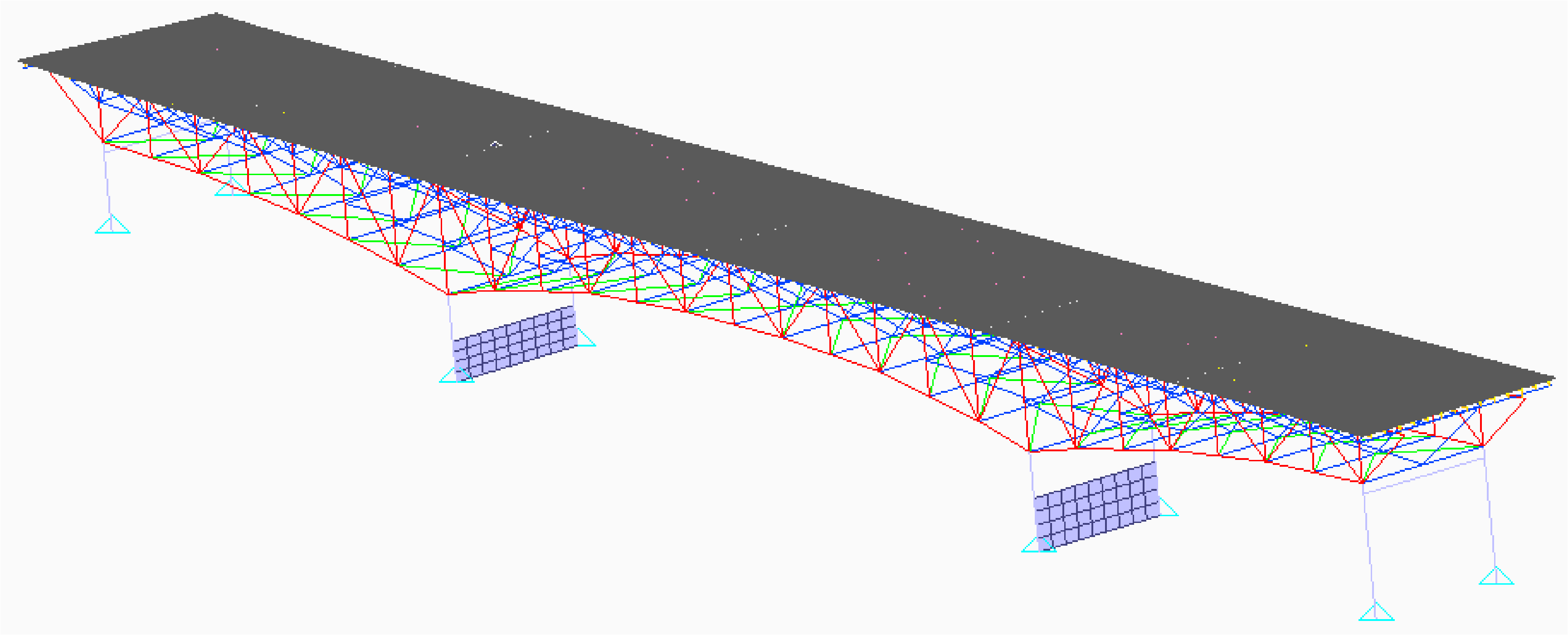

Figure 6. Overall view of global stick model.

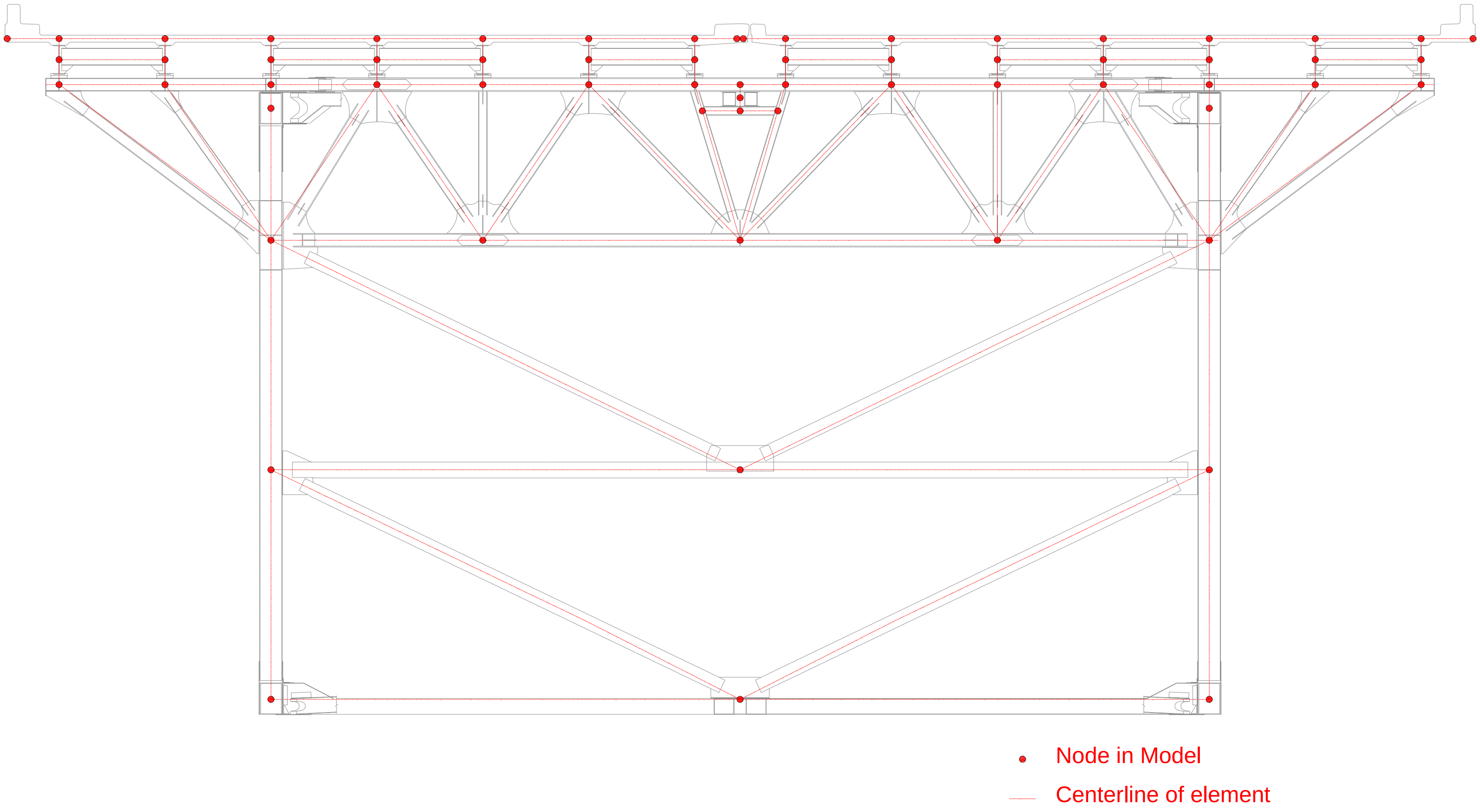

Figure 7. Idealization of floor truss system for Designed (1965) As-Built (2007) models.

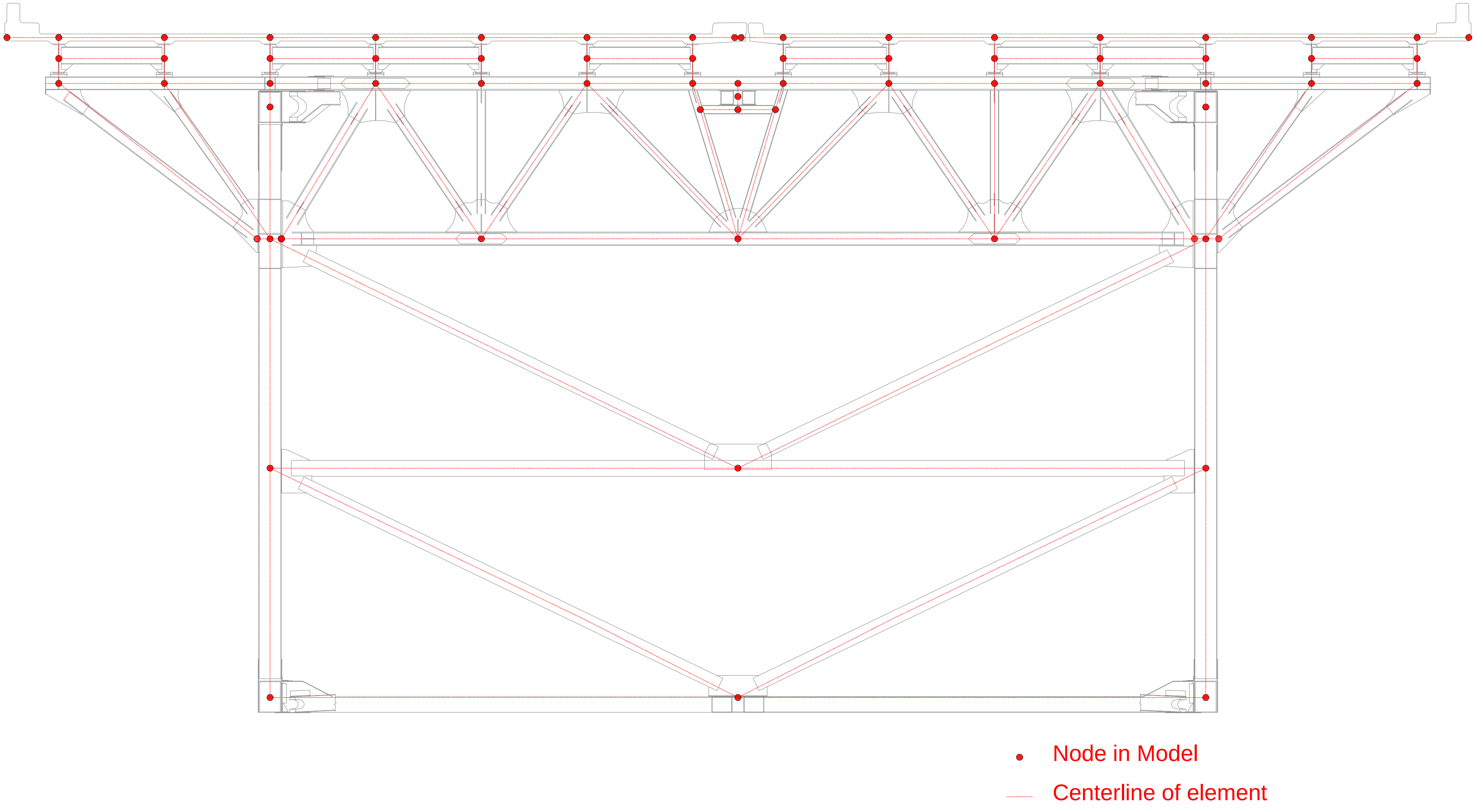

Figure 8. Idealization of floor truss 10 in Detailed Model.

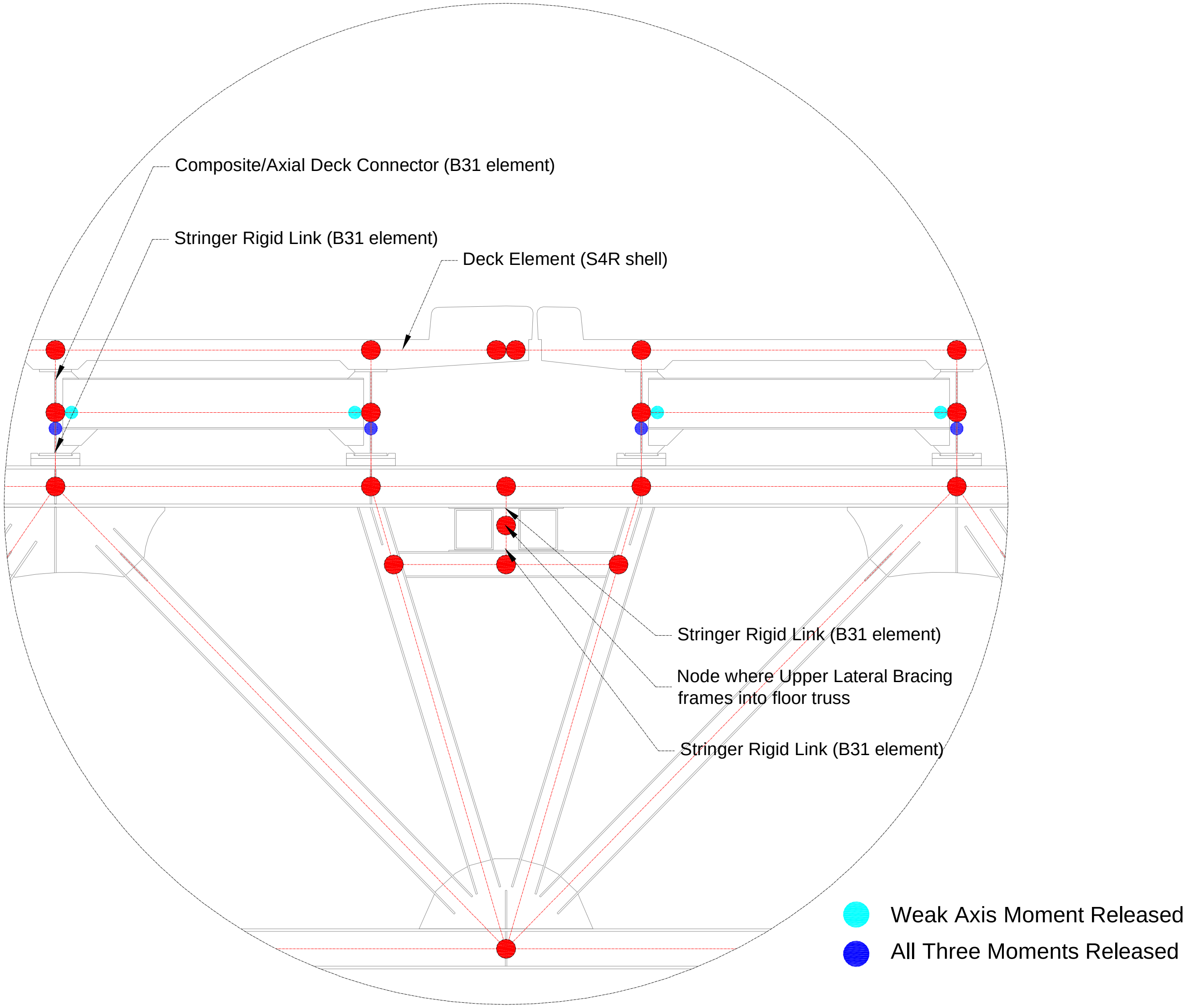

Figure 9. Zoomed view of floor truss idealization.

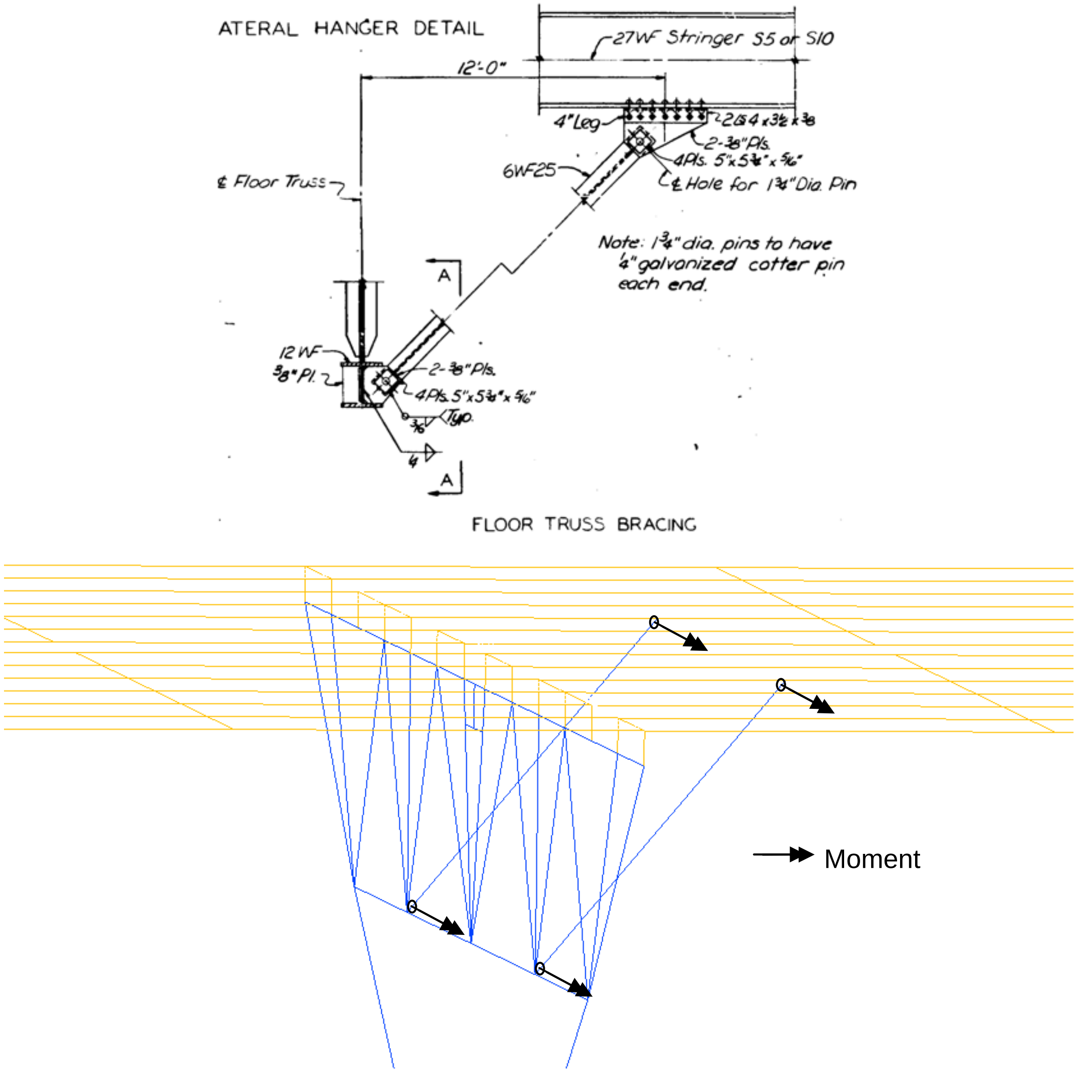

Figure 10. Detailing and idealization of floor truss braces. Top taken from design plans[1].

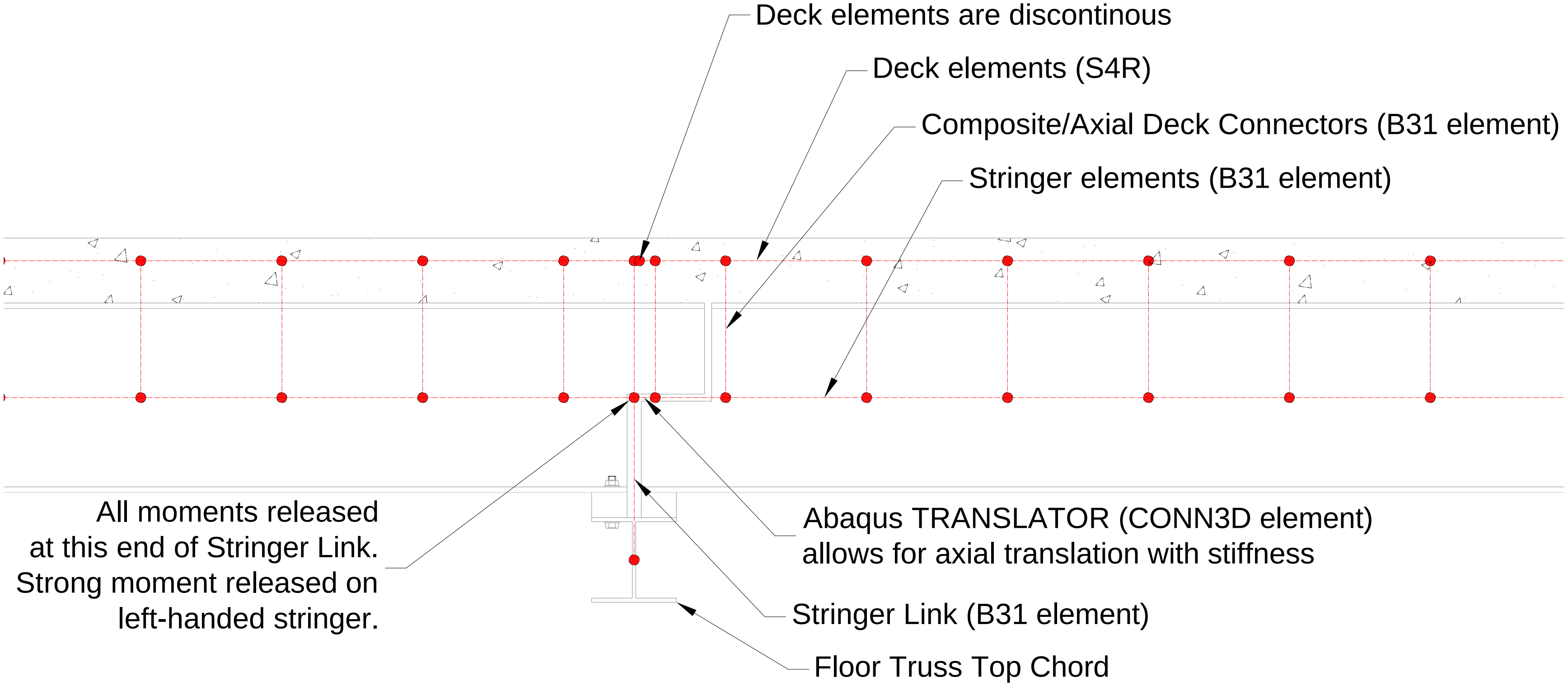

Figure 11. Idealization of deck and stringer structural system.

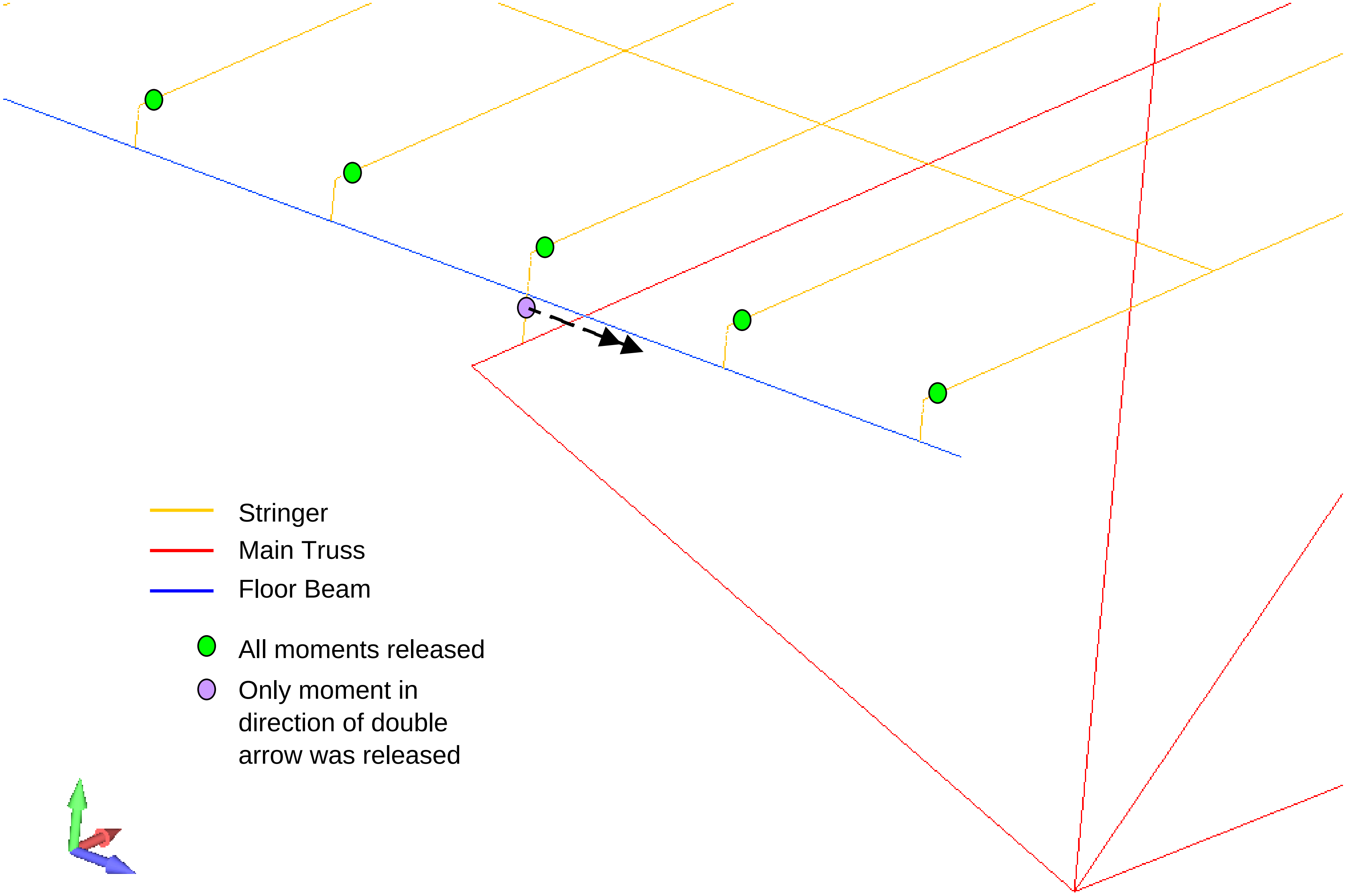

Figure 12. Illustration of moment releases near the floor beams.

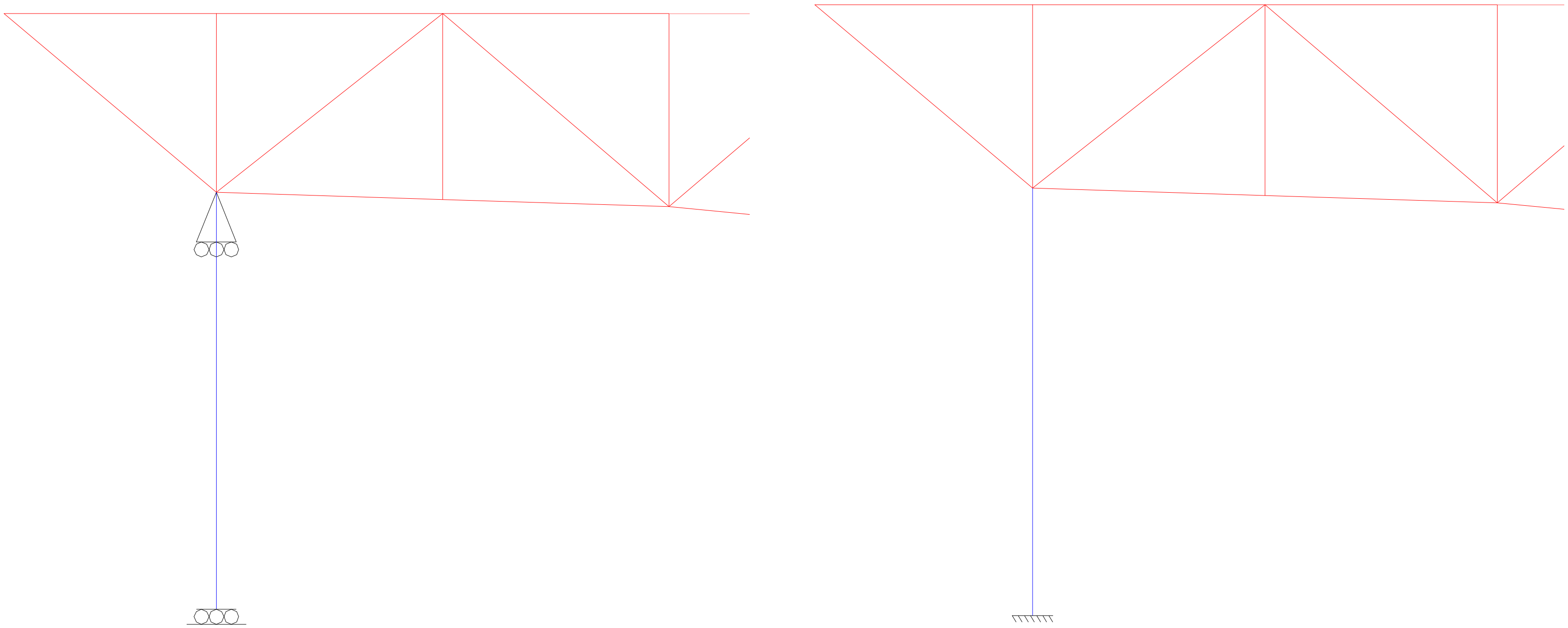

Figure 13. Bridge boundary conditions. Through first three steps (left). For final step (right).

Table 7 Designed (1965) Approach Span Reactions on the Main Truss

Analysis Step	Approach Span Reaction Loads on Truss Cantilever (kips)			
	NW Corner (node 74)	NE Corner (node 30)	SW Corner (node 859)	SE Corner (node 40434)
1	433.1	428.6	187.2	153.0
2	433.1	428.6	187.2	153.0
3	539.6	529.7	238.3	195.1
4	552.5	534.7	242.9	202.1

Table 8 As-Built (2007) Approach Span Reactions on the Main Truss

Analysis Step	Approach Span Reaction Loads on Truss Cantilever (kips)			
	NW Corner (node 74)	NE Corner (node 30)	SW Corner (node 859)	SE Corner (node 40434)
1	435.0	430.6	188.5	154.0
2	435.0	430.6	188.5	154.0
3	541.5	531.8	239.6	196.1
4	554.3	536.7	244.2	203.2

Table 9 Detailed Model Approach Span Reactions on the Main Truss

Analysis Step	Approach Span Reaction Loads on Truss Cantilever (kips)			
	NW Corner (node 74)	NE Corner (node 30)	SW Corner (node 859)	SE Corner (node 40434)
1	451.7	446.8	196.5	160.5
2	451.7	446.8	196.5	160.5
3	553.1	543.0	245.1	200.7
4	565.9	547.9	249.8	207.7

Table 10 Approach Span Spring Stiffness applied at the Main Truss Cantilevered Ends

Truss Corner	Spring Stiffness (kip/in)
NE	5.00
NW	2.95
SE	7.05
SW	9.45

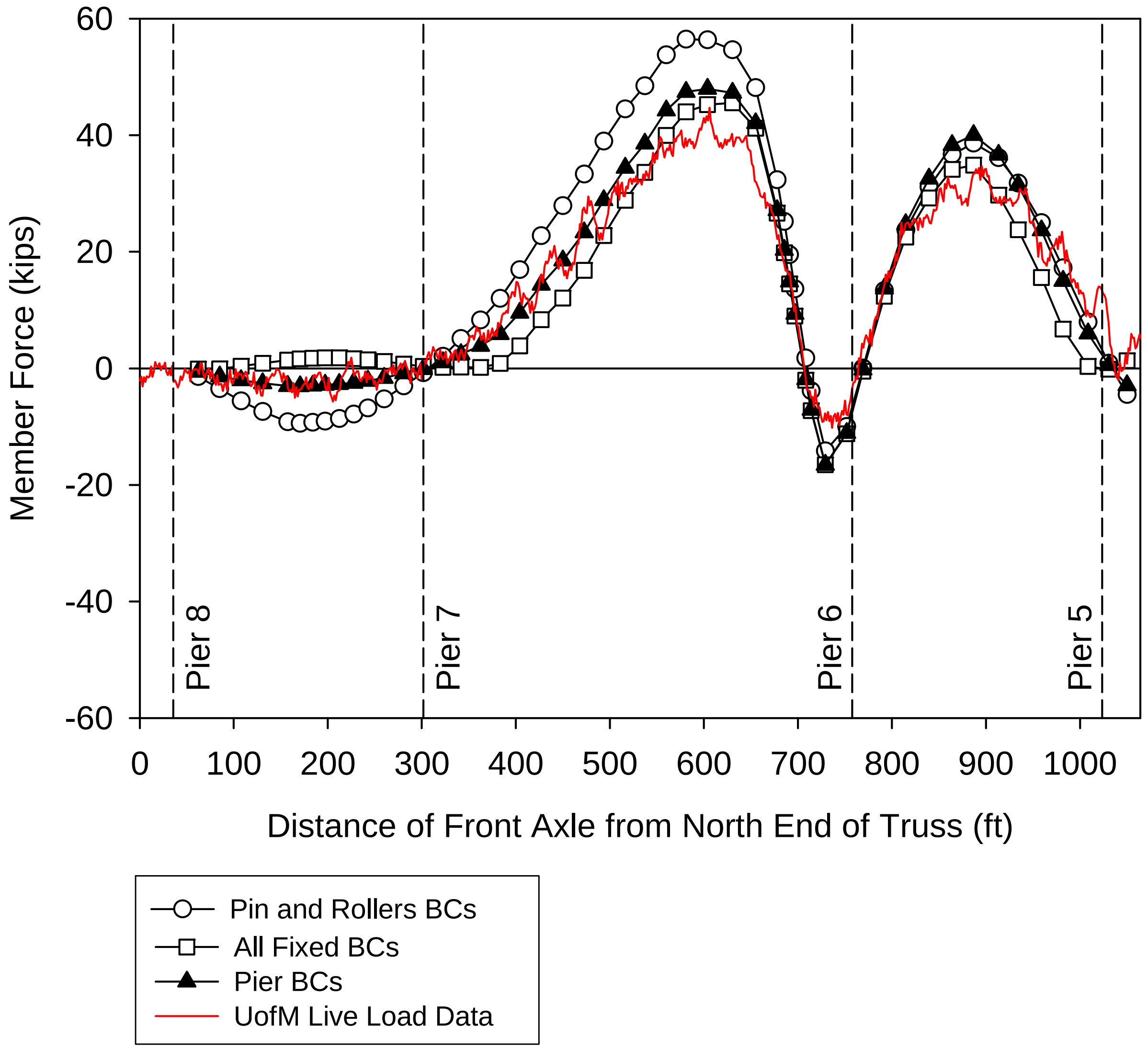

Figure 14. Influence lines from calibration for west truss upper chord member U10-U9.

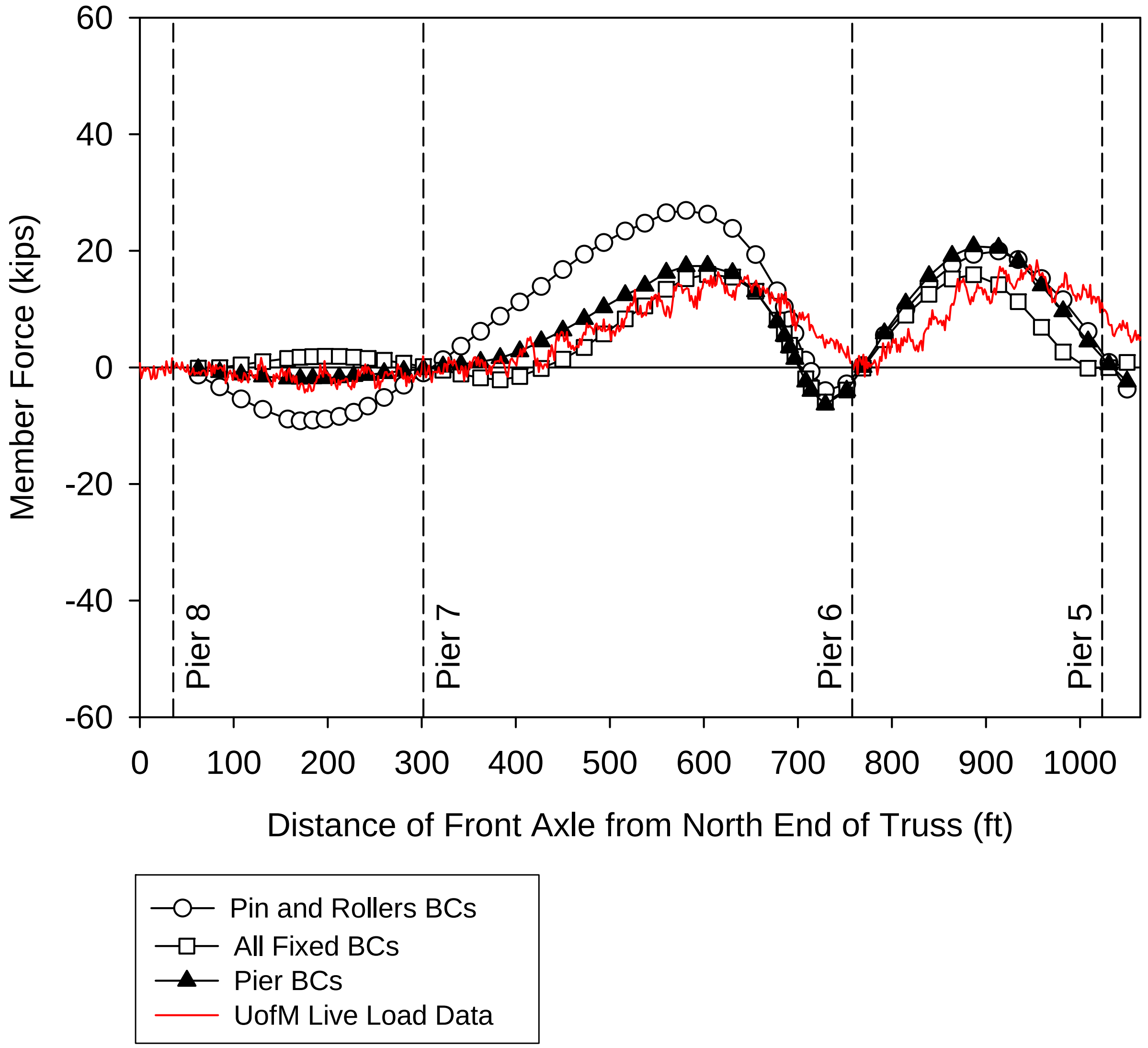

Figure 15. Influence lines from calibration for east truss upper chord member U10-U9.

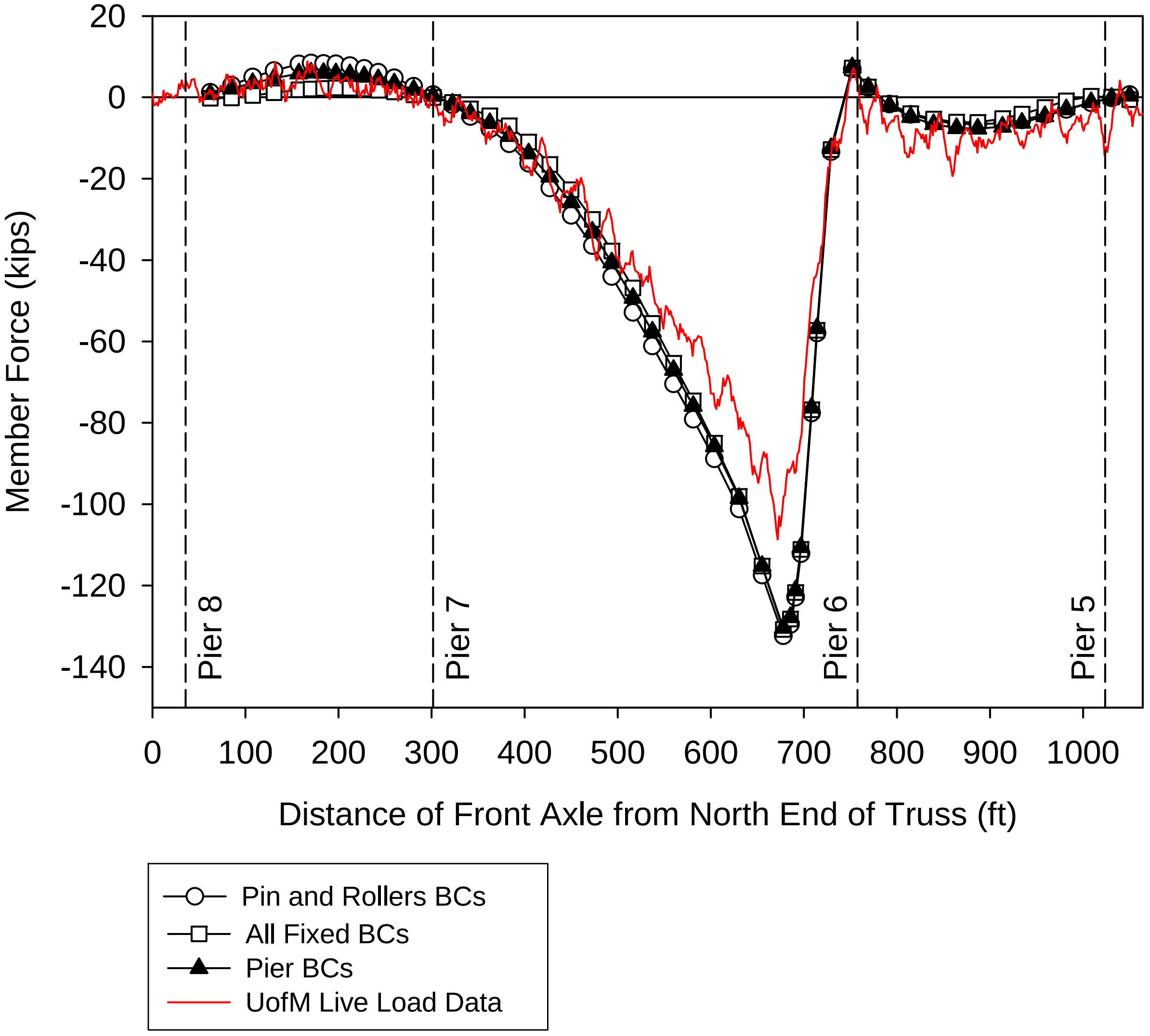

Figure 16. Influence lines from calibration for west truss diagonal member U10-L9.

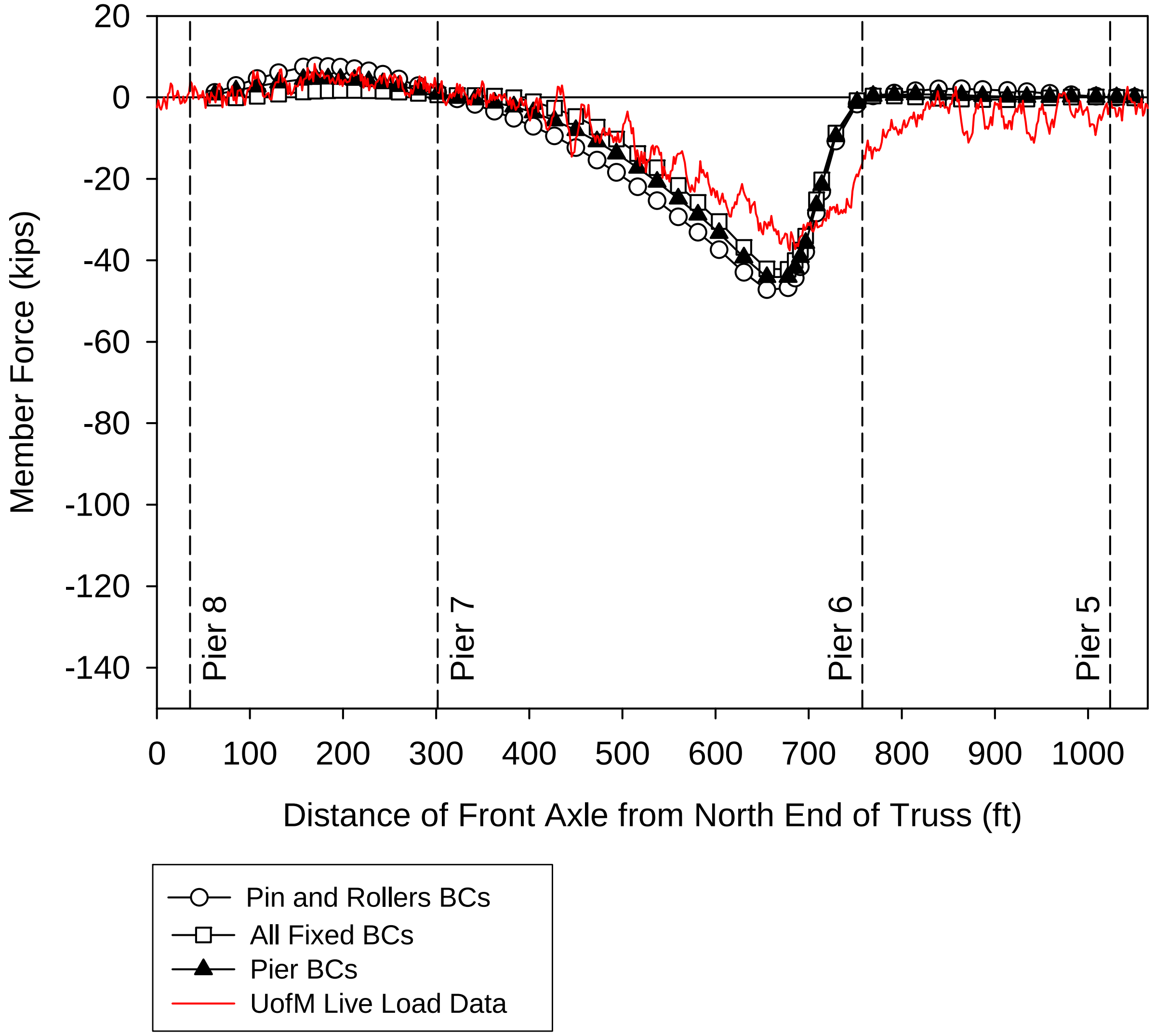

Figure 17. Influence lines from calibration for east truss diagonal member U10-L9.

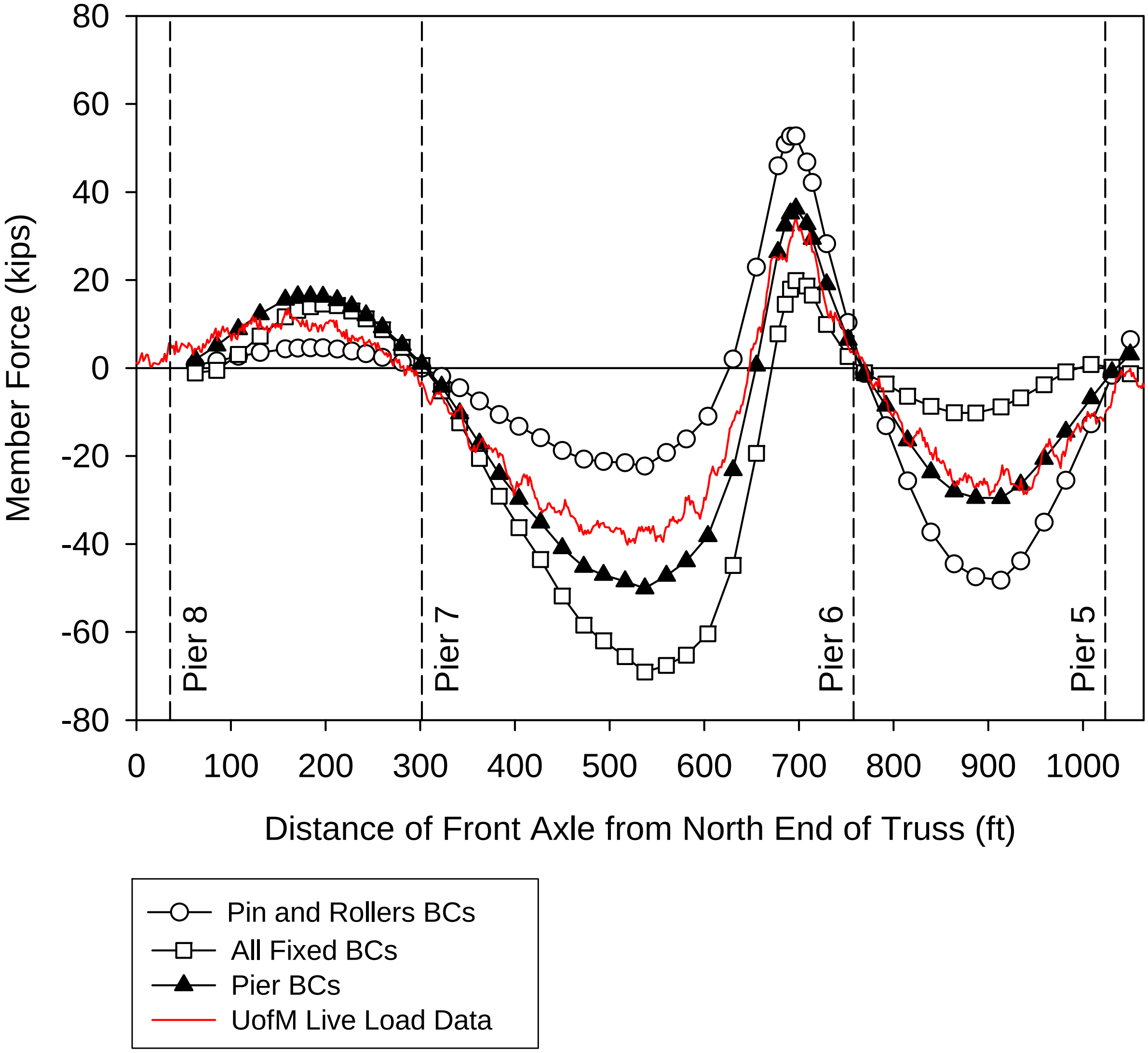

Figure 18. Influence lines from calibration for west truss lower chord member L10-L9.

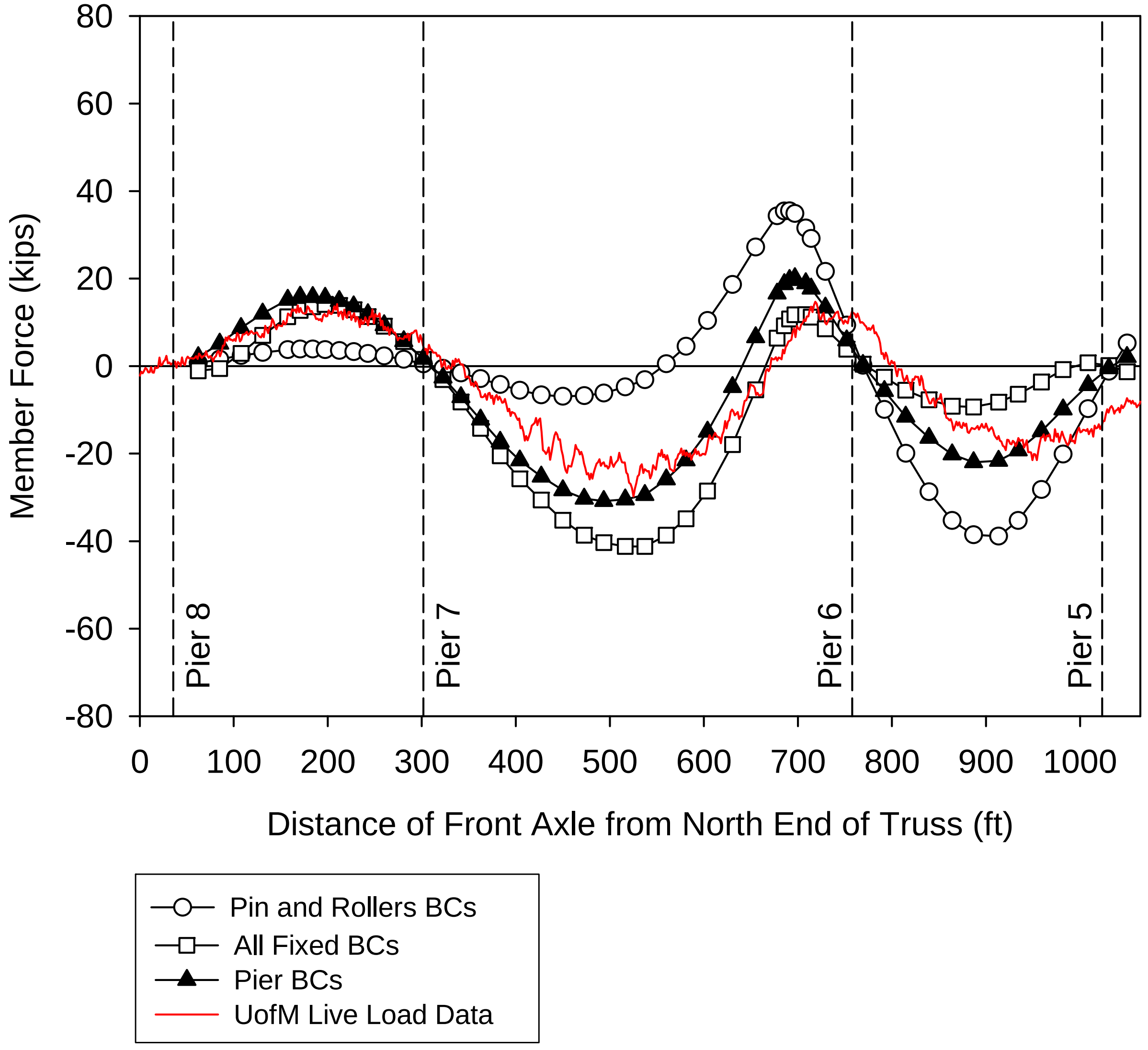

Figure 19. Influence lines from calibration for east truss lower chord member L10-L9.

Table 11 Main Truss Upper Chord Axial Forces After Step 2

Member	Member Axial Force (kips)							
	Design Plans	URS Designed (2003)	BSDI Designed (1965)		FHWA Designed (1965)		FHWA As-Built (2007)	
	Symmetric	Symmetric	West Truss	East Truss	West Truss	East Truss	West Truss	East Truss
U0-U1	439	483.5	391.0	431.0	319.7	315.9	319.8	319.8
U1-U2	439	421.3	391.0	425.0	313.3	313.4	312.7	312.7
U2-U3	-226	-224.0	-212.0	-203.0	-246.2	-244.0	-249.0	-249.0
U3-U4	-226	-219.4	-209.0	-197.0	-249.9	-246.2	-252.3	-252.3
U4-U5	516	495.6	487.0	489.0	420.2	423.0	421.7	421.7
U5-U6	516	466.4	485.0	487.0	396.1	384.5	392.3	392.3
U6-U7	1762	1935.0	1784.0	1793.0	1645.5	1673.5	1649.4	1649.4
U7-U8	1762	1991.2	1793.0	1801.0	1695.2	1694.7	1699.6	1699.6
U8-U9	1551	1730.0	1570.0	1579.0	1495.0	1493.5	1505.0	1505.0
U9-U10	1551	1726.5	1564.0	1576.0	1498.8	1496.5	1509.2	1509.2
U10-U11	-486	-527.6	-463.0	-466.0	-428.8	-428.4	-429.1	-429.1
U11-U12	-486	-390.7	-464.0	-465.0	-410.5	-410.9	-407.3	-407.3
U12-U13	-1899	-2002.7	-1896.0	-1905.0	-1785.5	-1784.6	-1790.6	-1790.6
U13-U14	-1899	-1972.1	-1806.0	-1814.0	-1723.9	-1723.3	-1728.7	-1728.7
U14-U13'	-1899	-2050.5	-1826.0	-1833.0	-1760.4	-1760.7	-1769.3	-1769.3
U13'-U12'	-1899	-2176.1	-1912.0	-1921.0	-1842.1	-1840.5	-1850.4	-1850.4
U12'-U11'	-486	-550.5	-518.0	-516.0	-475.5	-477.9	-474.4	-474.4
U11'-U10'	-486	-609.8	-498.0	-509.0	-481.1	-483.8	-482.4	-482.4
U10'-U9'	1551	1649.2	1508.0	1513.0	1440.6	1430.9	1450.5	1450.5
U9'-U8'	1551	1662.3	1519.0	1519.0	1444.0	1433.3	1454.0	1454.0
U8'-U7'	1762	1966.1	1757.0	1773.0	1673.5	1660.1	1678.2	1678.2
U7'-U6'	1762	1908.7	1742.0	1758.0	1588.7	1636.2	1593.3	1593.3
U6'-U5'	516	541.2	566.0	556.0	404.7	427.0	401.9	401.9
U5'-U4'	516	572.9	572.0	562.0	485.9	476.2	487.5	487.5
U4'-U3'	-31	10.2	10.0	8.0	-59.4	-65.0	-62.7	-62.7
U3'-U2'	-31	-16.5	0.1	-3.0	-62.8	-63.4	-67.5	-67.5
U2'-U1'	796	763.1	774.0	780.0	632.8	630.5	630.4	630.4
U1'-U0'	796	884.8	778.0	784.0	651.8	650.1	651.8	651.8

Table 12 Main Truss Lower Chord Axial Forces After Step 2

Member	Member Axial Force (kips)							
	Design Plans	URS Designed (2003)	BSDI Designed (1965)		FHWA Designed (1965)		FHWA As-Built (2007)	
	Symmetric	Symmetric	West Truss	East Truss	West Truss	East Truss	West Truss	East Truss
L1-L2	80	76.2	93.0	68.0	145.9	147.6	148.8	148.8
L2-L3	80	76.7	95.0	70.0	146.3	147.8	149.1	149.1
L3-L4	-18	-35.8	-22.0	-26.0	10.5	13.4	12.0	12.0
L4-L5	-18	-37.1	-26.0	-30.0	10.2	11.6	11.6	11.6
L5-L6	-1087	-1232.2	-1100.0	-1103.0	-1041.1	-1038.5	-1046.8	-1046.8
L6-L7	-1087	-1232.3	-1100.0	-1104.0	-1041.0	-1038.9	-1046.8	-1046.8
L7-L8	-2533	-2896.5	-2544.0	-2559.0	-2468.4	-2464.7	-2484.6	-2484.6
L8-L9	-2543	-2902.4	-2552.0	-2569.0	-2470.0	-2465.4	-2486.3	-2486.3
L9-L10	-559	-582.2	-529.0	-531.0	-504.0	-503.0	-507.4	-507.4
L10-L11	-559	-582.0	-527.0	-531.0	-504.0	-502.8	-507.5	-507.5
L11-L12	1311	1512.0	1325.0	1333.0	1283.1	1281.3	1290.9	1290.9
L12-L13	1311	1512.5	1330.0	1335.0	1283.7	1281.8	1291.4	1291.4
L13-L14	2036	2269.0	1995.0	2005.0	1926.0	1923.2	1938.1	1938.1
L14-L13'	2036	2269.0	1995.0	2005.0	1926.3	1923.5	1938.4	1938.4
L13'-L12'	1311	1556.7	1372.0	1375.0	1312.2	1311.2	1320.1	1320.1
L12'-L11'	1311	1556.4	1369.0	1374.0	1312.1	1310.3	1320.0	1320.0
L11'-L10'	-559	-527.6	-455.0	-465.0	-459.6	-456.8	-463.5	-463.5
L10'-L9'	-559	-527.8	-458.0	-465.0	-459.3	-457.1	-463.3	-463.3
L9'-L8'	-2543	-2843.8	-2464.0	-2491.0	-2415.8	-2406.7	-2433.0	-2433.0
L8'-L7'	-2533	-2828.3	-2457.0	-2480.0	-2412.2	-2407.2	-2428.7	-2428.7
L7'-L6'	-1087	-1251.2	-1098.0	-1105.0	-1051.7	-1049.8	-1057.9	-1057.9
L6'-L5'	-1087	-1251.1	-1097.0	-1106.0	-1052.0	-1049.0	-1058.2	-1058.2
L5'-L4'	-137	-192.9	-149.0	-150.0	-113.5	-110.7	-112.2	-112.2
L4'-L3'	-137	-191.7	-148.0	-148.0	-112.2	-109.7	-110.9	-110.9
L3'-L2'	-190	-240.5	-200.0	-199.0	-112.2	-110.8	-109.2	-109.2
L2'-L1'	-190	-241.3	-203.0	-201.0	-112.7	-111.1	-109.7	-109.7

Table 13 Main Truss Diagonal Axial Forces After Step 2

Member	Member Axial Force (kips)							
	Design Plans	URS Designed (2003)	BSDI Designed (1965)		FHWA Designed (1965)		FHWA As-Built (2007)	
	Symmetric	Symmetric	West Truss	East Truss	West Truss	East Truss	West Truss	East Truss
U0-L1	-560	-646.1	-512.0	-539.0	-422.0	-397.3	-422.1	-422.1
U1-L1	-323	-416.2	-333.0	-325.0	-316.0	-316.0	-317.9	-317.9
U2-L1	-662	-732.4	-618.0	-632.0	-592.2	-589.0	-596.0	-596.0
U2-L2	266	246.7	211.0	209.0	221.8	219.4	219.5	219.5
U2-L3	192	191.9	155.0	174.0	135.9	138.5	136.5	136.5
U3-L3	-320	-336.0	-286.0	-292.0	-278.8	-280.1	-280.5	-280.5
U4-L3	321	341.5	309.0	300.0	314.1	314.0	316.5	316.5
U4-L4	234	206.1	170.0	175.0	184.8	185.9	182.9	182.9
U4-L5	-640	-730.1	-660.0	-655.0	-650.0	-647.9	-654.5	-654.5
U5-L5	-318	-347.9	-293.0	-297.0	-284.6	-284.9	-286.4	-286.4
U6-L5	883	981.7	872.0	873.0	852.3	851.5	858.1	858.1
U6-L6	275	276.9	238.0	242.0	243.9	242.7	241.5	241.5
U6-L7	-1174	-1378.6	-1192.0	-1199.0	-1179.3	-1178.0	-1187.8	-1187.8
U7-L7	-333	-369.7	-302.0	-307.0	-301.8	-299.5	-304.0	-304.0
U8-L7	1216	1359.6	1169.0	1179.0	1161.9	1157.8	1170.3	1170.3
U8-L8	-2527	-2867.7	-2255.0	-2540.0	-2219.2	-2215.5	-2230.8	-2230.8
U8-L9	1560	1767.8	1545.0	1559.0	1508.5	1505.4	1518.4	1518.4
U9-L9	-331	-359.3	-301.0	-306.0	-300.3	-299.6	-302.2	-302.2
U10-L9	-1680	-1985.3	-1736.0	-1751.0	-1682.9	-1679.6	-1694.1	-1694.1
U10-L10	271	290.3	255.0	258.0	256.0	255.3	253.6	253.6
U10-L11	1432	1624.6	1438.0	1450.0	1396.3	1393.8	1405.1	1405.1
U11-L11	-269	-307.1	-259.0	-262.0	-262.0	-261.3	-263.6	-263.6
U12-L11	-1215	-1380.8	-1225.0	-1235.0	-1179.0	-1177.1	-1186.5	-1186.5
U12-L12	270	268.5	241.0	245.0	237.4	236.8	234.9	234.9
U12-L13	834	905.8	799.0	805.0	778.5	777.5	783.4	783.4
U13-L13	-330	-327.8	-285.0	-260.0	-284.2	-283.6	-285.8	-285.8
U14-L13	-214	-271.6	-234.0	-235.0	-225.9	-226.0	-227.8	-227.8
U14-L14	244	234.7	197.0	198.0	191.7	191.3	190.0	190.0

Table 14 Main Truss Diagonal Axial Forces After Step 2 (con't)

Member	Member Axial Force (kips)							
	Design Plans	URS Designed (2003)	BSDI Designed (1965)		FHWA Designed (1965)		FHWA As-Built (2007)	
	Symmetric	Symmetric	West Truss	East Truss	West Truss	East Truss	West Truss	East Truss
U14-L13'	-214	-231.5	-205.0	-208.0	-202.0	-201.0	-203.5	-203.5
U13'-L13'	-330	-346.3	-283.0	-286.0	-290.7	-290.0	-293.0	-293.0
U12'-L13'	834	896.9	770.0	777.0	766.3	764.2	771.9	771.9
U12'-L12'	270	268.5	242.0	246.0	237.6	236.7	234.9	234.9
U12'-L11'	-1215	-1384.6	-1200.0	-1212.0	-1168.1	-1164.6	-1176.1	-1176.1
U11'-L11'	-269	-304.6	-261.0	-263.0	-261.5	-260.4	-263.1	-263.1
U10'-L11'	1432	1631.5	1425.0	1437.0	1391.5	1387.2	1400.6	1400.6
U10'-L10'	271	289.8	246.0	254.0	253.1	251.8	250.7	250.7
U10'-L9'	-1680	-1999.2	-1712.0	-1732.0	-1676.6	-1671.0	-1688.1	-1688.1
U9'-L9'	-331	-359.6	-306.0	-307.0	-300.0	-298.2	-301.9	-301.9
U8'-L9'	1560	1782.5	1542.0	1557.0	1507.6	1501.9	1517.7	1517.7
U8'-L8'	-2527	-2817.7	-2463.0	-2493.0	-2174.8	-2170.4	-2186.7	-2186.7
U8'-L7'	1216	1286.8	1111.0	1124.0	1110.8	1106.6	1119.2	1119.2
U7'-L7'	-333	-369.3	-304.0	-309.0	-299.1	-299.2	-301.3	-301.3
U6'-L7'	-1174	-1281.0	-1112.0	-1126.0	-1114.7	-1109.3	-1123.1	-1123.1
U6'-L6'	275	276.3	240.0	245.0	242.4	242.7	240.0	240.0
U6'-L5'	883	885.5	791.0	796.0	776.0	776.5	782.0	782.0
U5'-L5'	-318	-349.6	-300.0	-300.0	-283.8	-284.5	-285.6	-285.6
U4'-L5'	-640	-614.6	-552.0	-561.0	-560.7	-559.5	-565.5	-565.5
U4'-L4'	234	201.8	153.0	174.0	185.3	184.0	183.4	183.4
U4'-L3'	220	227.2	194.0	198.0	222.6	220.9	225.1	225.1
U3'-L3'	-320	-333.9	-284.0	-287.0	-279.4	-278.1	-281.2	-281.2
U2'-L3'	291	295.4	261.0	264.0	224.3	224.4	224.7	224.7
U2'-L2'	266	253.0	217.0	223.0	224.0	224.0	221.8	221.8
U2'-L1'	-771	-859.0	-735.0	-745.0	-688.3	-688.3	-692.1	-692.1
U1'-L1'	-323	-427.5	-332.0	-342.0	-321.9	-328.7	-323.8	-323.8
U0'-L1'	-1014	-1164.6	-996.0	-1004.0	-833.6	-831.5	-833.6	-833.6

Table 15 Comparison of Upper Chord Forces after Step 2 to those shown in the Design Plans

Member	Design Plans[1] (page 20) (kip)	FHWA Designed (1965) (kip)	Percent Difference	Magnitude Difference[a] (kip)
U0-U2	439	320	0.27	-119
U2-U4	-226	-250	-0.11	24
U4-U6	516	486	0.06	-30
U6-U8	1762	1695	0.04	-67
U8-U10	1551	1499	0.03	-52
U10-U12	-486	-484	0.00	-2
U12-U14	-1899	-1842	0.03	-57
U4'-U2'	-31	-65	-1.10	34
U2'-U0'	796	652	0.18	-144

Differences larger than 10% shaded gray

[a] – negative values mean the model predicts less than shown in the design plans

Table 16 Comparison of Lower Chord Forces after Step 2 to those shown in the Design Plans

Member	Design Plans[1] (page 20) (kip)	FHWA Designed (1965) (kip)	Percent Difference	Magnitude Difference[a] (kip)
L1-L3	80	148	-0.85	68
L3-L5	-18	10	1.58	-28
L5-L7	-1087	-1052	0.03	-35
L7-L8	-2533	-2467	0.03	-66
L8-L9	-2543	-2471	0.03	-72
L9-L11	-559	-504	0.10	-55
L11-L13	1311	1312	0.00	1
L13-L13'	2036	1926	0.05	-110
L5'-L3'	-137	-114	0.17	-23
L3'-L1'	-190	-113	0.41	-77

Differences larger than 10% shaded gray

[a] – negative values mean the model predicts less than shown in the design plans

Table 17 Comparison of Vertical Forces after Step 2 to those shown in the Design Plans

Member	Design Plans[1] (page 20) (kip)	FHWA Designed (1965) (kip)	Percent Difference	Magnitude Difference[a] (kip)
U1-L1	-323	-329	-0.02	6
U2-L2	266	224	0.16	-42
U3-L3	-320	-281	0.12	-39
U4-L4	234	185	0.21	-49
U5-L5	-318	-286	0.10	-32
U6-L6	275	243	0.11	-32
U7-L7	-333	-302	0.09	-31
U8-L8	-2527	-2223	0.12	-304
U9-L9	-331	-301	0.09	-30
U10-L10	271	256	0.06	-15
U11-L11	-269	-263	0.02	-6
U12-L12	270	237	0.12	-33
U13-L13	-330	-291	0.12	-39
U14-L14	244	191	0.22	-53

Differences larger than 10% shaded gray

[a] – negative values mean the model predicts less than shown in the design plans

Table 18 Comparison of Diagonal Forces after Step 2 to those shown in the Design Plans

Member	Design Plans[1] (page 20) (kip)	FHWA Designed (1965) (kip)	Percent Difference	Magnitude Difference[a] (kip)
U0-L1	-560	-421	0.25	-139
U2-L1	-662	-594	0.10	-68
U2-L3	192	139	0.27	-53
U4-L3	321	313	0.02	-8
U4-L5	-640	-648	-0.01	8
U6-L5	883	851	0.04	-32
U6-L7	-1174	-1176	0.00	2
U8-L7	1216	1159	0.05	-57
U8-L9	1560	1512	0.03	-48
U10-L9	-1680	-1688	0.00	8
U10-L11	1432	1399	0.02	-33
U12-L11	-1215	-1182	0.03	-33
U12-L13	834	780	0.06	-54
U14-L13	-214	-227	-0.06	13
U4'-L3'	220	223	-0.01	3
U2'-L3'	291	224	0.23	-67
U2'-L1'	-771	-687	0.11	-84
U0'-L1'	-1014	-835	0.18	-179

Differences larger than 10% shaded gray

[a] – negative values mean the model predicts less than shown in the design plans

Table 19 Main Truss Vertical Reactions for the FHWA models After Step 2

	Vertical Reaction Force (kips)			
	Design Plans[1] (Sheet 20)	Designed (1965)	As-Built (2007)	Detailed As-Built (2007)
Pier 5 East (node 8659)	1098	946	951	991
Pier 5 West (node 205)	1098	982	987	1029
Pier 6 East (node 40119)	3660	3584	3608	3733
Pier 6 West (node 421)	3660	3590	3614	3739
Pier 7 East (node 649)	3589	3514	3538	3664
Pier 7 West (node 666)	3589	3522	3547	3673
Pier 8 East (node 250)	1446	1295	1300	1354
Pier 8 West (node 7)	1446	1289	1294	1348
TOTAL	19,586	18,722	18,839	19,531

Table 20 Main Truss Vertical Reactions Through Time for the Designed (1965) Model

	Step 1	Step 2	Step 3	Step 4
Pier 5 East (node 8659)	953.3	946	1261	1224
Pier 5 West (node 205)	907	982	1323	1289
Pier 6 East (node 40119)	3255	3584	4454	4632
Pier 6 West (node 421)	3265	3590	4437	4769
Pier 7 East (node 649)	3187	3514	4343	4327
Pier 7 West (node 666)	3195	3522	4357	4327
Pier 8 East (node 250)	1214	1295	1662	1648
Pier 8 West (node 7)	1209	1289	1628	1602
Sum	**17185**	**18722**	**23465**	**23816**

Table 21 Main Truss Vertical Reactions Through Time for the As-Built (2007) Model

	Step 1	Step 2	Step 3	Step 4
Pier 5 East (node 8659)	867	951	1265	1228
Pier 5 West (node 205)	911	987	1328	1294
Pier 6 East (node 40119)	3279	3608	4478	4657
Pier 6 West (node 421)	3289	3614	4461	4792
Pier 7 East (node 649)	3210	3538	4367	4351
Pier 7 West (node 666)	3220	3547	4382	4352
Pier 8 East (node 250)	1218	1300	1667	1653
Pier 8 West (node 7)	1214	1294	1632	1606
Sum	**17208**	**18839**	**23580**	**23933**

Table 22 Main Truss Vertical Reactions Through Time for Detailed As-Built (2007) Model

	Step 1	Step 2	Step 3	Step 4
Pier 5 East (node 8659)	907	991	1273	1263
Pier 5 West (node 205)	953	1029	1328	1349
Pier 6 East (node 40119)	3404	3733	4577	4748
Pier 6 West (node 421)	3414	3739	4575	4892
Pier 7 East (node 649)	3336	3664	4474	4446
Pier 7 West (node 666)	3346	3673	4501	4456
Pier 8 East (node 250)	1272	1354	1695	1685
Pier 8 West (node 7)	1268	1348	1662	1643
Sum	**17900**	**19531**	**24085**	**24482**

Table 23 Axial Forces of U10 Members Through All Steps

Member	Axial Force (kips)				
	After Step 1 (Steel + wet concrete)	After Step 2 (Add original barriers)	After Step 3 (Add deck thickness and modified barriers)	After Step 4 (Add construction and traffic loads)	Design Load (from sheet 20 of design plans)
U10U9W	1420.0	1560.2	1926.1	1989.4	2179
U10U9E	1417.2	1557.7	1922.8	1952.7	2179
U10L9W	-1593.0	-1747.6	-2163.2	-2388.6	-2288
U10L9E	-1589.3	-1744.4	-2160.5	-2291.3	-2288
U10L10W	234.8	265.5	333.1	398.8	540
U10L10E	233.8	264.8	332.7	373.6	540
U10L11W	1333.0	1458.4	1796.7	1933.1	1975
U10L11E	1330.3	1455.9	1794.3	1870.9	1975
U10U11W	-407.9	-436.0	-520.3	-647.6	-972
U10U11E	-407.5	-435.7	-521.3	-604.6	-972

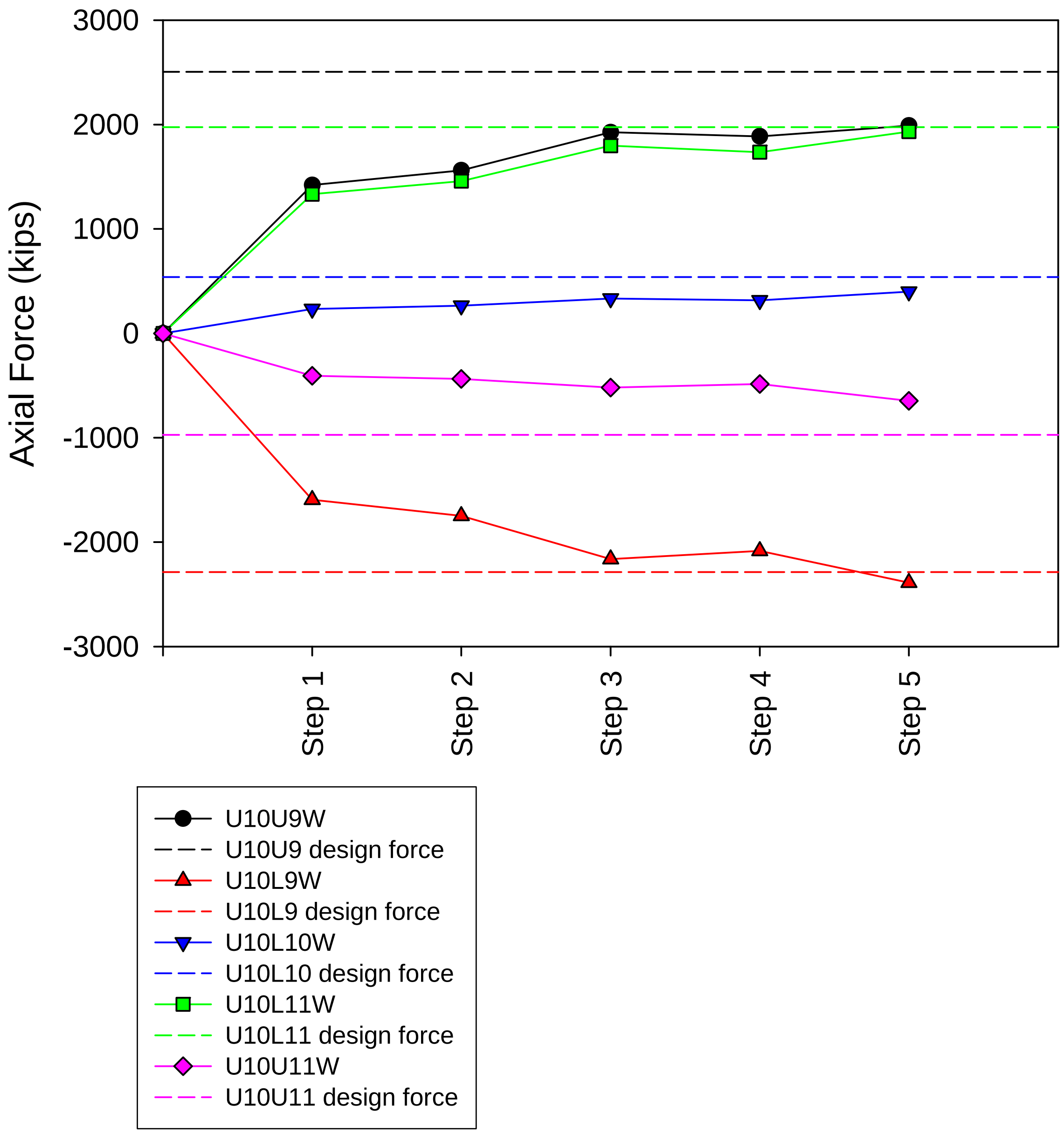

Figure 20. Axial force traces of U10 members.

CHAPTER 3. FHWA DETAILED MODEL

In order to study connection details involved in the collapse, a more refined model was constructed by enhancing the original global model. This model embedded localized models of the U10W, U10E, L11E, and L11W joints. The members and gussets were meshed with shell elements within the local area around each connection. This detail model was used to evaluate the effects of thermal loads, corrosion, initial imperfections, and gusset plate thickness. The following section will briefly describe this model and some select results.

MODEL DESCRIPTION

The global stick model described in the previous chapter was modified to investigate the effects of the local models embedded within it. Figure 21 shows a view of the entire detailed model in which the local model of the L11W connection can be seen. The localized U10 and L11 models were made entirely of S4R shell elements and can be seen in Figures 22-23.

At each connection, the main truss members were extended for 36-60 inches (depending on the member) beyond the gusset plate to ensure there were no localized stress effects near the connection due to the beam-to shell element transition. To make this transition, the ends of the shell members were capped with shell elements given "rigid-like" material properties. These rigid plate elements were given a thickness of 2 inches and a material modulus of 29,000 ksi.

Rivet holes were not explicitly modeled in either the gusset plates or the truss members. Initially rivet holes were included, however it made the mesh too dense to analyze the models in a timely manner. Instead, a node was purposely placed at the center of each rivet in both the gusset and main member plates. A rigid link between these adjoining nodes was used to represent the rivet. The rigid link element was the Abaqus *MPC BEAM which is a multi-point constraint that locks all the degrees of freedom together between the linked nodes.

Since the shell elements reduce the 3D geometry down to plate mid-planes, the mesh could deform unrealistically due to lack of contact between the plates. Explicit contact modeling was avoided due to potential convergence issues that could slow down the analysis. Instead, nonlinear springs were meshed between the truss members and the gusset plate around the perimeter of the truss members at the points of contact. These springs were assigned a low opening stiffness of 0.0001 kips/inch and a high closing stiffness of 10000 kips/inch. Therefore adjoining plates could pull apart easily yet push on each other with a high stiffness. Figure 24 is a view of compression diagonal of the U10 connection showing the aforementioned rivet links and the nonlinear contact springs.

MATERIAL MODELS

The local imbedded portion of the models utilized the nonlinear material analysis capabilities of Abaqus. This was accomplished using the Abaqus *PLASTIC command. This command utilizes the Von Mises yield criterion with isotropic hardening in the nonlinear iteration. The command requires the user to enter true stress/strain data from a uniaxial tension test. As part of the investigation, tension tests were performed from the material of the four U10 gusset plates, and all truss members framing into the U10 connection.

The tension test results showed little variation between samples from all four gusset plates, therefore a single material model was used for all grade 50 material. The tension test results for the grade 36 and grade 50 material in the truss members were not yet available. Therefore, typical material properties were assumed for the truss members. As will be shown in the results sections, the truss members remained elastic and all nonlinear material behavior was concentrated in the gusset plates. Therefore the typical material properties assumed for the members have no effect on model results.

The stress/strain characteristics of the three materials used for this model are shown in Figure 25. The nonlinear material properties were implemented in Abaqus using the *PLASTIC command which assumes an isotropic hardening model. Abaqus also requires the input to be in terms of true stress and strain, not engineering strain. Therefore the curve for the U10 material shown in Figure 25 is in terms of true stress because it was based on test data. The other two models presented in this figure were in terms of engineering stress because these materials were not exclusively tested at the time the modeling occurred and the engineering stress relationship was entered into the Abaqus input deck. The 36 ksi yield material model (ASTM A36) was assumed because the U10-U12 and L9-L11 members were made from that material. The 100 ksi yield material (ASTM A514) was used for the models that explored what would happen if higher strength material was used for the gussets.

RESULTS FROM DETAILED MODEL

For purposes of this report only selected data is presented from the model. Results are limited to those considered relevant to the investigation recalling that evidence from the collapse site suggests that the failure initiated in the U10 connection.

For the remainder of this document, reference will be made to the A-A and B-B planes where free body checks are made in the U10 and L11 connections. These describe two of the fundamental cross-sectional failure planes a designer might use to check a gusset plate in design. Both of these planes are taken through the gross section away from the effect of rivet holes. Obviously a thorough design check of a gusset plate will involve many more section planes through both the gross and net sections. The A-A plane is the horizontal plane running along the edge of the chord members and B-B is a vertical plane running along side the side edge of the vertical member. The A-A and B-B planes are shown in Figure 26 for both the U10 and L11 connections. Also shown in this figure are reference lines, drawn to scale, that define the edge distance nomenclature used in many future graphs.

Figure 27 shows three Von Misses stress contour plots of the U10W connection, west plate. The contours were scaled from 51.5 ksi (the yield stress of this material) to 80 ksi. Therefore, any stress less than 51.5 ksi plots as black and shades of blue represent areas that exceed the Von Mises yield criteria. Three contour plots are presented at different stages in the bridge's life starting from immediately after construction (Step 2: considers weight of steel, original deck and barriers), after the deck thickness increased and modified barriers were installed (Step 3), and with the construction and traffic loads known to be on the bridge at collapse (Step 4). These plots show the surface stresses (accounting for membrane and bending stresses) and all contours are for the inner surface of the connection. This plot shows immediately after the bridge was constructed, the gusset plate material was already at its yield point in a localized region at the base of the compression diagonal member, despite being designed using an allowable stress philosophy where yielding should be prevented. Over the life of the bridge the dead load increased by 24% from increased deck thickness and modified stocky barriers and this extra load greatly increased the area where the material was at its yield point along the A-A plane and around the base of the compression diagonal. Once the construction and traffic loads were applied, the area at yield increased even further, extending nearly across the entire A-A plane. Note, that contours are only presented for the U10W-west plate. While trends are similar in the other three plates, the reader should understand that the yield patterns may be slightly different at other locations..

Similarly, Figure 28 plots the Von Mises stress contours for the L11W-west plate between values of 51.5-80 ksi. Again, shades of blue represent areas that are at the Von Mises yield criteria. Similar to the U10 connection, small areas of the L11 gusset plate are at its yield strength under the weight of the bridge immediately after construction. Also similar to the U10 connection, the area of the L11 gusset plate at the yield point increases as load is added to the bridge. However, the area of yielded material is smaller and much more localized compared to the U10 connection.

It should be noted that while Figures 27 and 28 show significant areas of the gusset plates are at their yield point, little deformation is occurring in the joint. The elastic material surrounding the yielded area constrains the yielded material from undergoing plastic flow. Therefore, the presence of yielded material does not represent total failure of the gusset plate.

Figures 29-32 are a series of plots showing the normal, shear, and Von Mises stress distributions along the A-A plane at mid-thickness for all four gusset plates at location U10 at the end of step 4 (all dead and live load known to be on bridge at collapse). It should be mentioned that all the shell elements used in the local connection modeling were given outward normal definitions pointing away from the connection itself, this explains the sign difference of the shear plots between the east and west plates. The plateaus shown in the Von Mises plots indicate a significant portion of the gusset was at its yield strength consistent with the yielding shown in the contour plots. The normal stress plots show the stress caused by bending moment and axial force across the free body cut at section A-A. Using a beam bending analogy, one would expect linear normal stress distribution across this plane. The normal stress distribution generally follows the linear beam bending analogy except at the edges of the plate. The shear distribution along the A-A plane shows a plateau similar to the Von Mises stress distribution with a magnitude close to the 29.9 ksi shear yield strength of the gusset plate. Therefore, as would be expected, shear being applied to the A-A plane appears to dominate the capacity of the U10 connection.

Figures 33-36 show similar plots along the B-B free-body section plane. There are two distinct regions of behavior along this section plane. The top region of the gusset serves primarily as a chord splice plate and additional internal splice plates share a portion of the total force. In the lower region, all of the member forces flow through the gusset plates. The shear stress below the top chord is close to the 29.9 ksi shear yield strength over a significant portion of the plate. The shear stress is lower in the top chord splice region since the internal splice plates take a portion of the load. Similarly, the normal stress distribution shows two distinct regions of behavior. A relatively uniform axial stress distribution can be observed in the top chord splice region. There appears to be more of a bending stress distribution across the lower portion of the plate. This illustrates the complexity involved with gusset plate design.

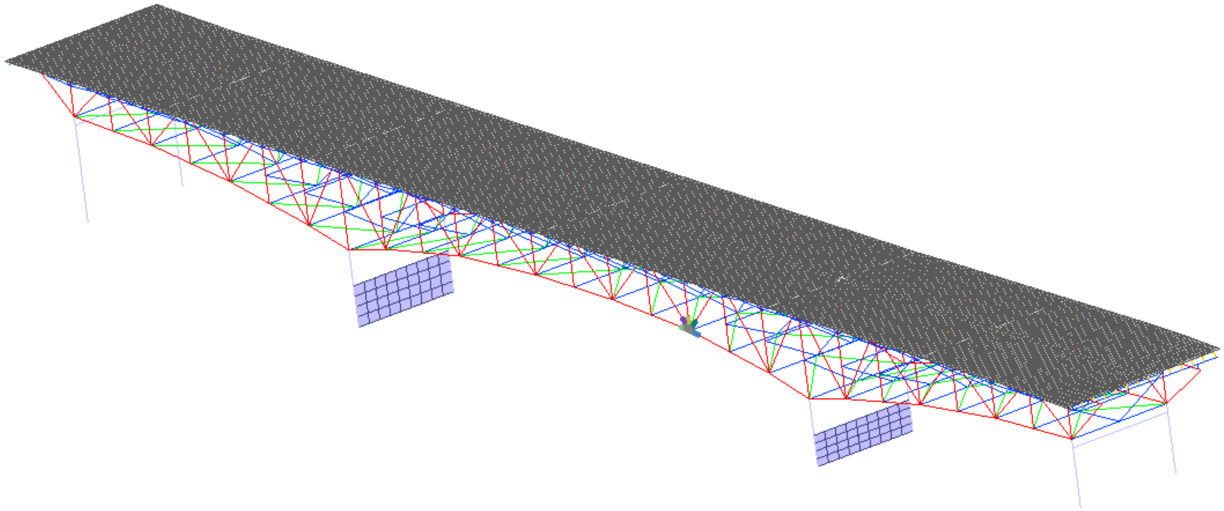

Figure 21. Entire TFHRC model.

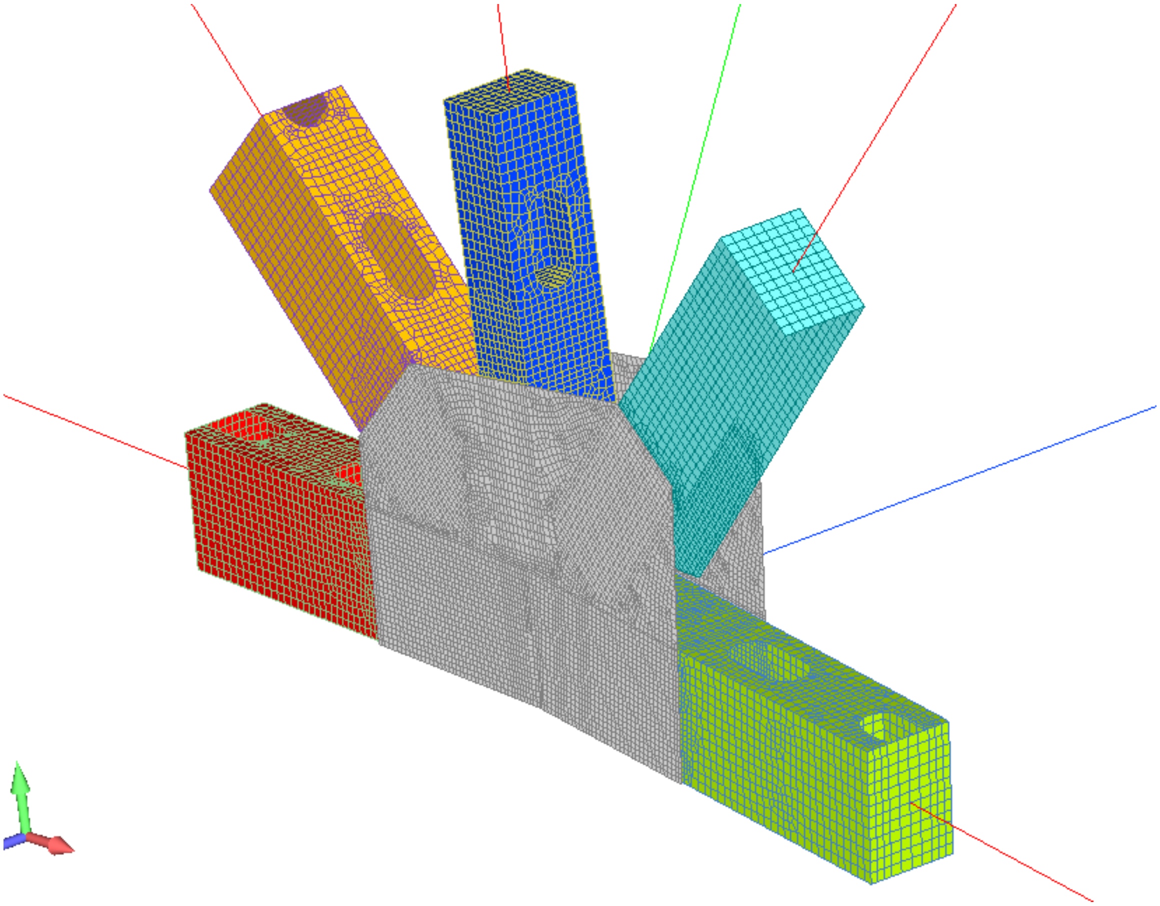

Figure 22. Local view of L11 connection.

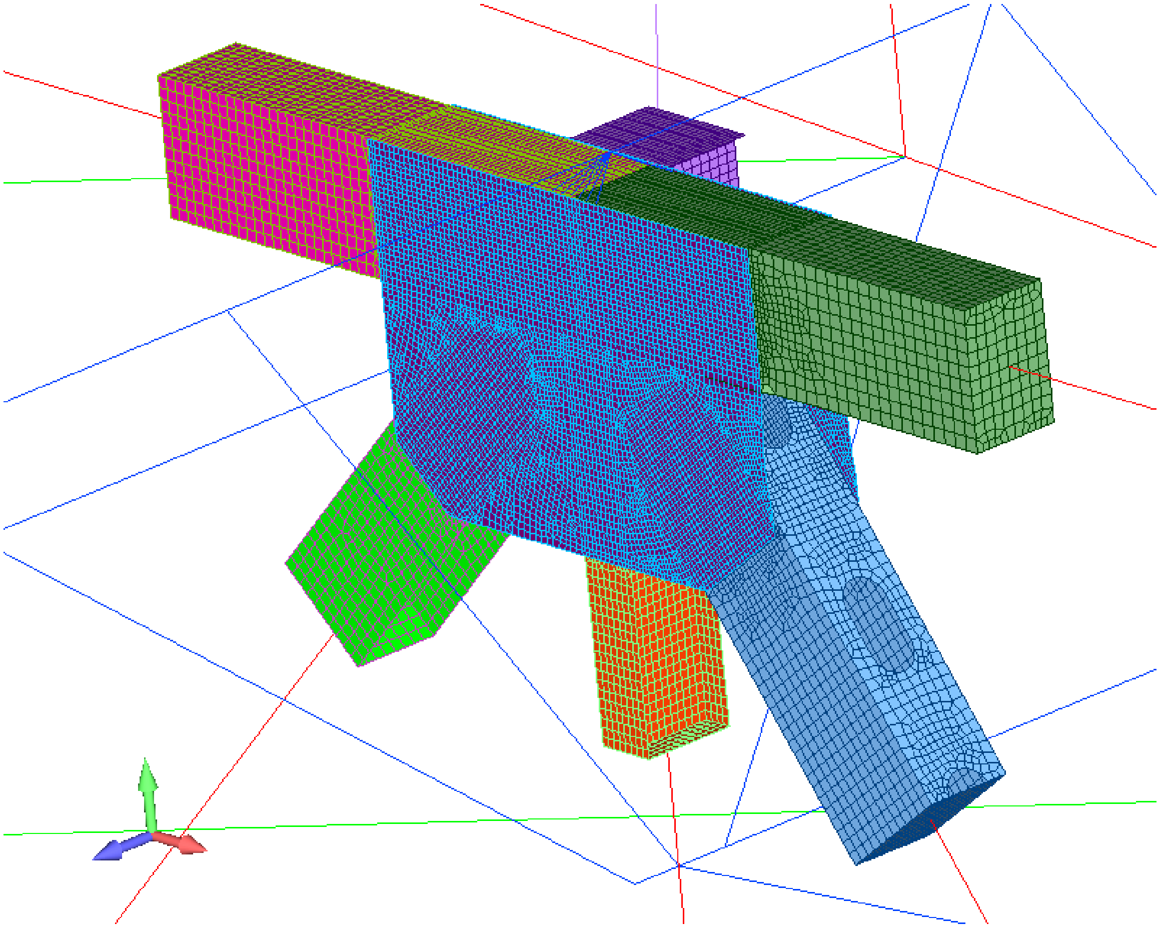

Figure 23. Local view of U10 connection.

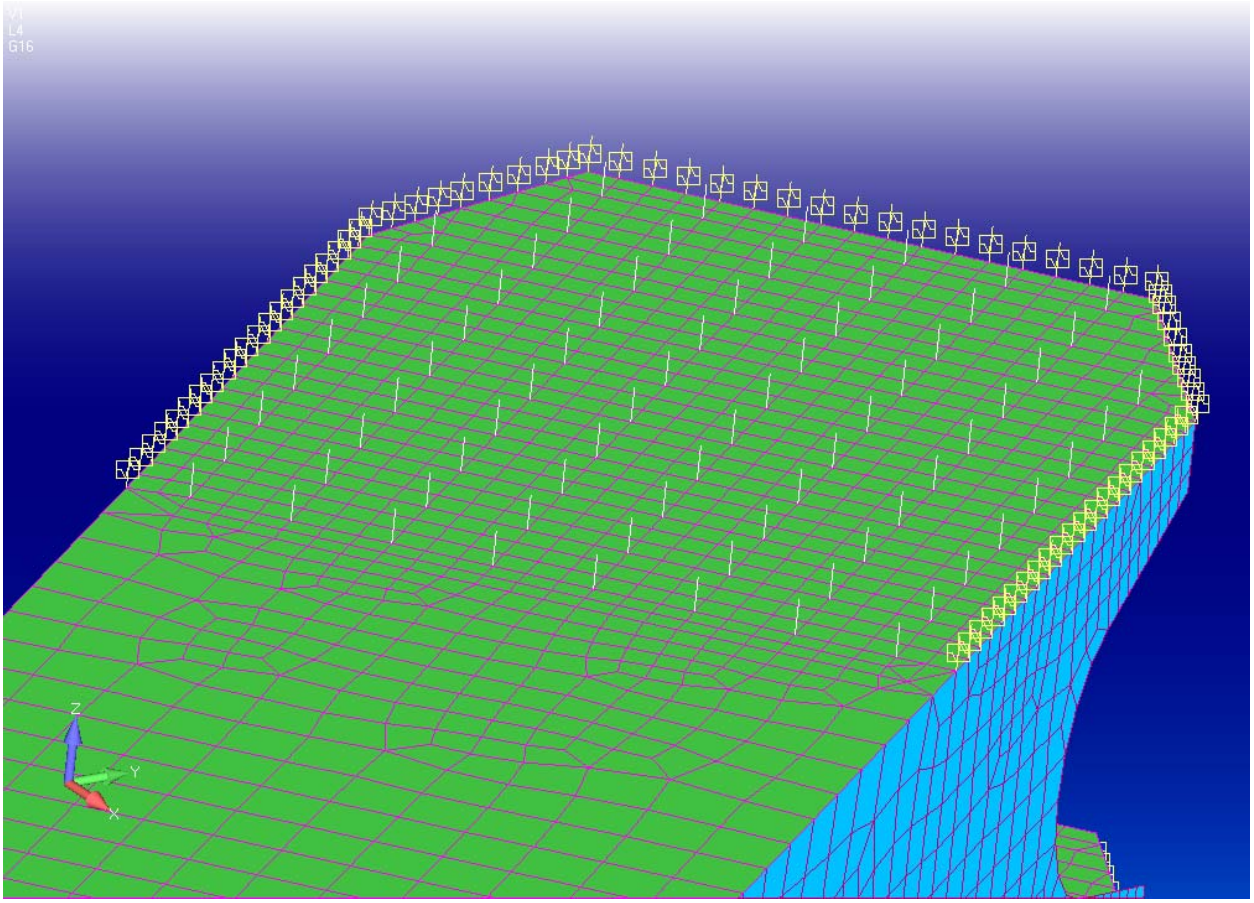

Figure 24. View of U10L9 diagonal showing rivet links and nonlinear contact springs.

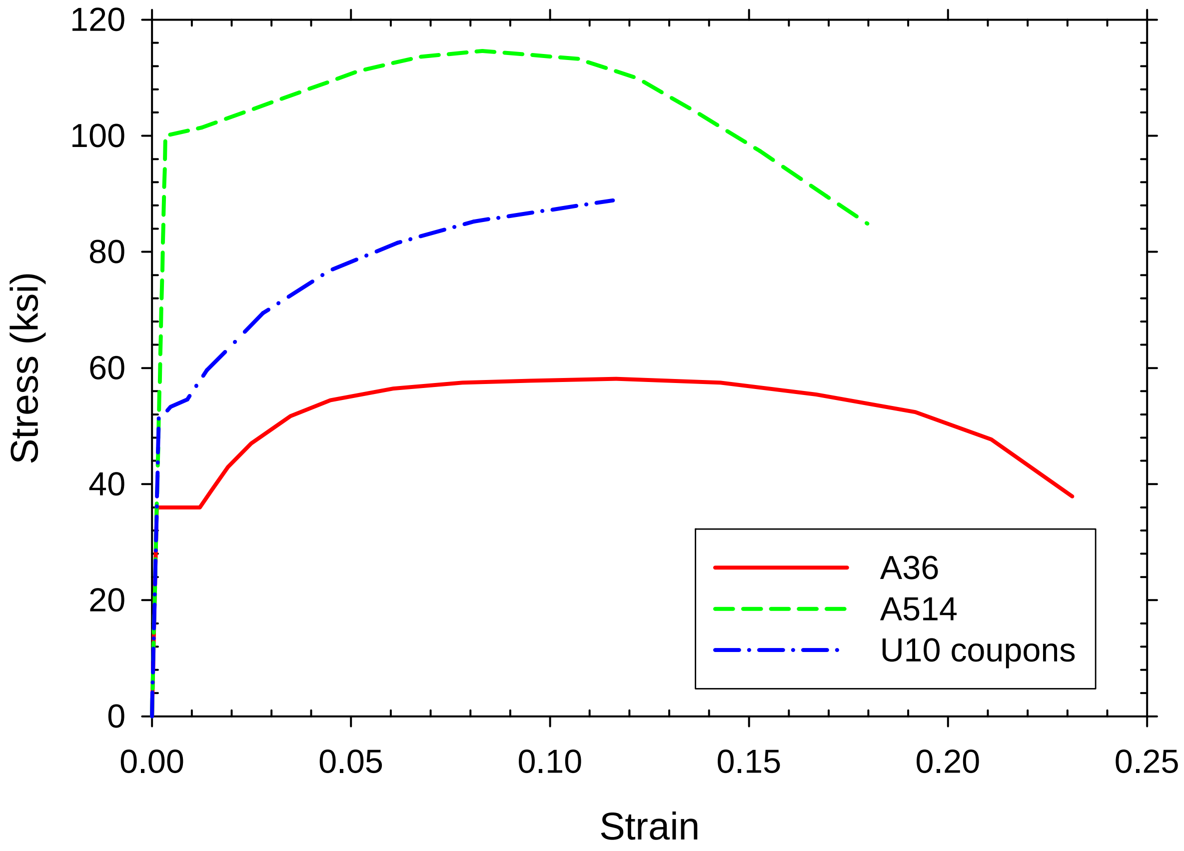

Figure 25. Material models used the detailed model.

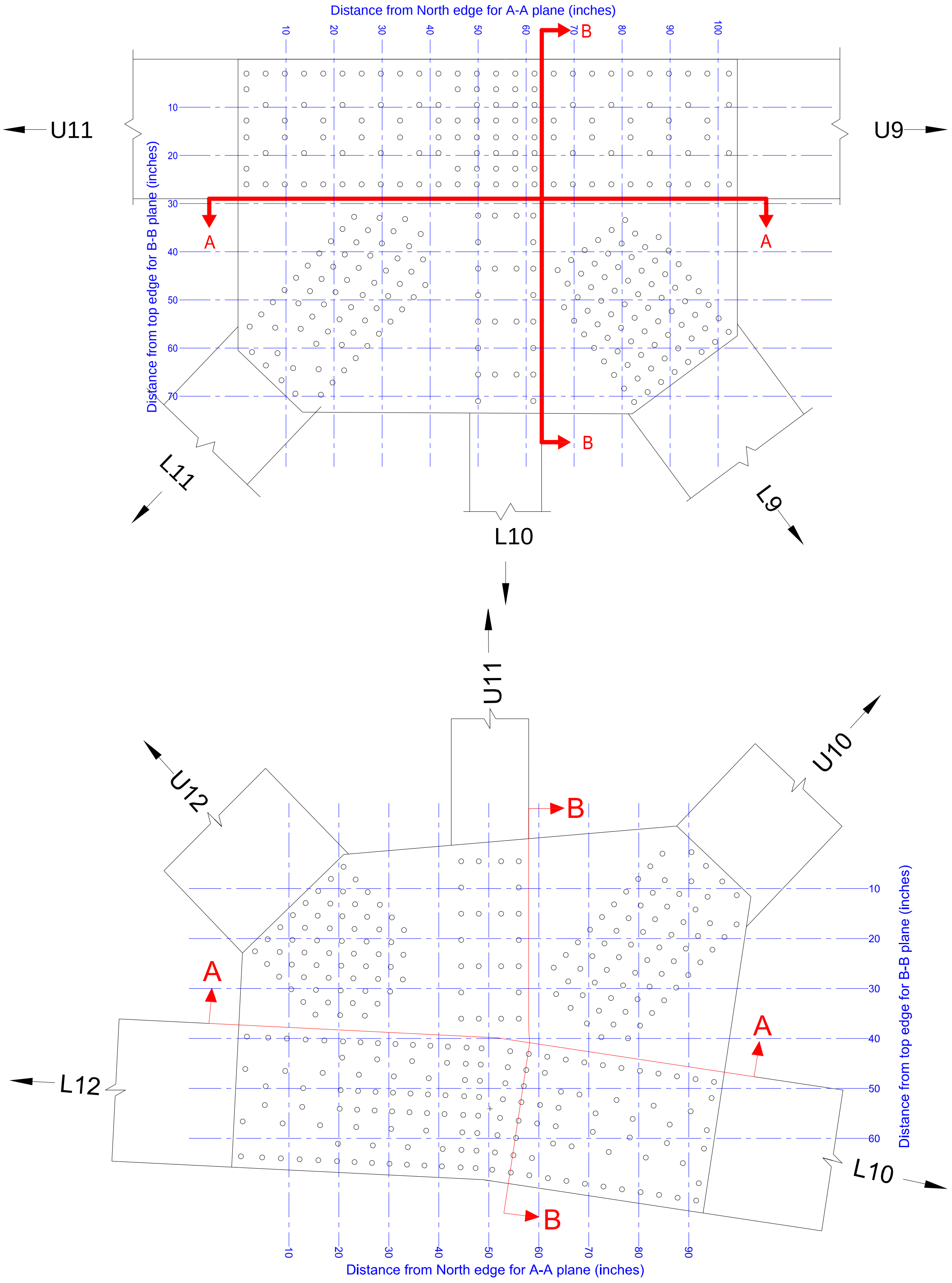

Figure 26. Reference schematic of A-A and B-B planes for U10 (top) and L11 (bottom) connections.

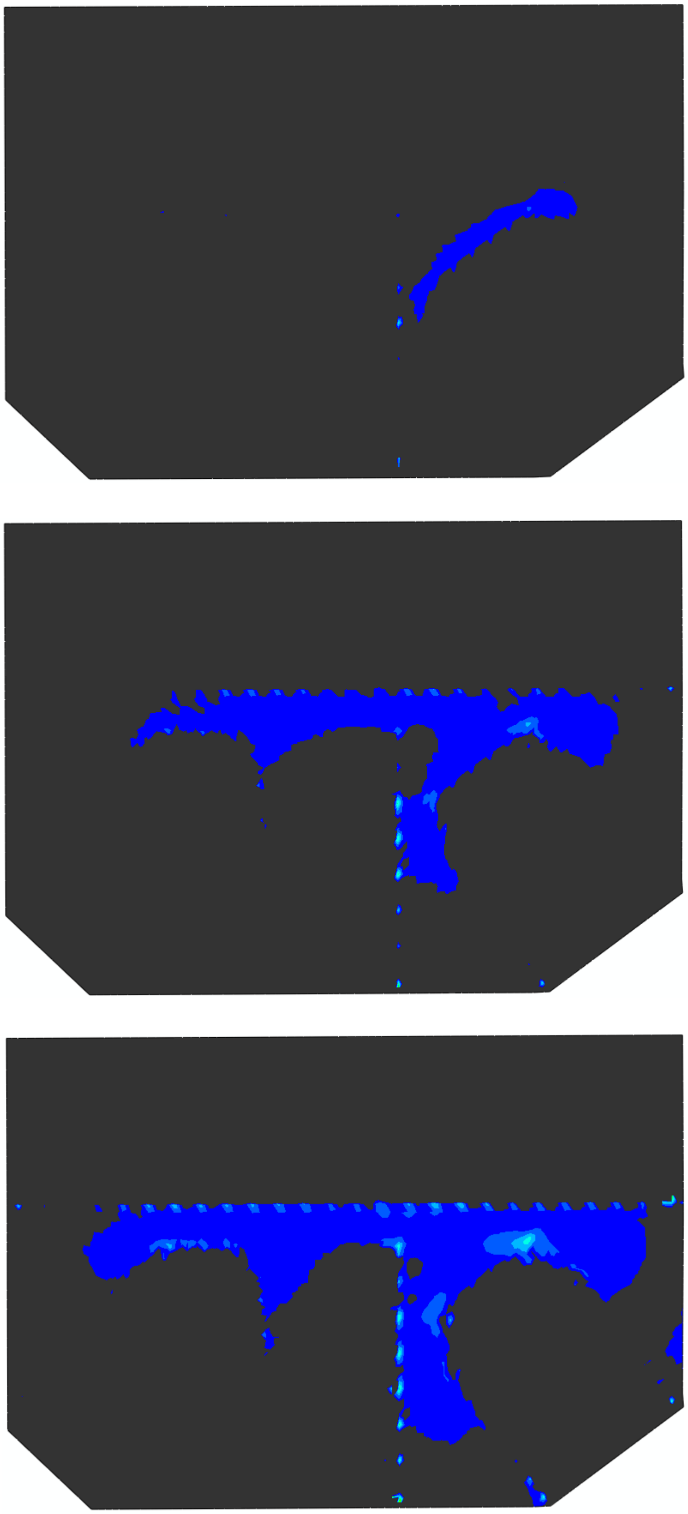

Figure 27. Von Mises stress contours of U10W-W plate from immediately after construction (top), after the deck thickness increased and barriers were modified (middle), and with the construction/traffic loads in place (bottom).

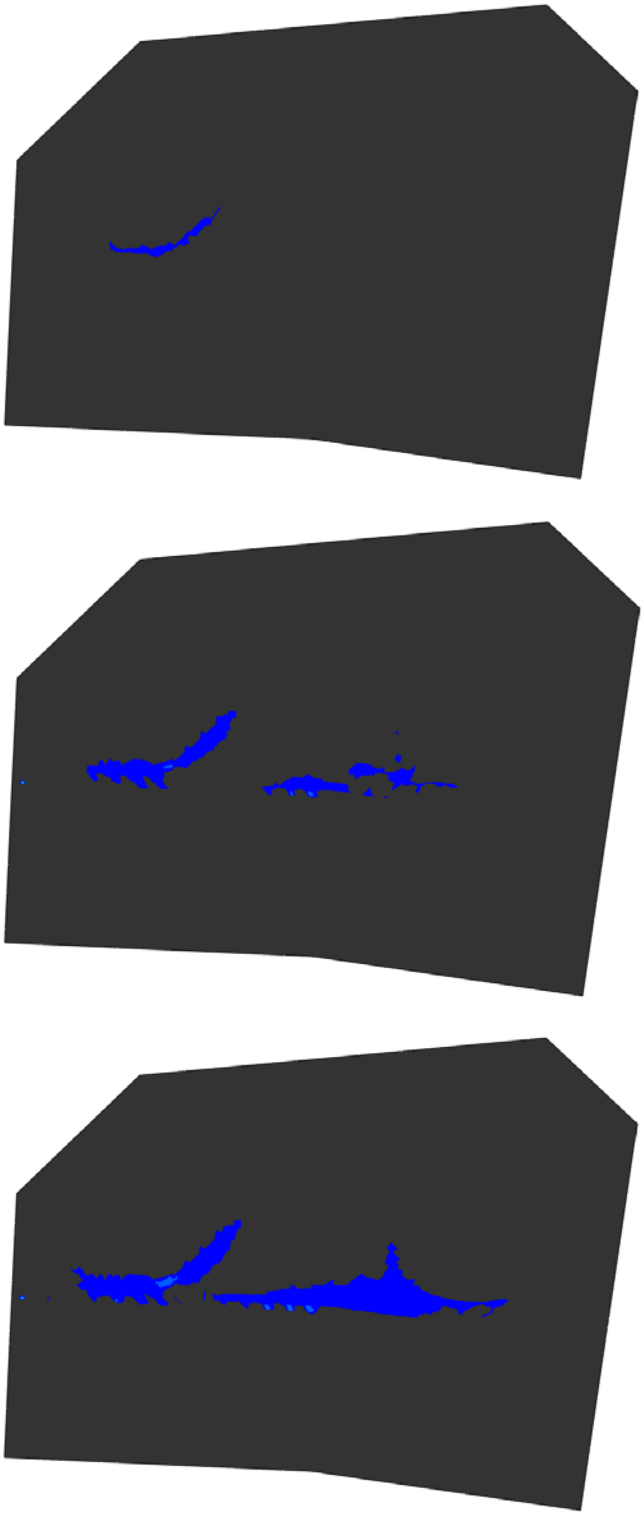

Figure 28. L11 Von Mises stress contours from immediately after construction (top), after the deck thickness increased and barriers were modified (middle), and with the construction/traffic loads in place (bottom).

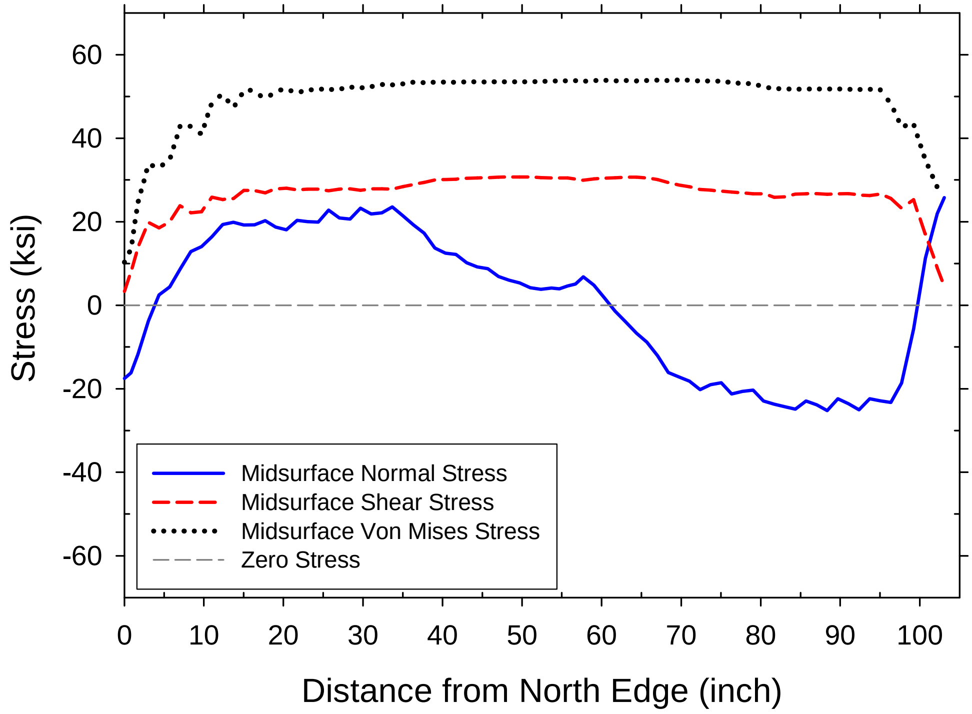

Figure 29. Mid-thickness normal and shear stresses on A-A plane for U10W-west plate.

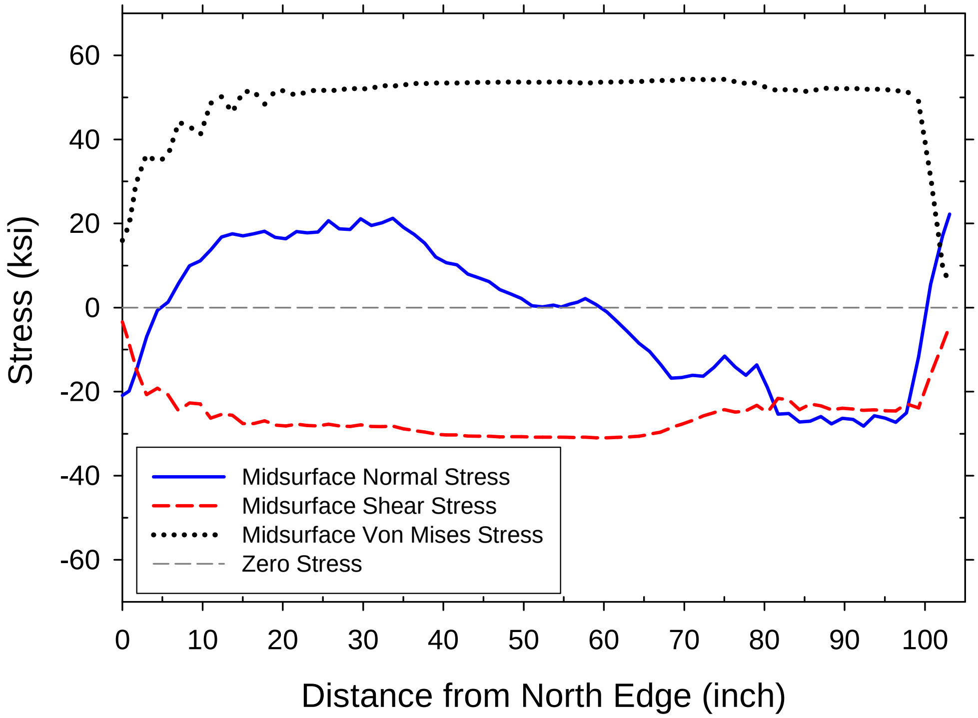

Figure 30. Mid-thickness normal and shear stresses on A-A plane for U10W-east plate.

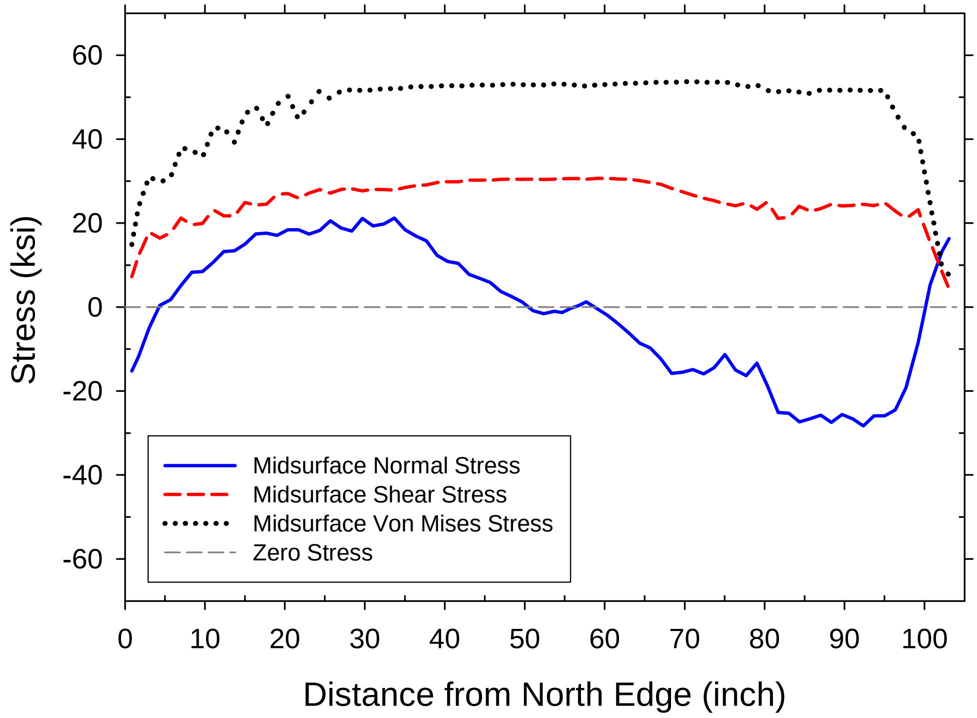

Figure 31. Mid-thickness normal and shear stresses on A-A plane for U10E-west plate.

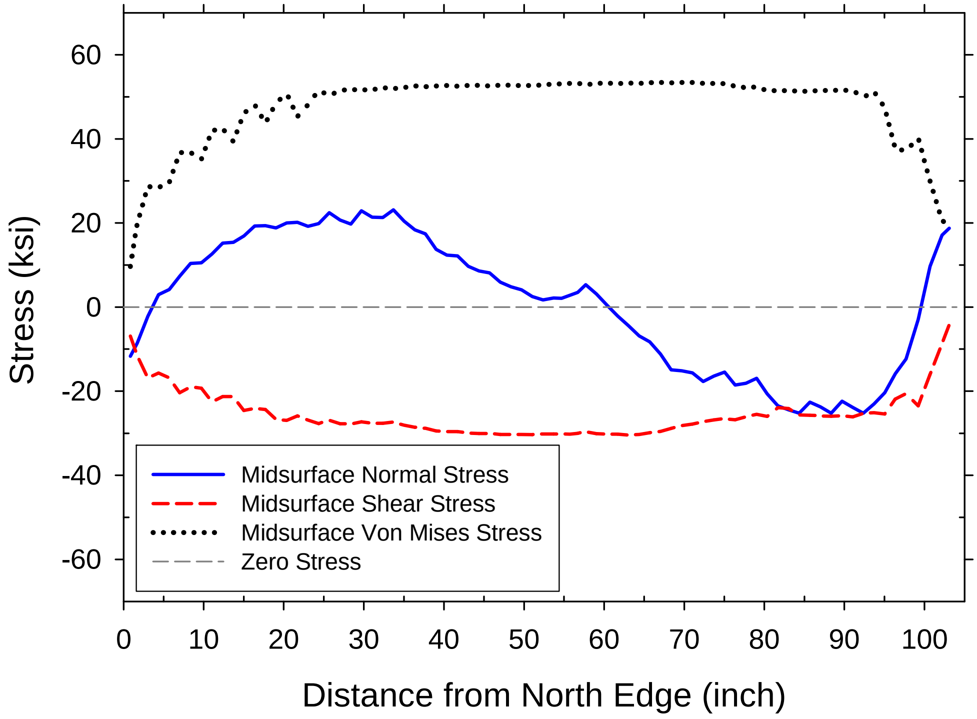

Figure 32. Mid-thickness normal and shear stresses on A-A plane for U10E-East plate.

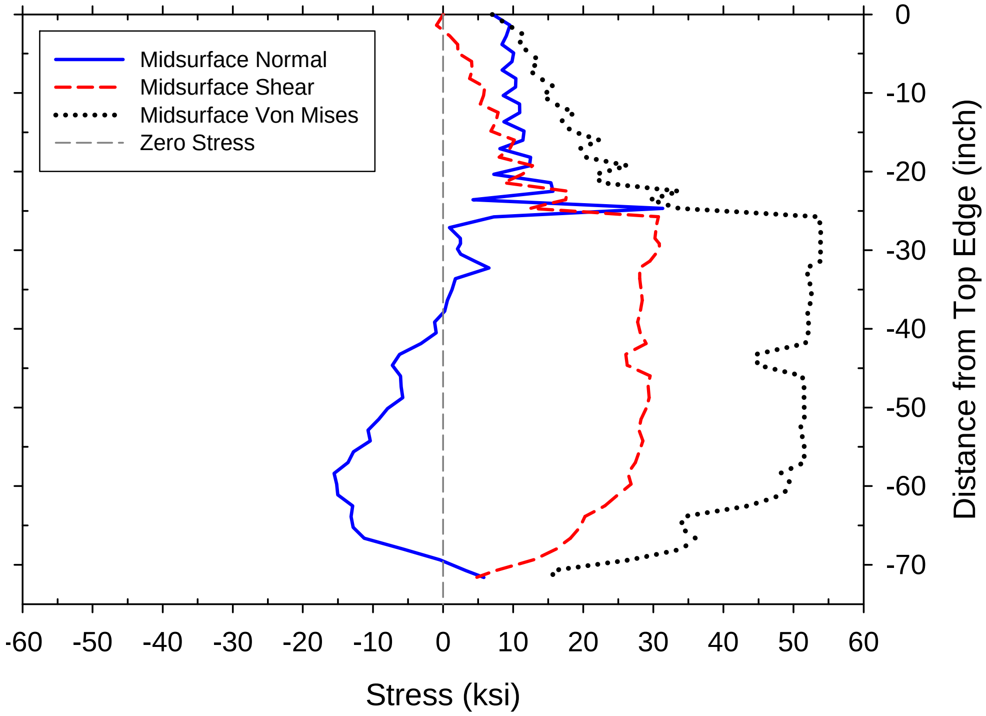

Figure 33. Mid-thickness normal and shear stresses on B-B plane for U10W-west plate.

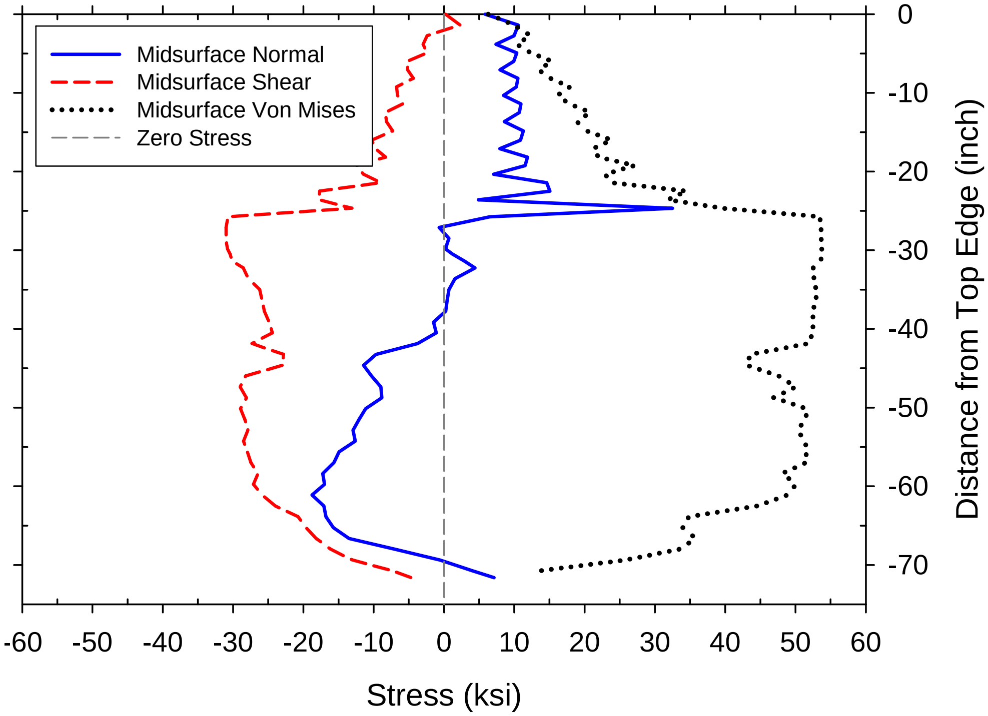

Figure 34. Mid-thickness normal and shear stresses on B-B plane for U10W-east plate.

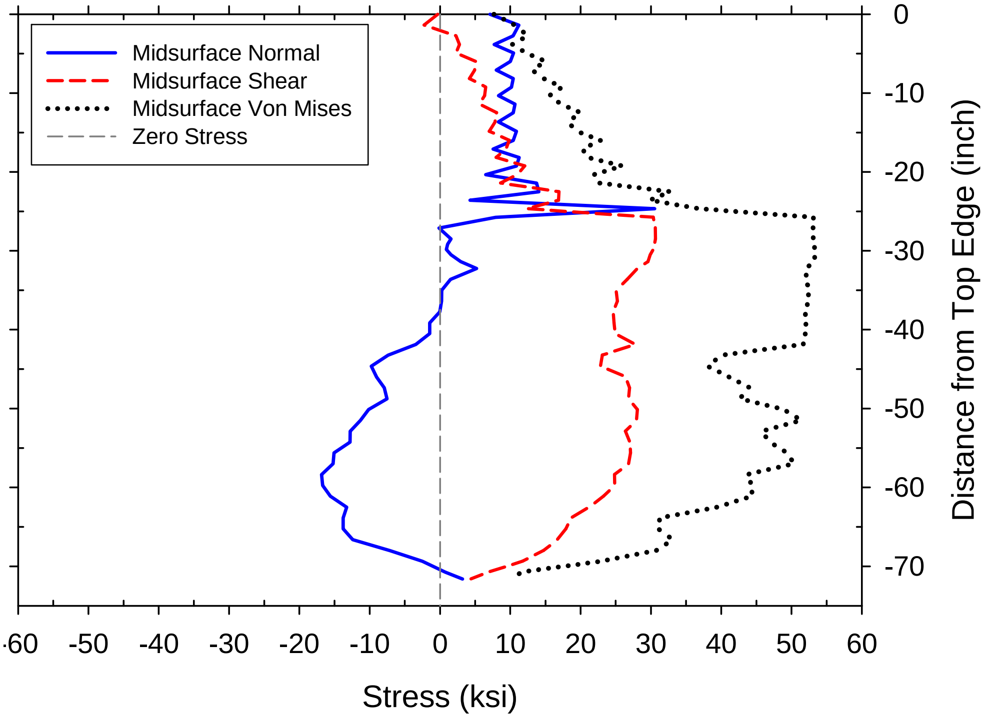

Figure 35. Mid-thickness normal and shear stresses on B-B plane for U10E-west plate.

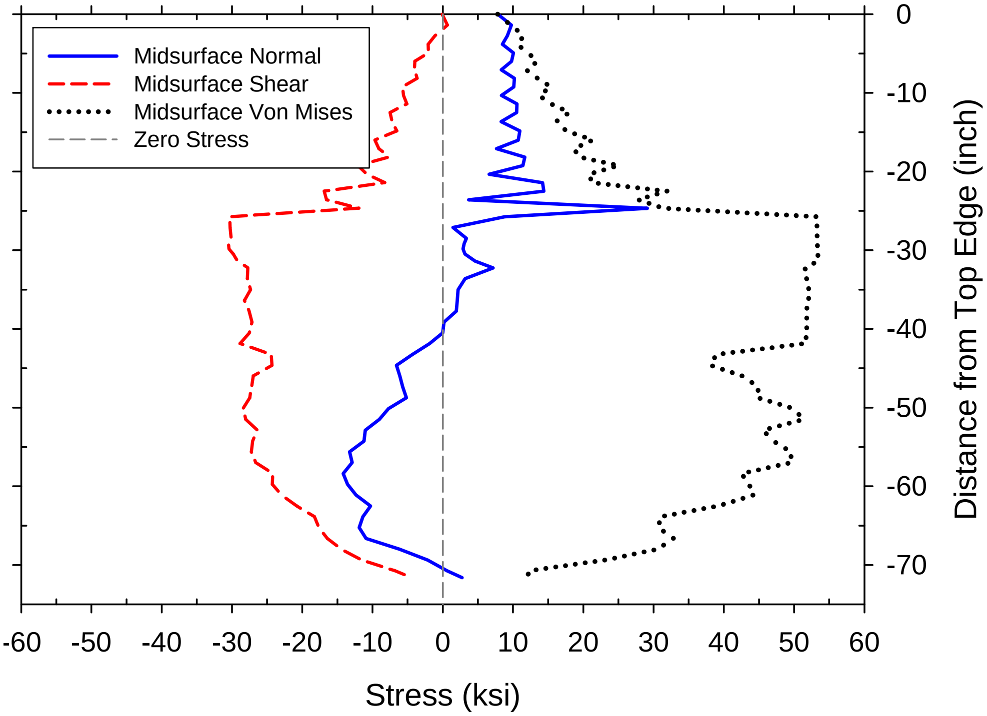

Figure 36. Mid-thickness normal and shear stresses on B-B plane for U10E-east plate.

CHAPTER 4. CORROSION AT JOINT L11

Some section loss due to corrosion was noted both in the inspection reports and through examination of the collapsed bridge wreckage for the gusset plates at joint L11. Examination of the wreckage points to joint U10 as the primary failure initiation site. However, since a moment connected truss is an indeterminate structural system, total failure can only occur when a collapse mechanism develops. Since damage was noted at L11 and it is adjacent to the U10 joint, the model was used to investigate any possible simultaneous mechanism mode of failure. The model also looked at the possibility that L11 was the primary failure initiation site.

FORENSIC EXAMINATION OF GUSSET PLATES

The NTSB provided a write-up of the L11 gusset condition post-collapse[9]. Thickness loss measurements were taken at one inch intervals along the width of the L11 gusset plates along the A-A plane at the edge of the lower chord members. Figure 37 shows the thickness profiles of the corroded plane in the four L11 gussets. The L11 gusset plates fractured along the A-A plane at some point in the collapse sequence, and the resulting damage made thickness measurement difficult in some parts of the plate. This explains the missing data in Figure 37 because either the plate no longer existed or the measurement was not physically possible. It should be noted that the L11 joints were severely damaged during the latter stages of collapse since they were crushed by the weight of the bridge. The forensic examination suggests the A-A plane fracture occurred late in the collapse event. The FE analysis was used to determine if shear yielding occurred along the A-A plane at an earlier stage prior to fracture.

To simplify modeling, a uniform distribution of the corrosion loss was initially assumed along the A-A plane. The results indicated that further refinement of the model was not necessary, therefore no detailed modeling of the corrosion pattern was attempted. Table 24 shows the average thickness calculated from the data shown in Figure 37. The averages were calculated using the given data and does not account for the missing data. Considering the accuracy of the thickness measurements, a uniform corrosion loss of 0.1 in. was assumed for all four gusset plates. This can be considered conservative based on the presented data.

MODELING OF THE CORROSION

The corrosion was modeled by duplicating a line of shell elements in the gusset directly above the lower chord members. The elements along this line were 0.5 inches tall above the top surface of the lower chord members. The duplicate elements were assigned different material thickness such that the sum totaled 0.5 inch, which was the original thickness of the plate. This allowed the duplicated elements to be removed during one of the model steps to simulate a structural change over time. The group of elements representing the corrosion was assigned a thickness of 0.1 inches and the duplicate elements were 0.4 inches. All four gusset plates were modeled identically such that all four of the plates were going to have a line of elements, 0.1

inches thick, instantaneously removed to represent the corrosion. A picture of the L11 connection showing the corrosion element group is shown in Figure 38.

The corrosion elements were removed in an additional analysis step after the additional dead load from thicker deck and new barriers was added but before adding the construction/traffic loads. The elements were removed using the Abaqus *MODEL CHANGE command which removes the element stiffness and redistributes the internal strain energy to the surrounding elements.

RESULTS

Tables 25 and 26 outline the member axial forces before and after corrosion for all members framing into the U10 and L11 connections respectively. It is clear that under the weight of the bridge, the removal of 0.1 inches of gusset plate thickness (i.e. 20% thickness reduction) on the A-A plane has no significant effect on member axial force. If there was any relative displacement between the L11 gusset plate sections above and below the A-A plane (i.e. shear yielding) a larger change in member axial force would be expected. Therefore, it can be concluded that the 20% corrosion loss was not sufficient to cause any global redistribution of member axial forces in the structure.

Figures 39-42 plot the mid-thickness shear and normal stress distributions on the A-A and B-B plane for both gusset plates in the L11West connection. These stresses are plotted for the line of full-thickness elements adjacent to the elements with reduced thicknesses. The plots for the L11East connection are similar, therefore only the L11West results are presented.

Similar to the member axial force results, there was very little change in stress on the A-A and B-B planes when the corrosion elements were removed. On section A-A, the shear stresses slightly decreased in the center of the plate and slightly increased on the two plate edges when the corrosion elements were removed. One would assume that if the gusset thickness is decreased the stresses should increase. However, prior to removal of the corrosion elements, the gusset plate had already reached the Von Mises yield criterion in the center region between the two diagonal members. The yield pattern in the L11 gusset plate before and after corrosion can be seen in Figures 43 and 44. Since this material is at its yield point, the strain energy of the corrosion elements gets redistributed to the elastic material at the edges of the plate. The normal stress distribution on the A-A plane showed no appreciable change with the corrosion elements removed.

On the B-B planes, there was a slight decrease in normal stress magnitude once the corrosion elements were removed. Again, this was due to the plastic redistribution of stress after removal of the corrosion elements. However, a small spike in the stress distribution on plane B-B was observed at the level of the corrosion elements (i.e. intersection with the A-A plane). The spike was small, and likely an artifact of the relatively coarse finite element mesh in this region. Regardless, it can be concluded that there was no significant change in the overall stress distribution in the L11 gusset plates due to corrosion.

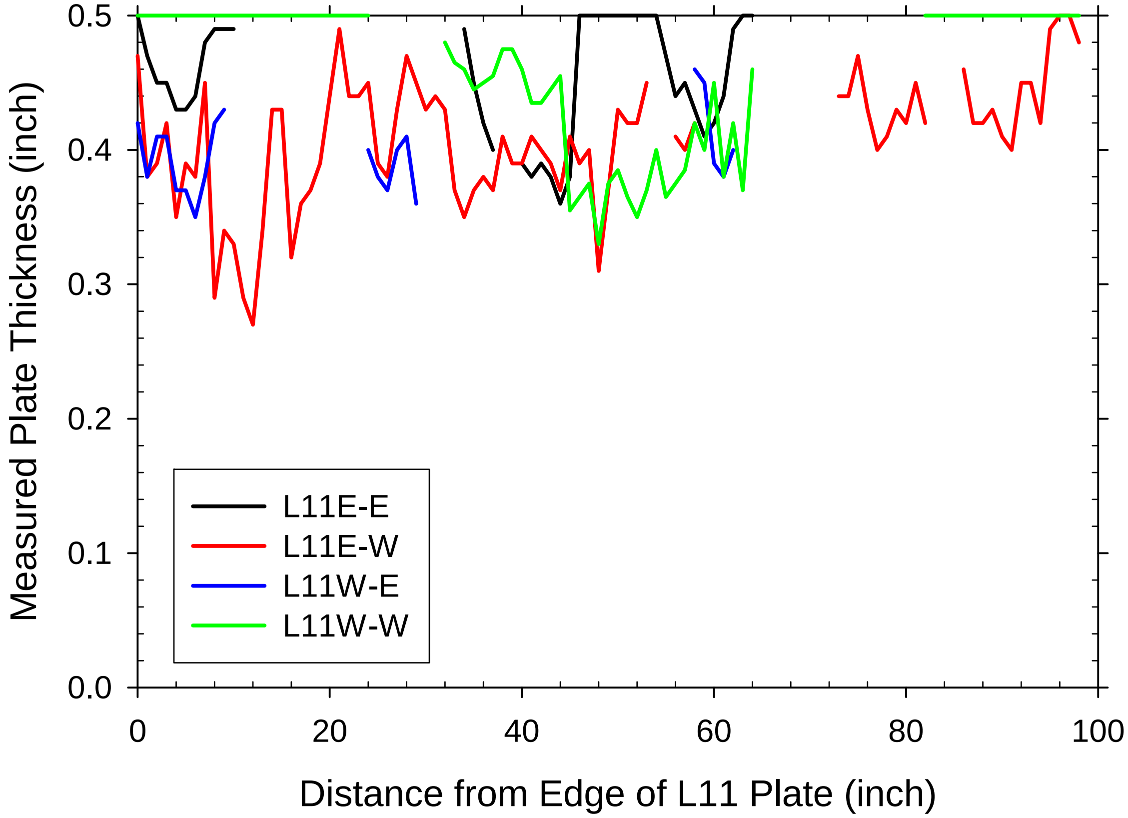

Figure 37. Thickness profile of L11 gussets.

Table 24 Average Plate Thickness in Corroded Portion of L11 Gusset Plates

Connection	L11East		L11West	
Plate	East	West	East	West
Average Thickness (inch)	0.455	0.409	0.397	0.437

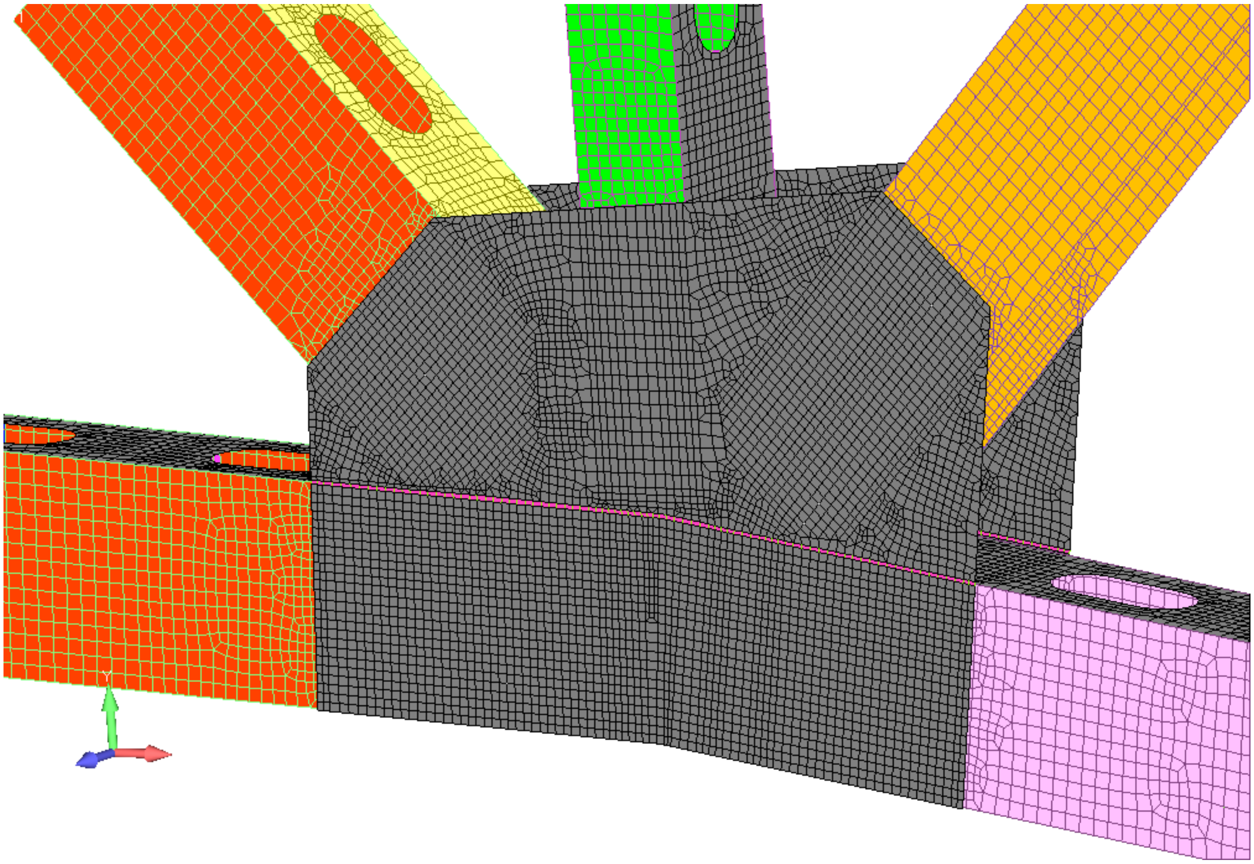

Figure 38. Preprocessor picture of L11 joint, corrosion elements shown as dark pink.

Table 25 Internal Axial Forces for U10 Members

	Axial load with increased deck thickness and new barriers (kips)	Axial load after corrosion elements removed (kips)	Differential Load [a] (kips) [% of dead load] [b]
U10U9 West	1926.1	1925.9	0.2 [0.01 %]
U10L9 West	-2163.1	-2163.3	0.2 [-0.01 %]
U10L10 West	333.1	333.4	-0.3 [-0.09 %]
U10L11 West	1796.6	1796.2	0.4 [0.02 %]
U10U11 West	-520.2	-520.2	0 [0 %]
U10U9 East	1922.7	1922.4	0.3 [0.02 %]
U10L9 East	-2160.4	-2160.6	0.2 [0.01 %]
U10L10 East	332.7	333.0	-0.3 [-0.09 %]
U10L11 East	1794.2	1793.8	0.4 [0.02 %]
U10U11 East	-521.2	-521.2	0 [0 %]

[a] – Difference was defined as axial load with increased deck thickness and new barriers and axial force after corrosion elements removed.

[b] – Percentage was defined as the difference divided by the axial load after the addition of a thicker deck and new barriers.

Table 26 Internal Axial Forces for L11 Members

	Axial load with increased deck thickness and new barriers (kips)	Axial load after corrosion elements removed (kips)	Differential Load[a] (kips) [% of dead load][b]
L11L10 West	-642.2	-642.0	-0.2 [0.03 %]
L11U10 West	1788.0	1787.6	0.4 [0.02 %]
L11U11 West	-342.2	-342.3	0.1 [-0.03 %]
L11U12 West	1650.6	1650.3	0.3 [0.02 %]
L11L12 West	-1520.1	-1519.6	-0.5 [0.03 %]
L11L10 East	-641.6	-641.3	-0.3 [0.05 %]
L11U10 East	1785.7	1785.3	0.4 [0.02 %]
L11U11 East	-341.5	-341.6	0.1 [-0.03 %]
L11U12 East	1648.4	1648.1	0.3 [0.02 %]
L11L12 East	-1518.5	-1518.0	-0.5 [0.03 %]

[a] – Difference was defined as axial load with increased deck thickness and new barriers and axial force after corrosion elements removed.
[b] – Percentage was defined as the difference divided by the axial load after the addition of a thicker deck and new barriers.

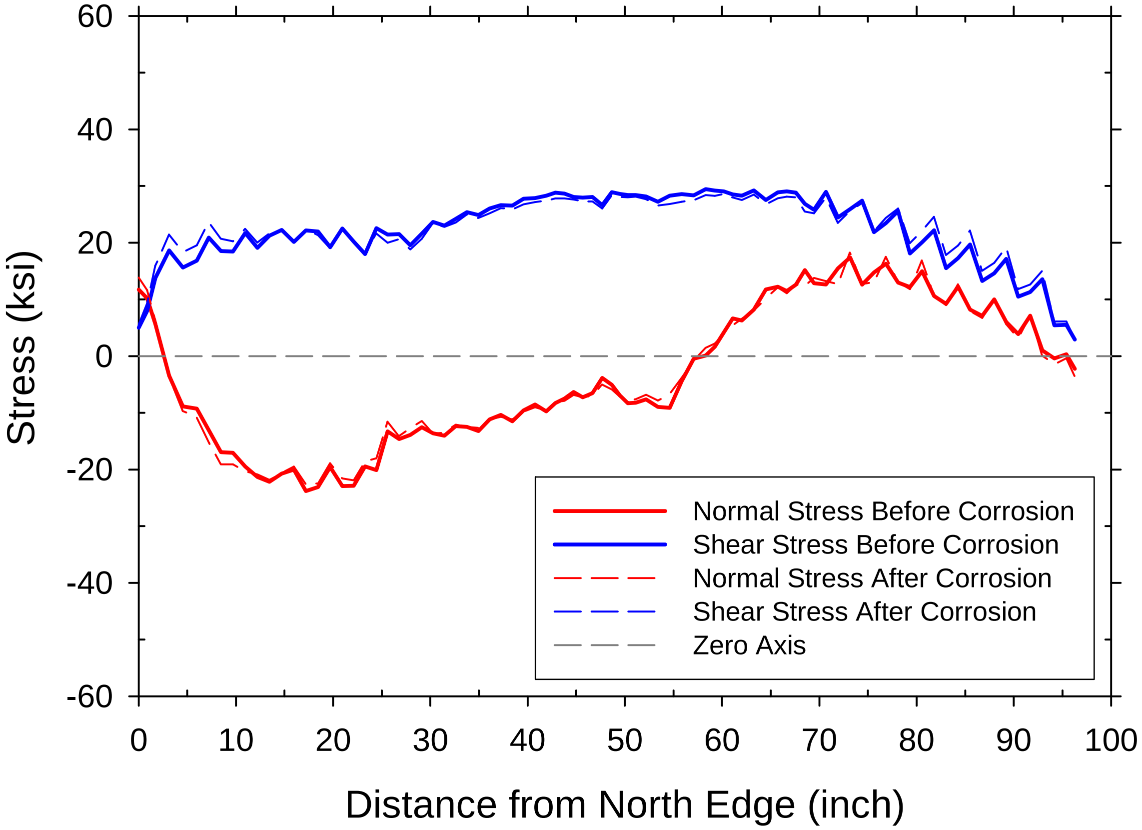

Figure 39. A-A midsurface normal and shear stress distributions for L11W-west plate.

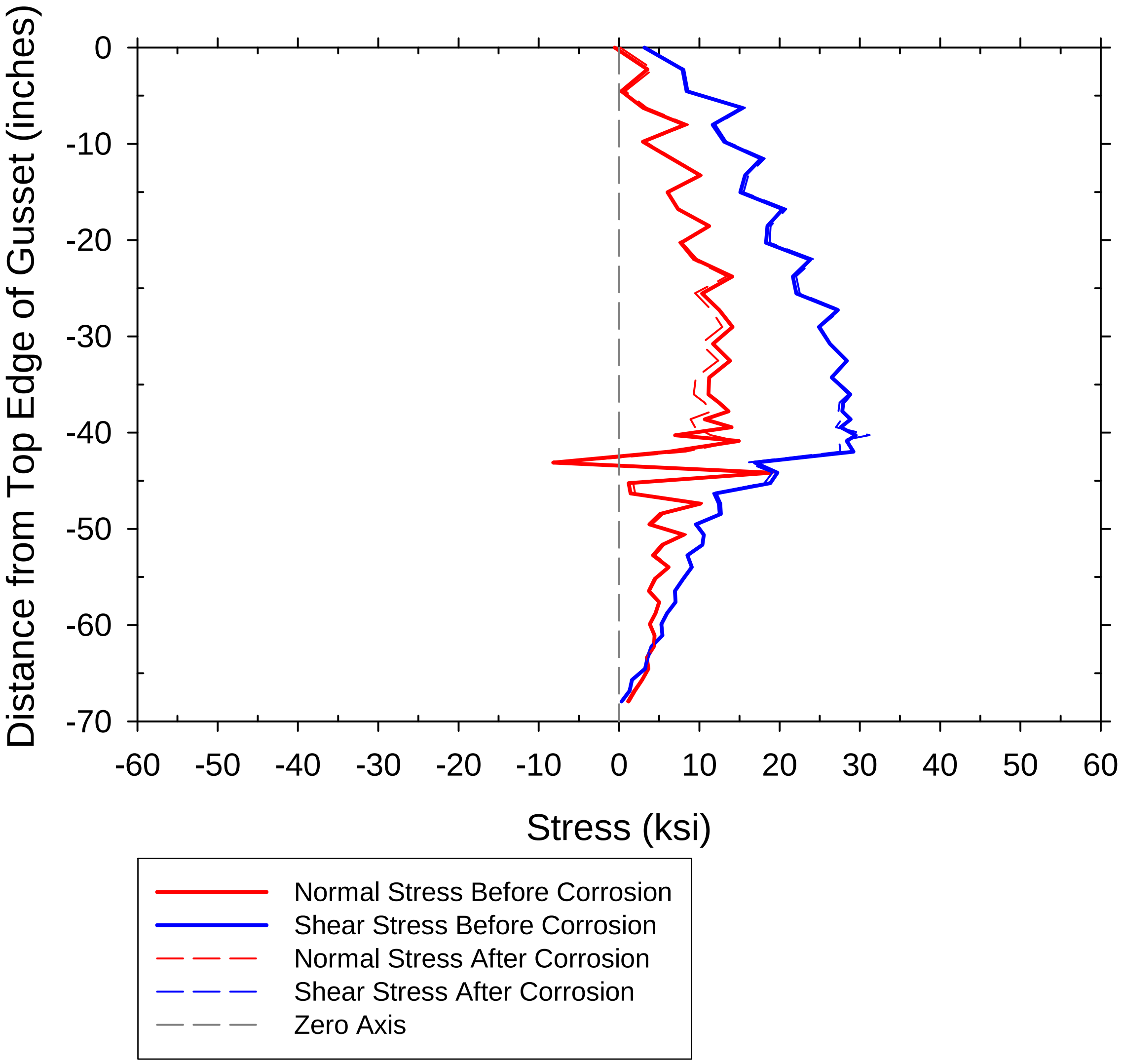

Figure 40. B-B midsurface normal and shear stress distributions for L11W-west plate.

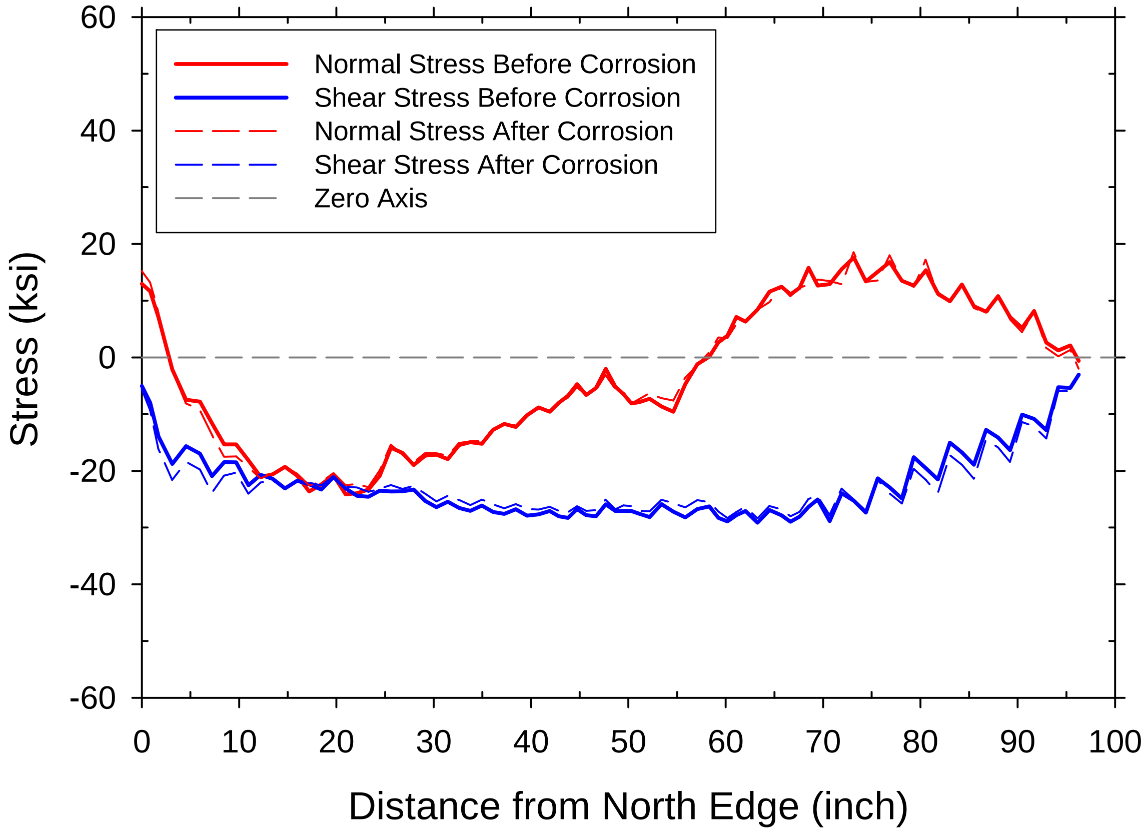

Figure 41. A-A midsurface normal and shear stress distributions for L11W-east plate.

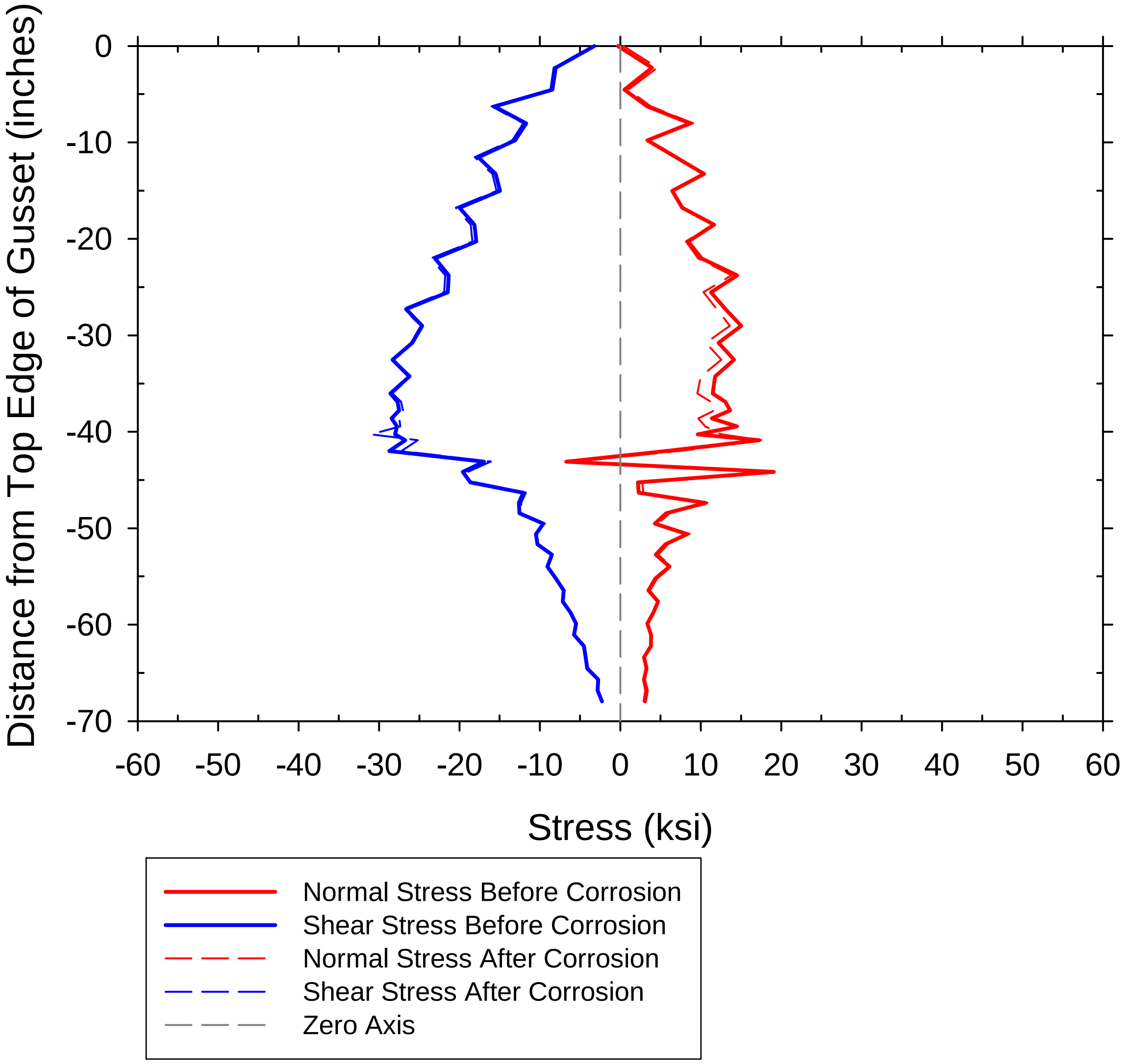

Figure 42. B-B midsurface normal and shear stress distributions for L11W-east plate.

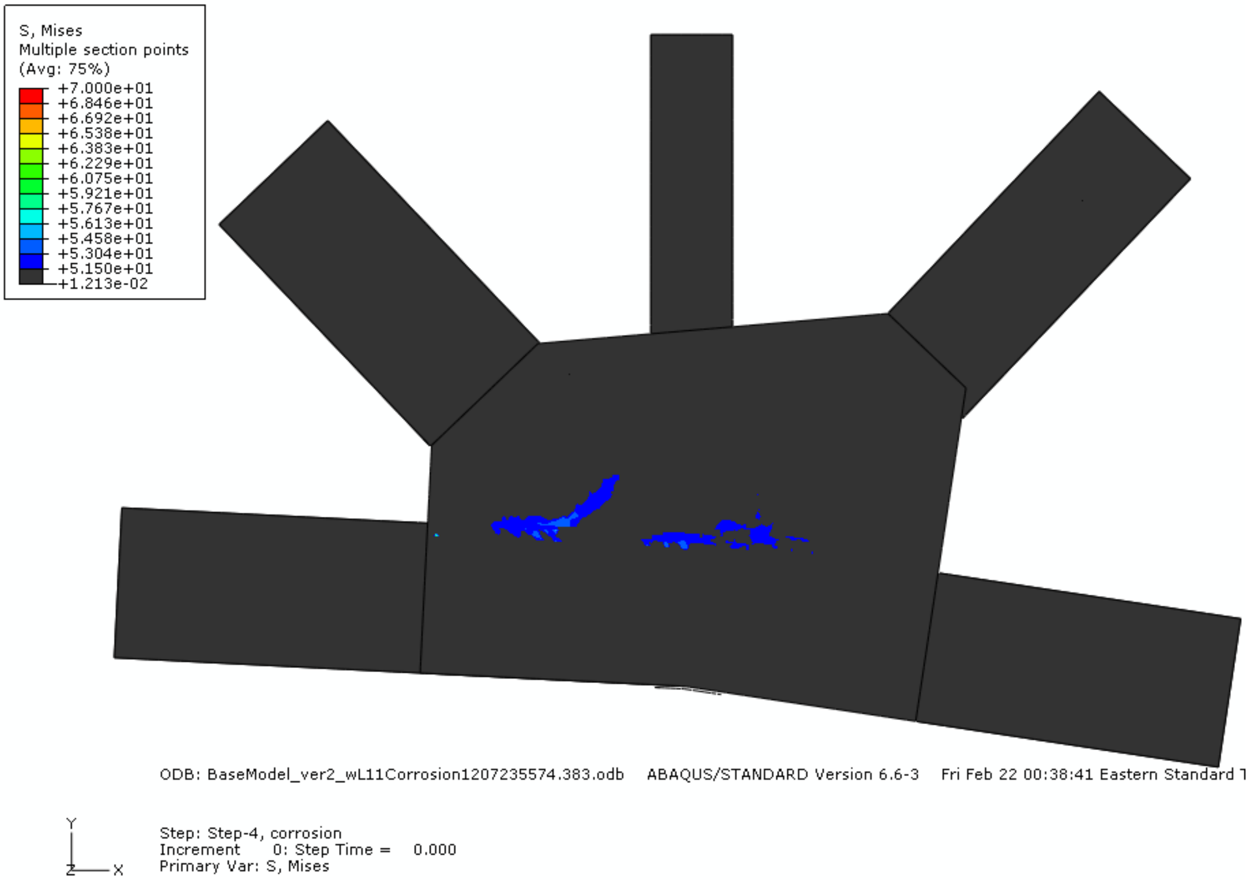

Figure 43. Yielded region (blue) of L11gusset before corrosion elements removed.

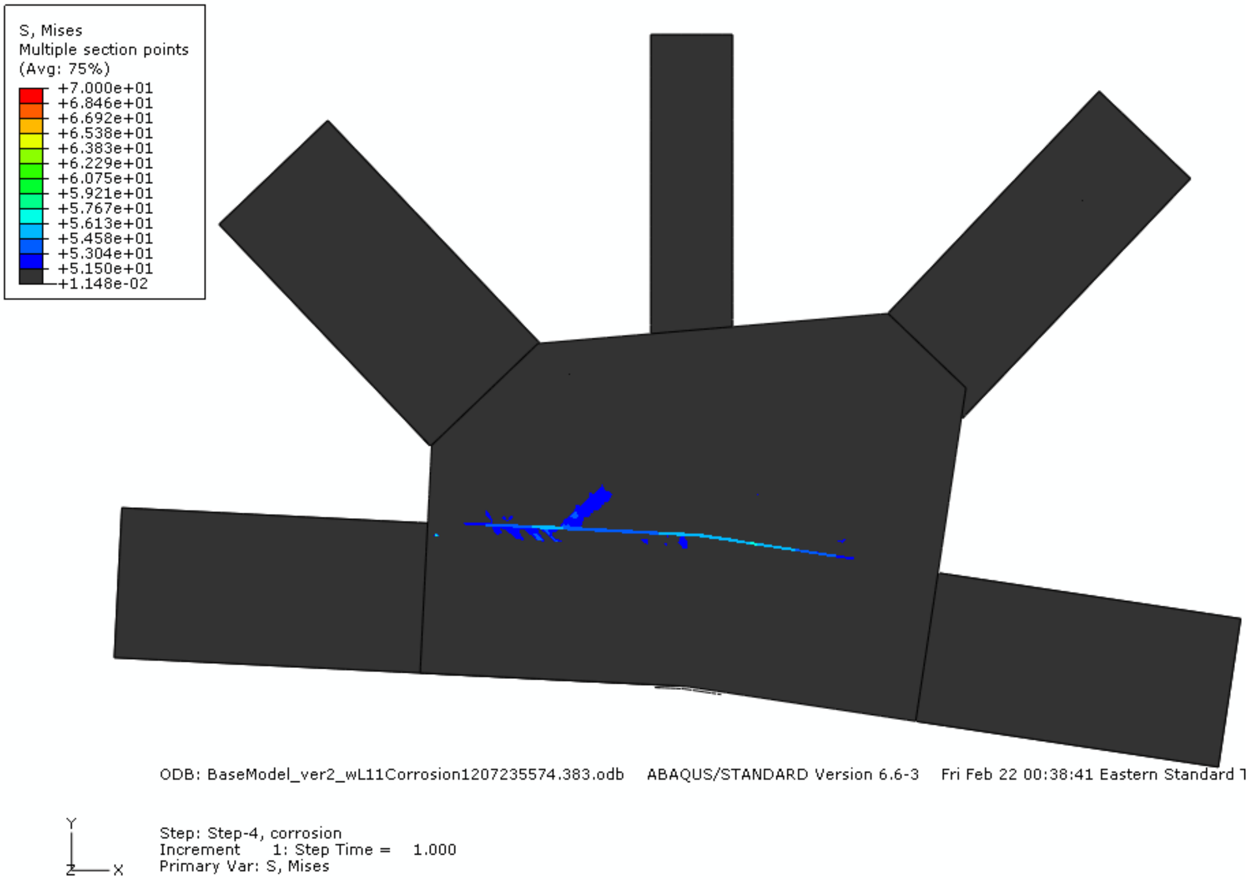

Figure 44. Yielded region (blue) of L11gusset after corrosion elements removed.

CHAPTER 5. THERMAL EFFECTS

Researchers and engineers involved in the fatigue assessments of the deck truss agreed that the roller bearings were "frozen" to some extent.[6,8] The condition of the roller bearings can greatly affect the internal member forces caused by temperature changes in the bridge. This section will describe how the detailed model was used to evaluate the influence of the thermal loads and the results of this analysis.

OBSERVATIONS OF BEARINGS

Figure 45 shows a picture of one of the bearing sole plates at the pier 5 location. A distinct wear pattern can be observed that depicts the displacement range of the three rollers within the bearing. White dashed lines have been superimposed upon the photo showing the overall range of motion presumably caused by the annual temperature extremes affecting the bridge. The second set of magenta dashed lines represents a more recent, active range of motion. Presumably this is due to a smaller daily, weekly, or monthly temperature ranges. The active range was defined as having a more polished, unrusted surface condition compared to the region bounded by the white dashed lines. These wear marks were also evaluated for the remaining sole plates on Pier 6 and 8 to isolate the bearing motions.

According to pg. 38 of the design plans[1], the roller bearings were designed with a set temperature of 45 °F. Extreme record temperatures for Minneapolis between years 1968 up to the time of collapse is -34 °F on 1 January 1970 and 105 °F on 31 July 1988.[7] Two separate runs with a negative 79 °F and positive 60 °F were applied to all elements in the computer model with a reference temperature of 45 °F. The coefficients of thermal expansion (COTE) for the steel and concrete elements of the bridge were 0.0000065/°F and 0.0000052/°F, respectively. The value of COTE for the concrete was based on measurement of cores removed from the deck.[5] The ideal range of bearing motion was determined by taking the difference in bearing displacements between these two model runs considering the main trusses were supported on ideal pin and roller boundary conditions.

Figure 46 compares the measured range of roller motion to that predicted by the computer model. The displacement range for each bearing is plotted relative to the pinned bearing at Pier 7. It should be noted that the displacement between the east and west bearings at each pier location were essentially equal (both in the model and in the field). Therefore, results will only be presented for each pier, not each individual bearing point. Looking at the actual range of motion, the motion of the Pier 6 roller is essentially the same as that predicted by the ideal roller model. However, both the Pier 5 and Pier 8 rollers exhibited greater motion than that predicted by the model. There is no readily explainable reason why the actual range of motion was larger than predicted. The process to determine motion from the rust patterns is somewhat subjective, and may explain some of this difference in addition to any thermal gradient effects.

MODELING THERMAL MOVEMENT

Abaqus has the capability to model the frictional drag force within the roller bearings, but before initiating that type of complexity, it was desirable to attempt a simpler approach. Bearing displacement data collected by the URS Corporation between June 2003 and July 2004 was used to develop a simpler approach to model the bearing movement.[8] Only the displacement of the Pier 5 rollers was measured for the entire 13 month period while the remaining rollers were only measured once, 5 months after taking the reference measurement. The data collected by URS is reproduced in Table 27.

The temperature corresponding to the URS displacement measurements were analyzed in the computer model assuming two different boundary conditions. The first boundary condition assumed ideal rollers at Piers 5, 6, and 8. The second boundary condition assumed the bearings were gone and that the bridge piers were pin-connected to the main trusses. The second boundary condition assumed the bearings were locked and forces due to thermal effects would cause bending of the piers. The model did predict slight differences between the east and west sides of each pier with some hysteresis through the 13 month temperature cycle. This is probably caused because of the path dependency of the solution considering nonlinear geometry and material affects in the model. The predicted data for the two boundary conditions are shown as thick red and gray regression lines in Figures 47 through 49. The regression lines are least-square fits through the data for both the east and west bearings.

Figures 47 through 49 also plot the physical measurements made by URS. Figure 47 shows that for the Pier 5 location, the URS measurements are poorly correlated to the ideal roller condition but highly correlated to the locked bearing case. This same trend is evidenced at the Pier 6 location (see Figure 48), although there is only one data point to compare. A similar plot made for Pier 8 shows poor correlation to both modeled cases in Figure 49. The predictions for Pier 8 appear to be counterintuitive since the locked bearing case predicts larger displacements than ideal bearings. However, in the case of locked bearings, the piers allow for a finite deflection of the pinned bearing at Pier 7 that is not allowed when analyzed with ideal boundary conditions.

The URS measurements of the Pier 5 rollers obviously show that the rollers do have real motion over the 65 degree change in the 13 month monitoring period. However, when all the bearings are locked from translation at the piers, the horizontal displacement of the pier tops predicted by the model is essentially the same as the measured displacement of the bearings. This suggests that pinning the bearings to the piers is an acceptable means to simulate actual bridge response. Lacking any knowledge of the actual resistance of the bearings to motion in their corroded condition, further refinement of bearings in the model is not warranted. Therefore, the pinned bearing assumption was used to simplify modeling of the structure under thermal loads.

EVALUATION OF THERMAL LOADS

The thermal load effects on member forces and stress in the bridge at the time of collapse cannot be definitely determined unless the zero-force reference temperature is known. That is, the bearings move under thermal cycles, but it cannot be determined at what point in the bearing's linear motion they may have locked into position (either with the bridge in an expanded or contracted state) nor at what time this may have occurred. Therefore, the best that can be done to determine the effect of thermal loads is to bound the results. To do this, one needs to determine the temperature extremes over a time range and consider that the bearings may have become locked at these extremes.

Displayed in Table 28 are the minimum and maximum temperatures for the 24 hour, weekly, and monthly time periods leading up to the collapse. It was assumed that the active range of motion evidenced on the bearing sole plates occurred from at least monthly movements. Assuming that the bearings moved at least on a monthly basis, the temperature extremes were 59 °F and 102 °F. These July 2007 minimum and maximum temperatures are shown in a thermal scale in Figure 50. This thermal history shows that two runs are required to bound the problem in the model. The first run will warm the bridge from the design set temperature of 45 °F to the July low of 59 °F after step 3, then lock the bearings, apply the construction and traffic loads, and finally warm the bridge up to 92.1 °F which was the ambient at collapse. The second run is slightly different by warming the bridge to 102 °F after step 3, lock the bearings, then apply the construction and traffic loads, and finally cool the ambient down to 92.1 °F for the collapse condition. Both of these scenarios apply only uniform temperatures to the entire bridge neglecting any affects from shading and radiation.

NTSB also provided estimates of differential heating and cooling of the main trusses for an additional analysis run.[10] Using temperature data collected from a study following the 1996 partial collapse of the LAK-90-2342 R deck truss bridge over the Grand River in Ohio, NTSB estimated the true temperature (accounting for radiation and shading) in the two main trusses as time progressed through the day of the collapse. These temperatures are shown in Figure 51. The same analysis philosophy was used as in the previously described analysis of uniform temperature change in terms of when the temperatures were applied, boundary conditions, etc. The only difference was the magnitude of the temperature change and to which nodes they were applied to. In this case, three groups of nodes were assembled. The first group accounted for all nodes in the west truss verticals, diagonals, and lower chords. The second group was for the east truss verticals, diagonals, and lower chords. The final group was for all the remaining nodes in the model including the upper chords of the main trusses and gusset plates from the U10 connections. The idea of neglecting the upper chords from the two main truss groups is they would have been shaded at the time of collapse and would be better represented by the ambient temperature

In the non-uniform heating scenarios, the east and west truss groups were assigned an appropriate temperature change to represent their individual temperatures at collapse as defined by the values of the blue and red lines in Figure 51 at the time of the collapse (6:00 pm or 18:00). The remaining nodes in the model were assigned an appropriate temperature to represent the ambient at collapse

RESULTS OF THERMAL LOADING

Uniform Heating

Table 29 shows the change in member axial force around the U10 connection when uniform thermal changes are induced with the construction/traffic loads in place. Shaded cells indicate the members where the magnitude of the axial force (tension or compression) increased as the bridge was either warmed or cooled. In general, a larger force change was observed in the top chord compared to the vertical and diagonal members. The magnitude of the force change is largest in the scenario where the bearings lock at 59 °F, where the force in member U10U11 increased by about 22 percent. For the case where the bearings lock at 102 °F the largest force increase was only 3.2% occurring in member U10U9.

To further display thermal loading results, stress distribution plots were plotted on the two critical planes (section A-A and B-B) for two the U10W gusset plates. Figures 52 through 55 show the midplane normal and shear stress distributions along sections A-A and B-B for the both the east and west gusset plates in the U10W connection, for the cases where the bearings were assumed to locked at 59 °F and 102 °F. The plots for the U10E connection show identical trends and will not be presented. In all four plots, the differences in the stress plots are unperceivable when the bearings were locked at 102 °F. However, in the cases where the bearings were locked at 59 °F, slight decreases where observed in all the shear stress distributions and in the normal stress distributions of the B-B planes as the bridge was warmed to the collapse temperature.

Non-Uniform Heating

Table 30 shows the change in member axial force around the U10 connection when non-uniform thermal changes are induced with the construction/traffic loads in place. Shaded cells indicate the members where the magnitude of the axial force (tension or compression) increased as the bridge temperature heated or cooled non-uniformly. The trends and magnitudes of forces changed very little between the uniform and non-uniform temperature scenarios.

To further demonstrate this point, stress distribution plots were made for the two critical planes (section A-A and B-B) of just the U10W-West plate. These are illustrated in Figures 56 and 57 for the A-A and B-B planes respectively. These two plots have unperceivable differences to those in Figures 52 and 53 for the uniform temperature scenarios indicating that the various sub-systems (floor trusses, stringers, deck, main trusses, etc.) are sufficiently decoupled from each other that non-uniform heating does not affect the proportioning of the axial loads in the U10 connections, nor the stresses within the U10 gussets

Summary

The temperature-induced member forces were primarily low compared to the forces from dead load though some of the top chord members had thermal increases up to 20% of their dead lead. However, the stress change in the gusset plates depends on when the bearings locked. There was no stress change when the bearings froze at 102 °F but the stress decreased when the bearings locked at 59 °F. Therefore, the thermal load effects are not considered be a significant factor on the day of the bridge collapse.

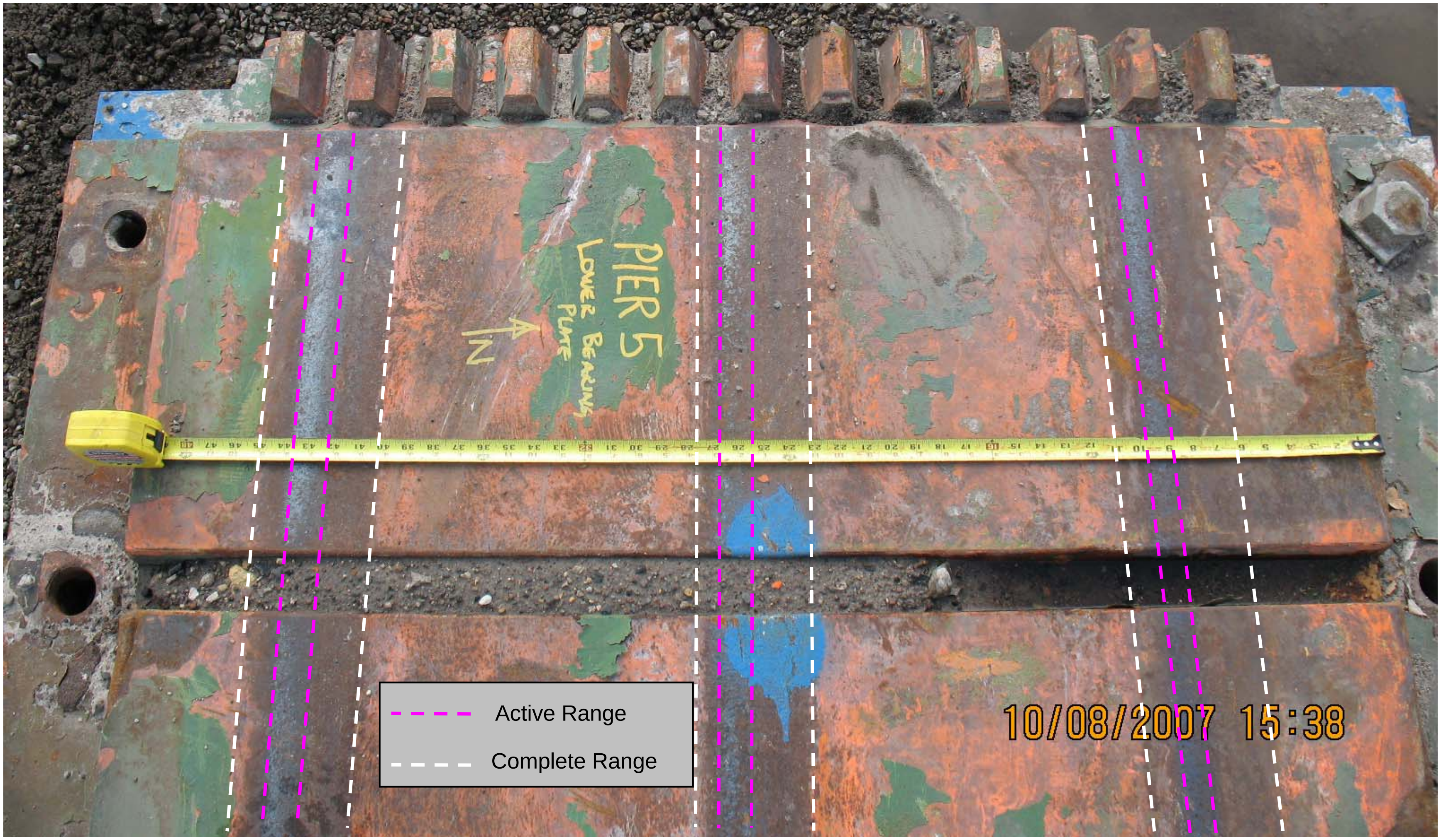

Figure 45. Roller wear indications in the lower bearing sole plate at Pier 5.

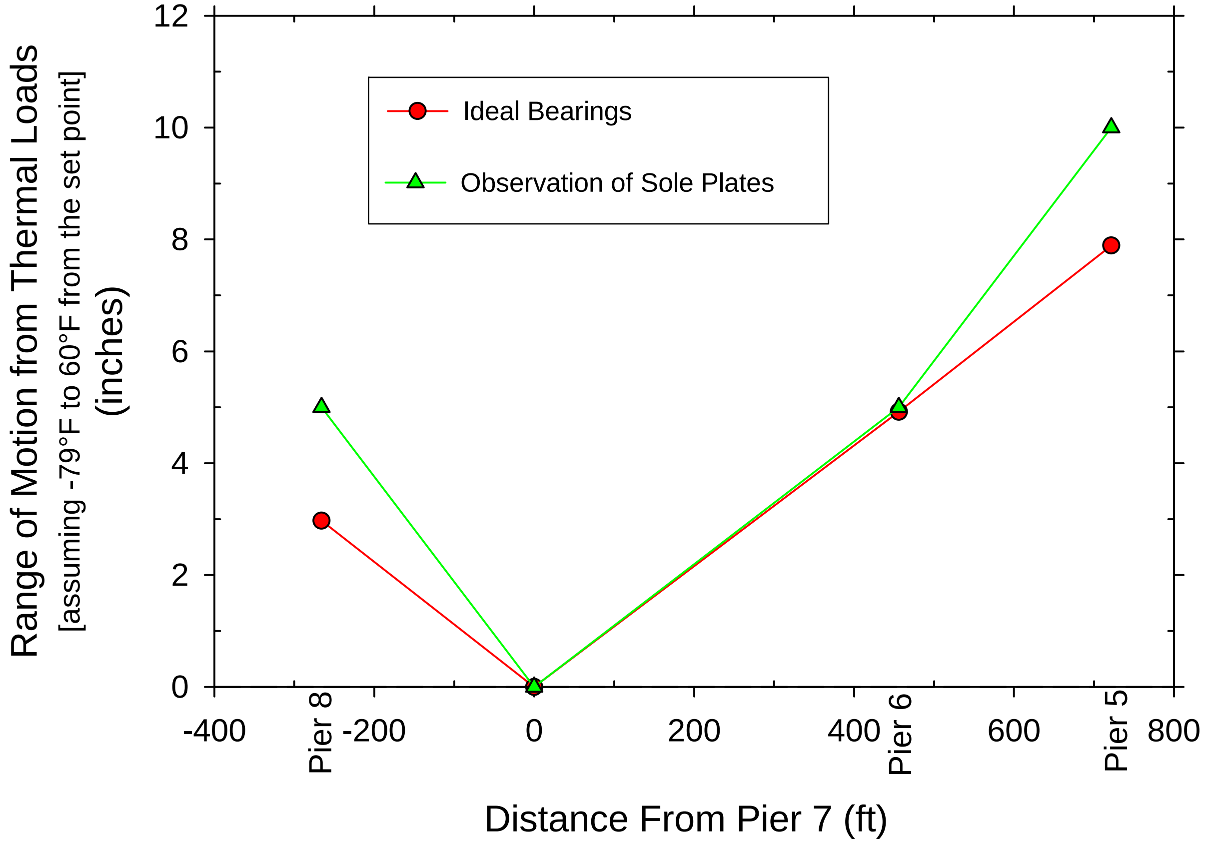

Figure 46. Range of bearing movement due to the annual MN seasonal temperature variation.

Table 27 URS Bearing Movement Measurements Reproduces from Ref. 8

	June 2003	November 2003		January 2004		March 2004		July 2004	
	Ref. Temp (°F)	Displ. (inch)	Temp. (°F)	Displ. (inch)	Temp. (°F)	Displ. (inch)	Temp. (°F)	Displ. (inch)	Temp. (°F)
Pier 5 East	66	-0.563	45	-1.438	1	-0.375	28	0.125	71
Pier 6 East	67	-0.094	45	-	-	-	-	-	-
Pier 8 East	68	-0.094	50	-	-	-	-	-	-
Pier 5 West	68	-0.500	54	-1.375	1	-0.375	28	0.500	71
Pier 6 West	68	0.000	54	-	-	-	-	-	-
Pier 8 West	63	0.000	52	-	-	-	-	-	-
NOTE: Negative displacements are towards the fixed bearing at Pier 7.									

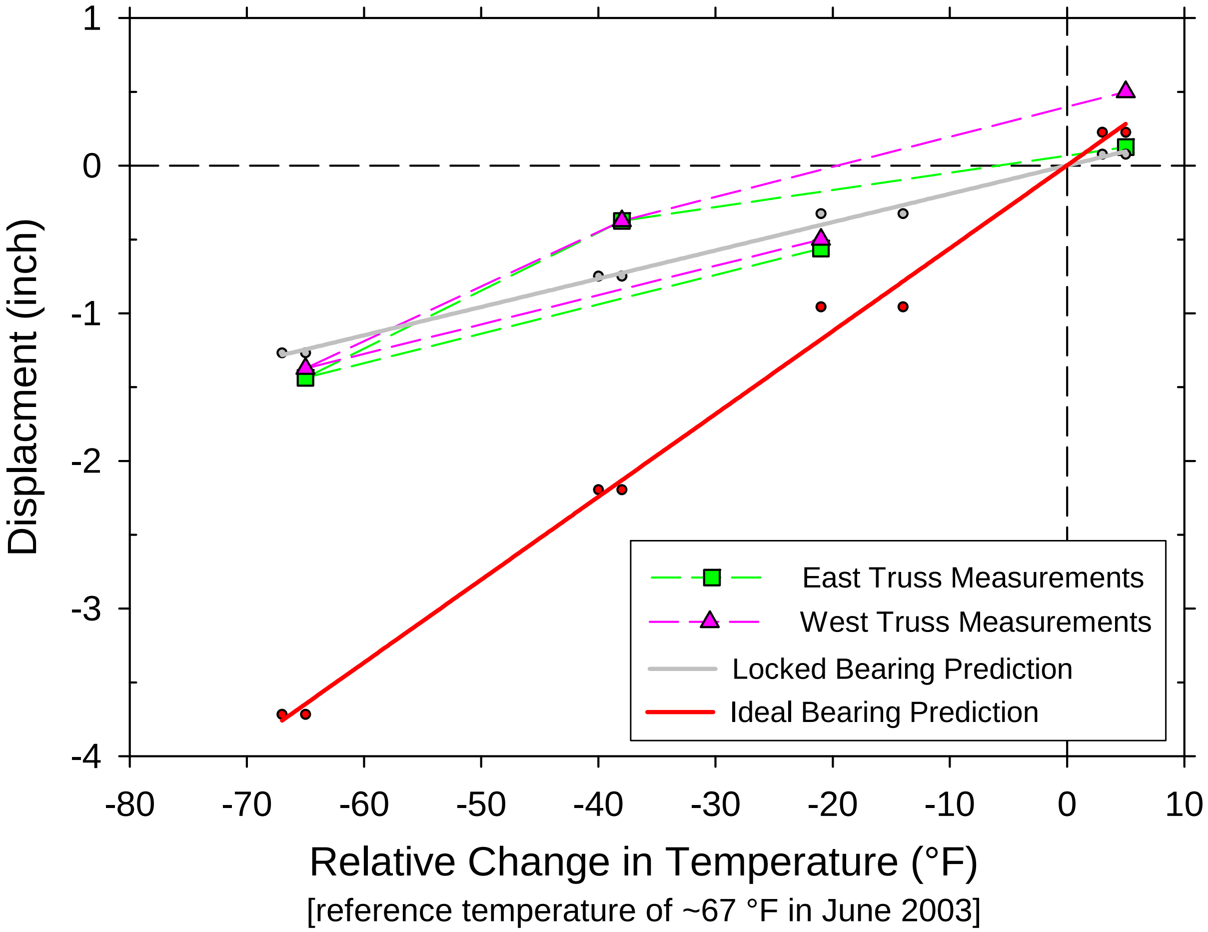

Figure 47. Comparison of URS measurements to model predictions for Pier 5

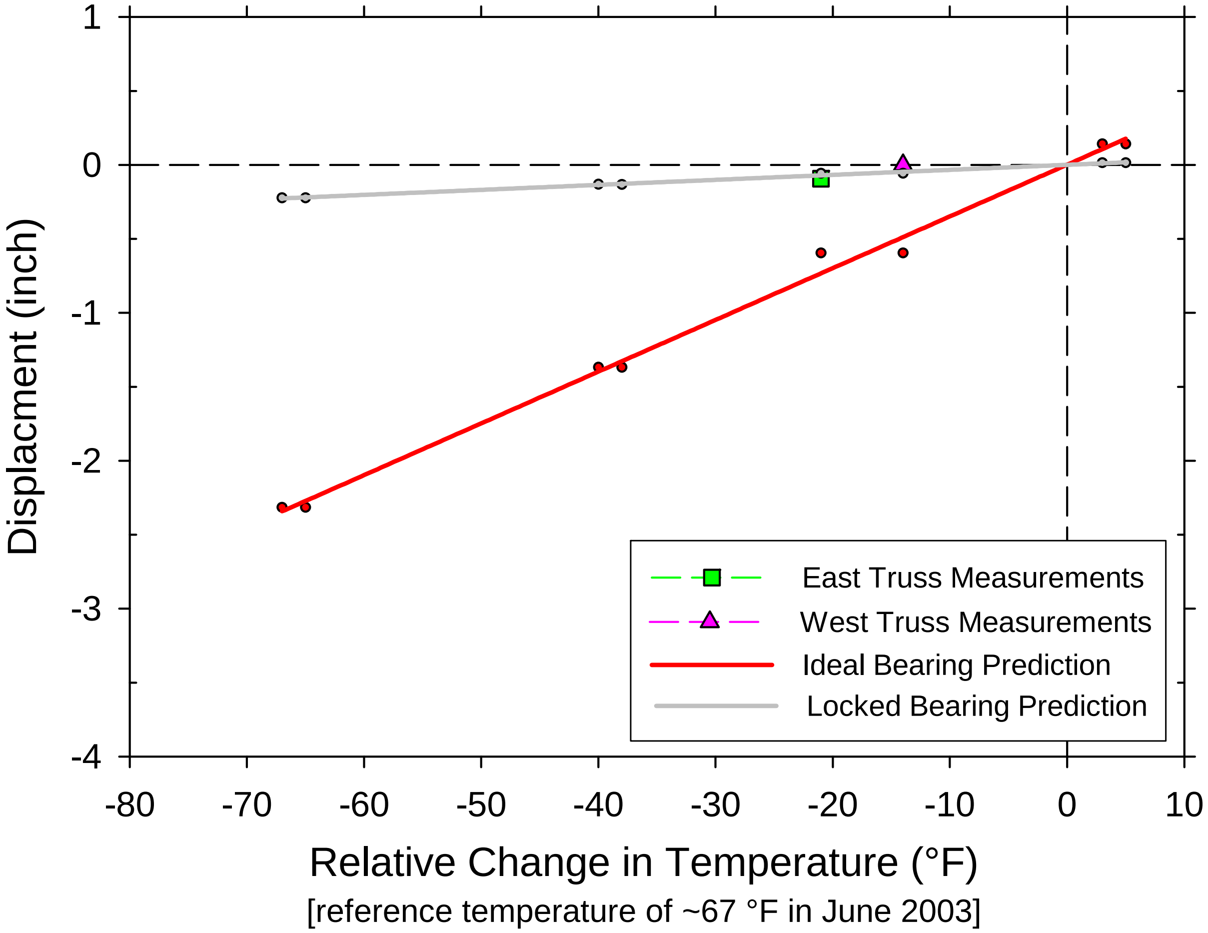

Figure 48. Comparison of URS measurements to model predictions for Pier 6.

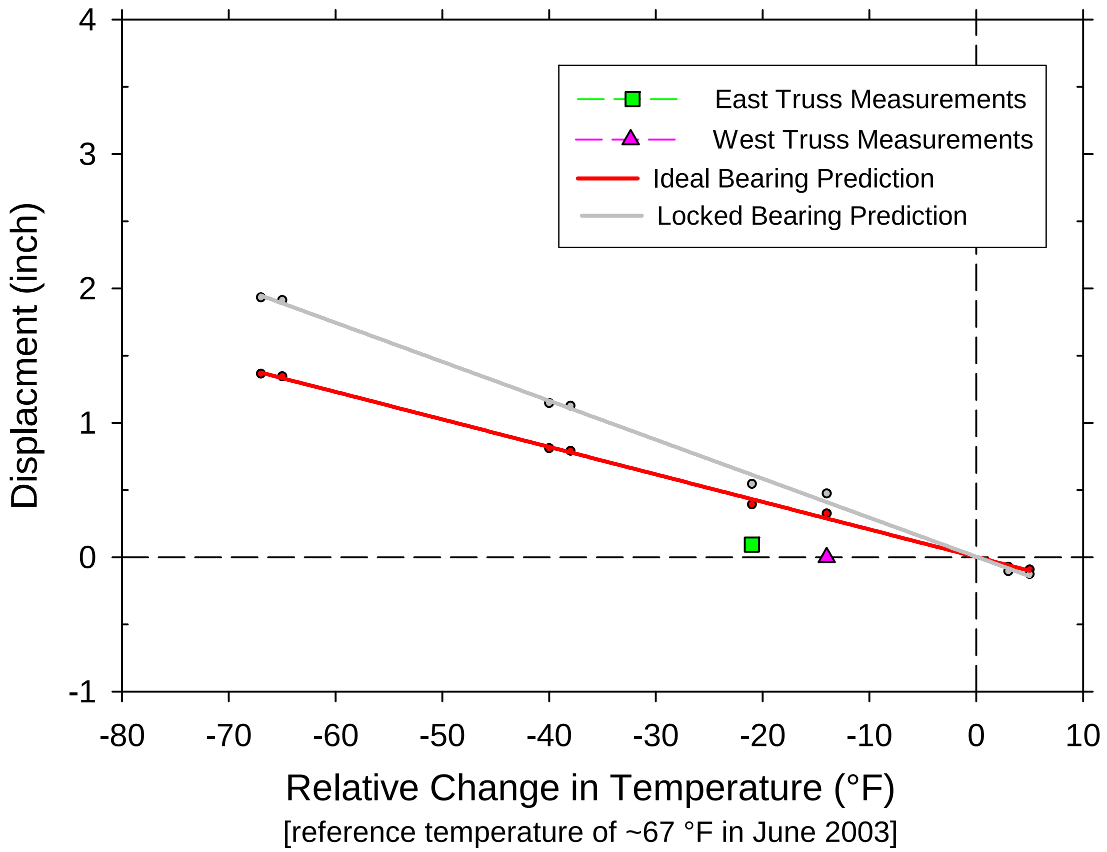

Figure 49. Comparison of URS measurements to model predictions for Pier 8.

Table 28 Temperature Ranges For the Day, Week, and Month Prior to Collapse

	Max. Temp (°F)	Min. Temp (°F)	Temperature Range (°F)
Day of Collapse	**92.9** (1 Aug 07, 4:30pm)	**73.5** (1 Aug 07, 5:00 am)	**19.4**
Week Leading up to Collapse	**97** (25 July 07)	**70** (28 July 07)	**27**
Month Leading up to Collapse	**102** (7 July 07)	**59** (11 July 07)	**43**

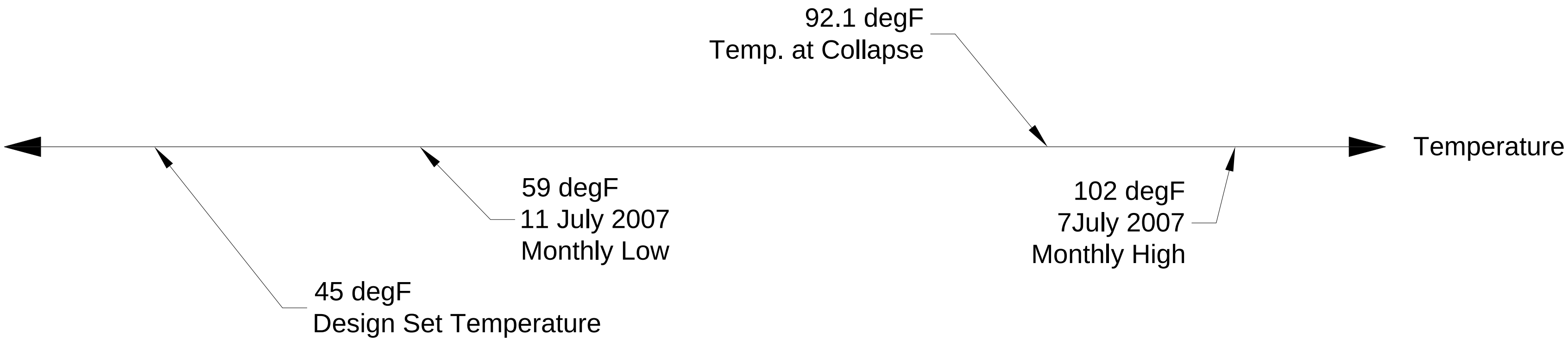

Figure 50. Thermal history of I-35W bridge in July 2007.

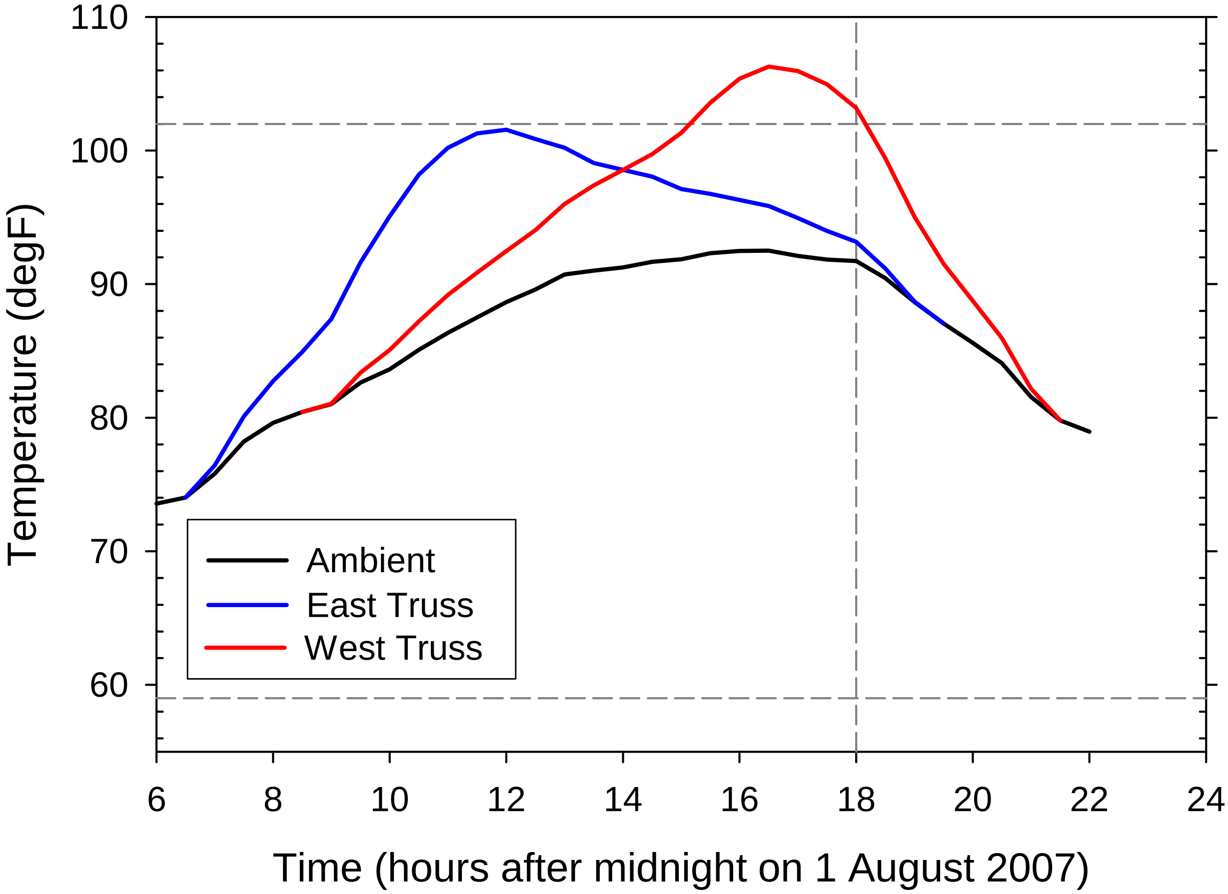

Figure 51. Temperature history of main trusses on day of collapse.

Table 29 U10 Connection Axial Force Comparisons Between Uniform Thermal Load Scenarios

Member	Assuming the bearings locked at 59 °F			Assuming the bearings locked at 102 °F		
	Axial force with const/traffic loads in place (kips)	Axial force after warming to 92.1 °F on locked bearings (kips)	Differential Load [a] (kips) [% change]	Axial force with const/traffic loads in place (kips)	Axial force after bridge cooled to 92.1 °F on locked bearings (kips)	Differential Load [a] (kips) [% change]
U10U9 West	1987.2	1774.0	-213.2 [-10.7 %]	1980.4	2043.4	63.0 [3.2 %]
U10L9 West	-2388.8	-2340.0	-48.8 [-2.0 %]	-2389.4	-2403.1	13.7 [0.6 %]
U10L10 West	399.1	405.2	6.1 [1.5 %]	400.0	397.8	-2.2 [-0.6 %]
U10L11 West	1933.2	1868.5	-64.7 [-3.3 %]	1933.5	1952.0	18.5 [1.0 %]
U10U11 West	-652.0	-792.4	140.3 [21.5 %]	-665.5	-623.3	-42.2 [-6.3 %]
U10U9 East	1950.3	1738.3	-211.9 [-10.9 %]	1943.0	2006.1	63.1 [3.2 %]
U10L9 East	-2291.4	-2243.5	-47.9 [-2.1 %]	-2297.9	-2306.4	8.5 [0.4 %]
U10L10 East	373.8	380.0	6.2 [1.7 %]	374.6	372.7	-1.9 [-0.5 %]
U10L11 East	1871.0	1806.8	-64.1 [-3.4 %]	1871.1	1890.2	19.1 [1.0 %]
U10U11 East	-609.2	-749.0	139.7 [22.9 %]	-623.1	-581.4	-41.7 [-6.7 %]

[a] – difference between the axial force with the construction/traffic loads in place and warming/cooling to 92.1 °F.

NOTE: Grey shading indicates an axial force increase

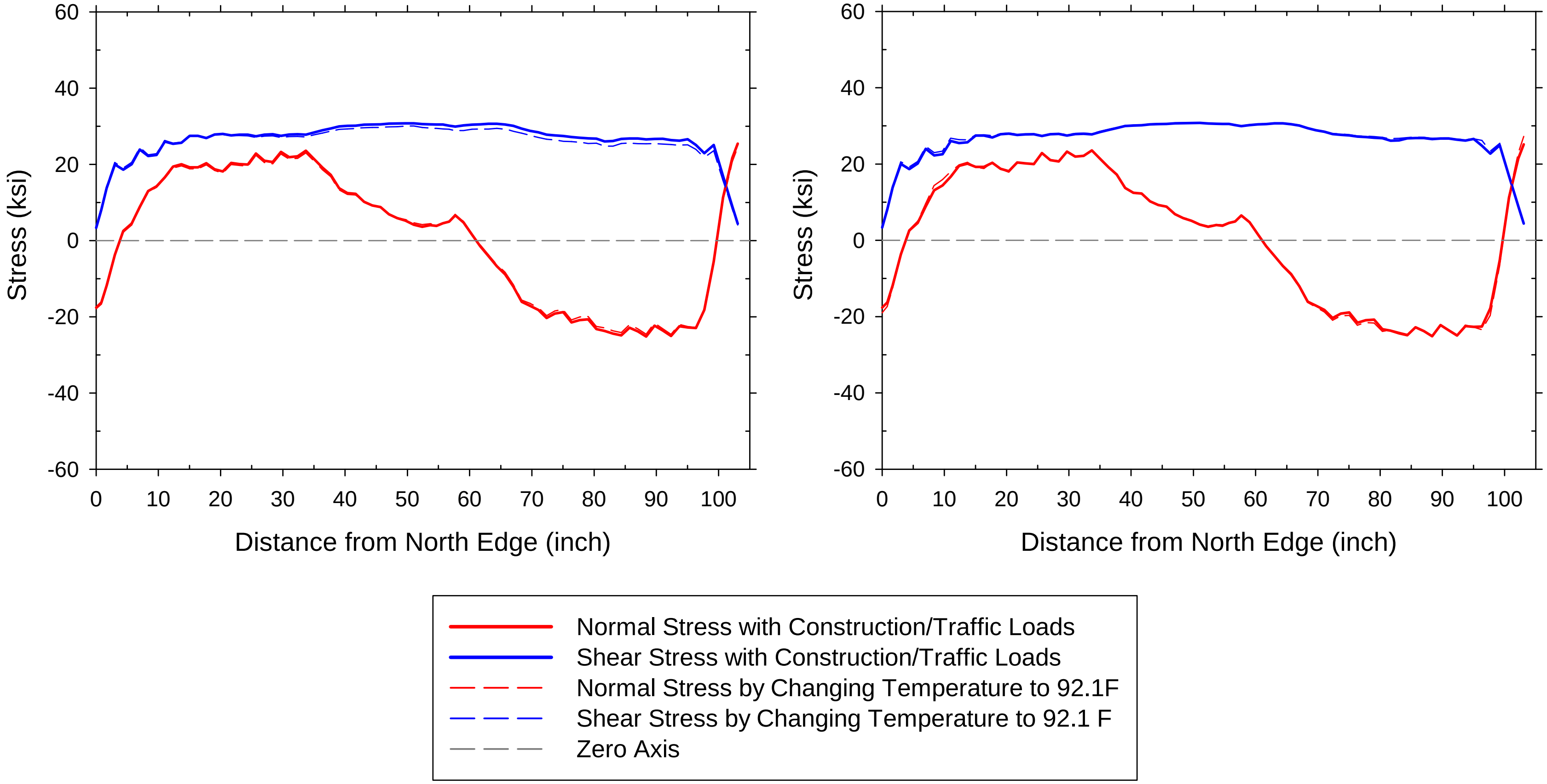

Figure 52. U10W-West plate section A-A stress distributions under uniform temperature change. Bearings locked at 59 °F (left). Bearings locked at 102 °F (right).

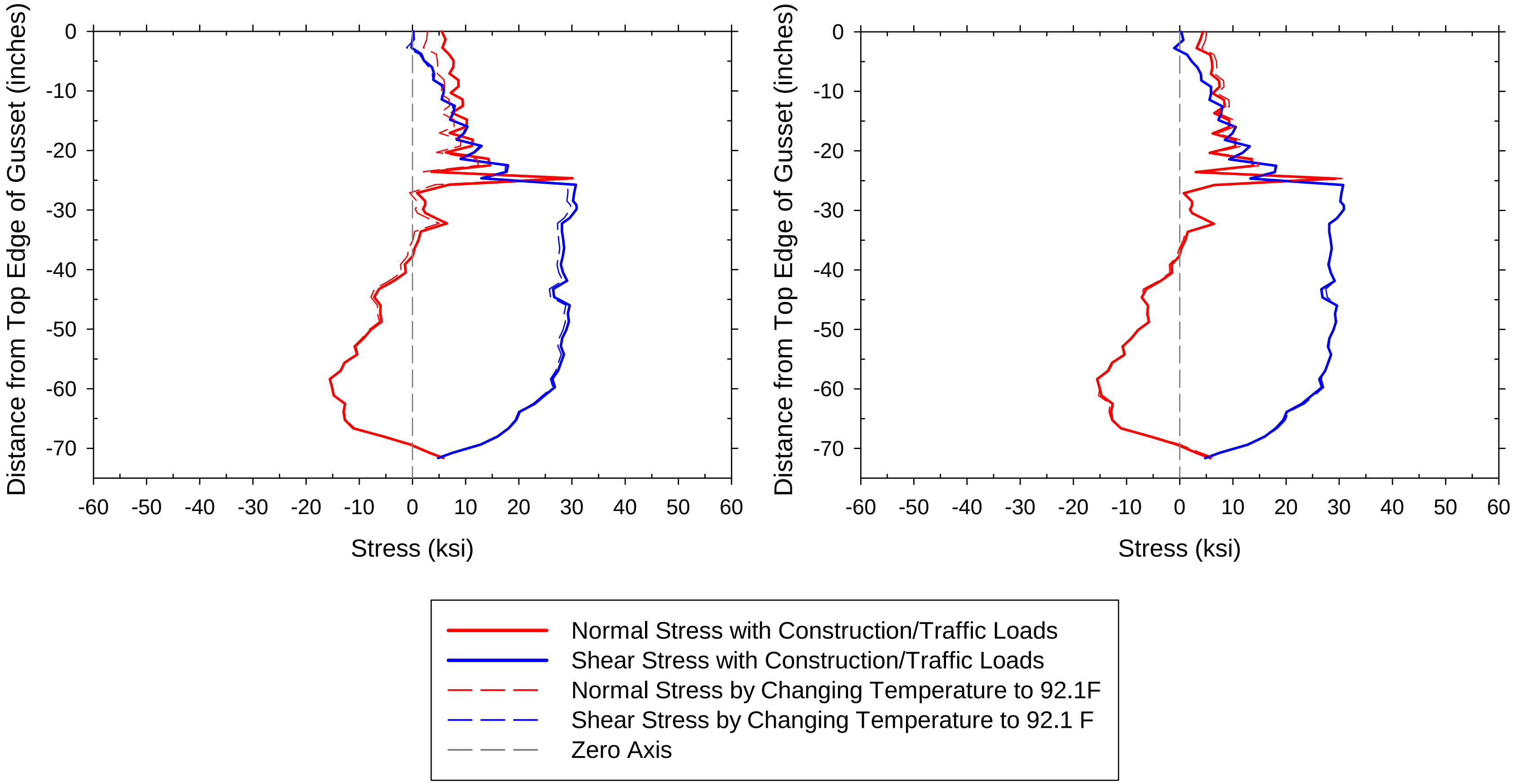

Figure 53. U10W-West plate section B-B stress distributions under uniform temperature change. Bearings locked at 59 °F (left). Bearings locked at 102 °F (right).

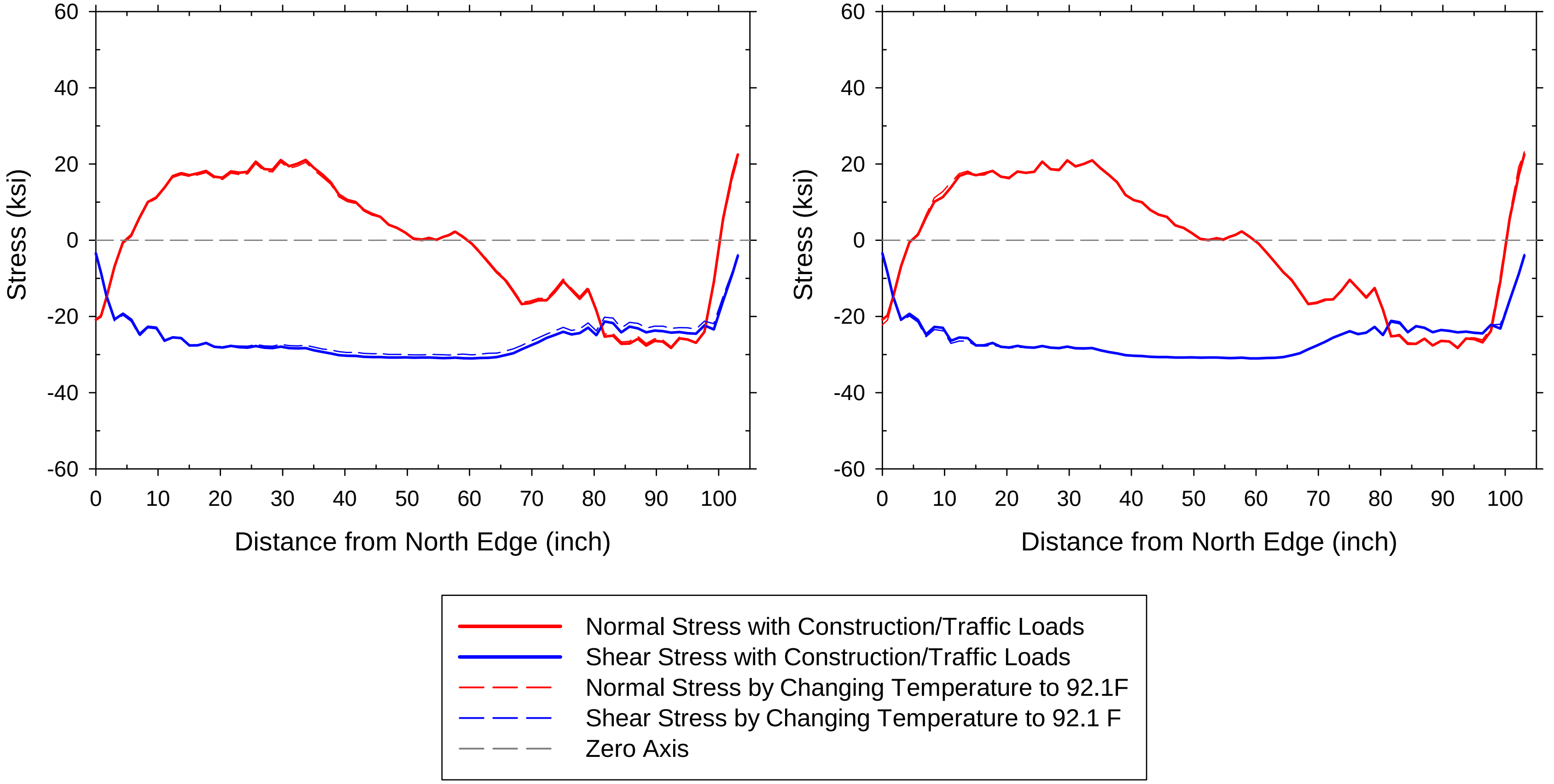

Figure 54. U10W-East plate section A-A stress distributions under uniform temperature change. Bearings locked at 59 °F (left). Bearings locked at 102 °F (right).

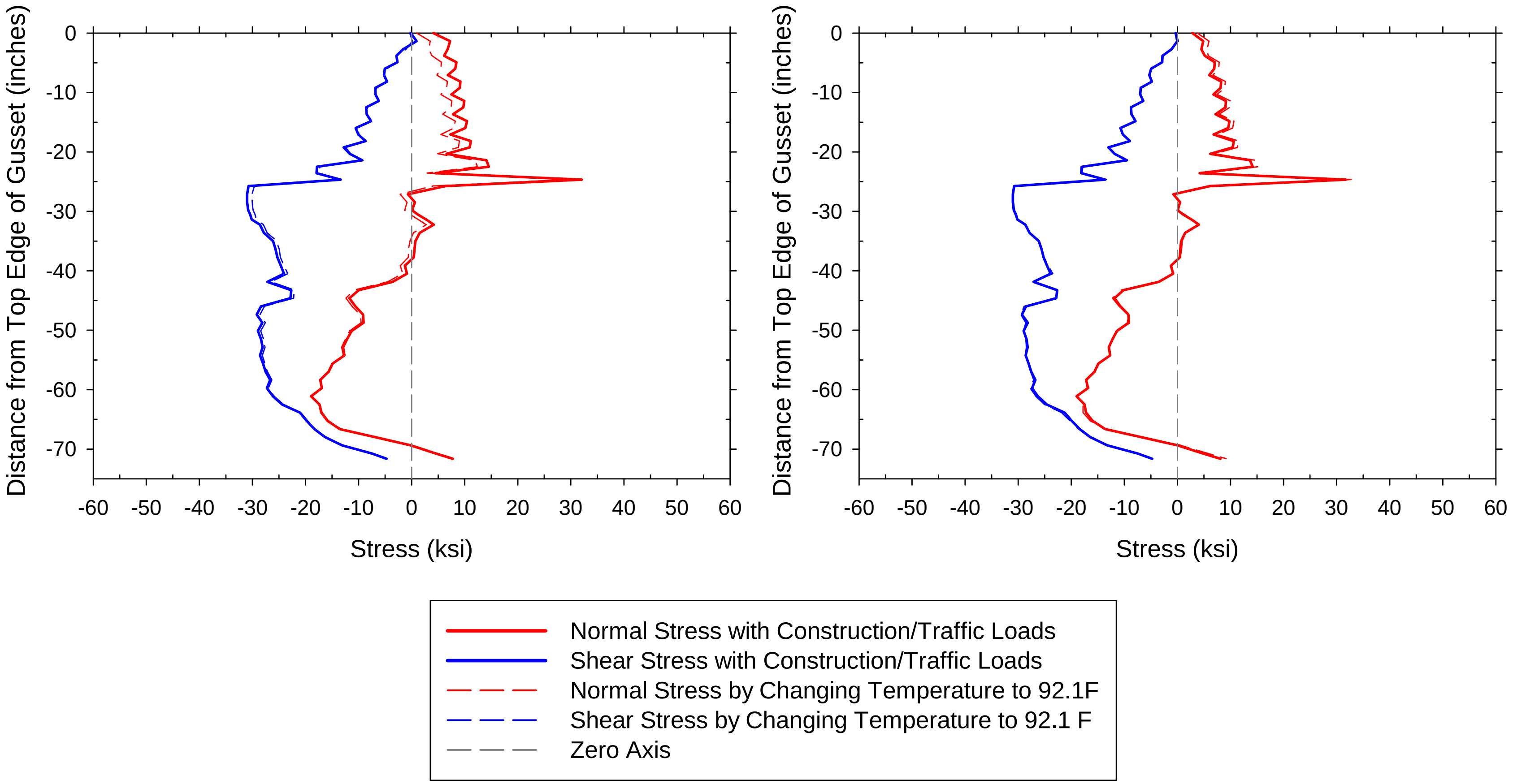

Figure 55. U10W-East plate section B-B stress distributions under uniform temperature change. Bearings locked at 59 °F (left). Bearings locked at 102 °F (right).

Table 30 U10 Connection Axial Force Comparisons Between Non-Uniform Thermal Load Scenarios

Member	Assuming the bearings locked at 59 °F			Assuming the bearings locked at 102 °F		
	Axial force with const/traffic loads in place (kips)	Axial force after warming [a] (kips)	Differential Load [b] (kips) [% change]	Axial force with const/traffic loads in place (kips)	Axial force after cooling [c] (kips)	Differential Load [b] (kips) [% change]
U10U9 West	1989.4	1762.0	-227.4 [-11.4%]	1989.4	2039.3	49.9 [2.5%]
U10L9 West	-2388.6	-2323.3	-65.3 [-2.7%]	-2388.6	-2386.8	-1.8 [-0.1%]
U10L10 West	398.8	409.3	10.5 [2.6%]	398.8	401.5	2.7 [0.7%]
U10L11 West	1933.1	1835.9	-97.2 [-5.0%]	1933.1	1920.2	-12.9 [-0.7%]
U10U11 West	-647.6	-779.4	131.8 [20.4%]	-647.6	-596.8	-50.8 [-7.8%]
U10U9 East	1952.7	1755.6	-197.1 [-10.1%]	1952.7	2030.7	78.0 [4.0%]
U10L9 East	-2291.3	-2235.5	-55.8 [-2.4%]	-2291.3	-2297.4	6.1 [0.3%]
U10L10 East	373.6	376.3	2.7 [0.7%]	373.6	368.1	-5.5 [-1.4%]
U10L11 East	1870.9	1802.6	-68.3 [-3.7%]	1868.0	1885.4	17.4 [0.9%]
U10U11 East	-604.6	-724.3	119.7 [19.8%]	-604.6	-542.5	-62.1 [-10.3%]

[a] – Warming was unsymmetric. West main truss lower chords, vertical and diagonals increased 44.18 °F. East main truss lower chords, vertical and diagonals increased 34.17 °F. All other nodes increased 32.74 °F. This assumes a reference temperature of 59 °F.

[b] - Difference between the axial force with the construction/traffic loads in place and warming or cooling.

[c] – Cooling was unsymmetric. West main truss lower chords, vertical and diagonals increased 1.18 °F. East main truss lower chords, vertical and diagonals decreased 8.83 °F. All other nodes decreased 10.26 °F. This assumes a reference temperature of 102 °F.

NOTE: Grey shading indicates an axial force increase

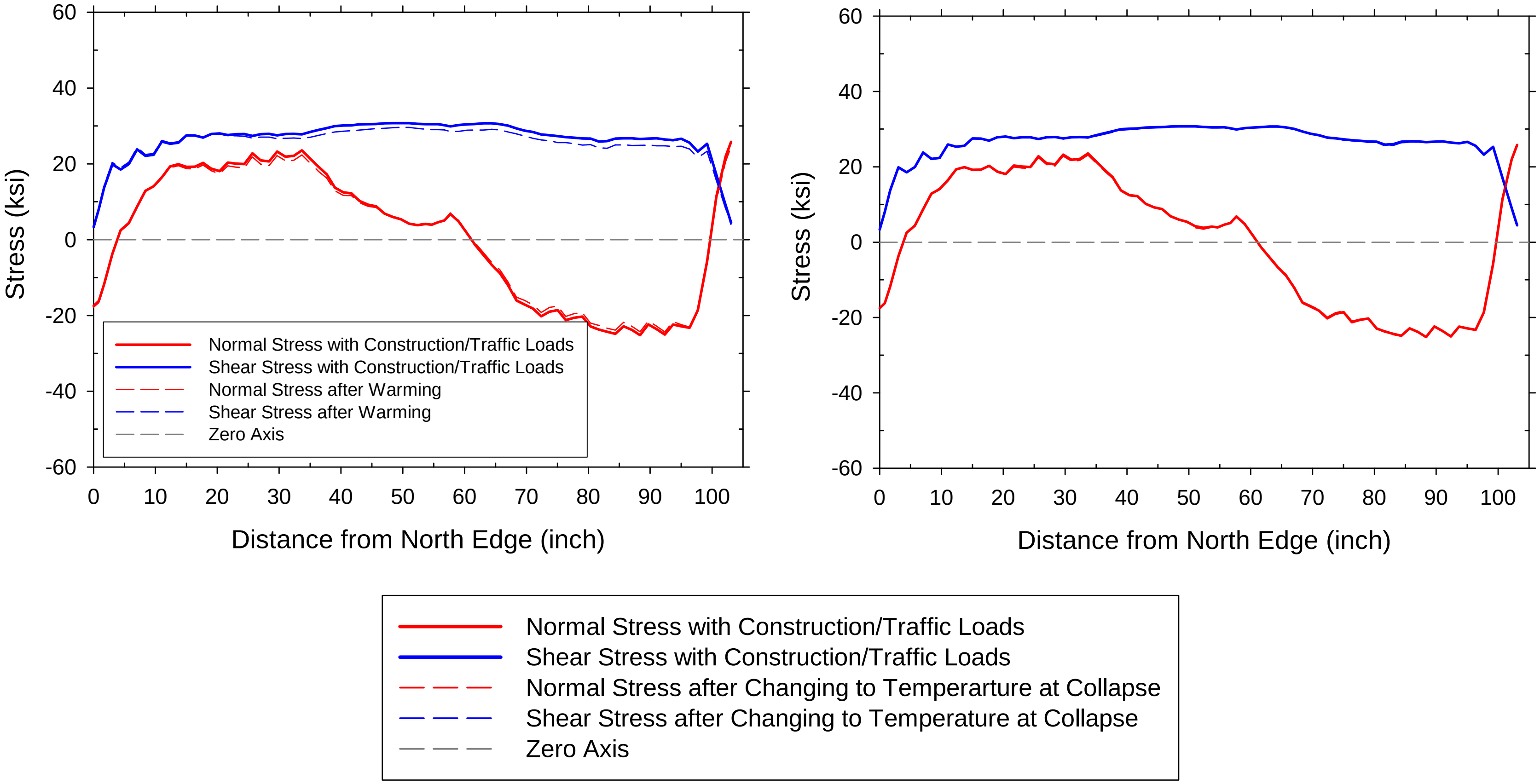

Figure 56. U10W-West plate section A-A stress distributions due to non-uniform temperature. Bearings locked at 59 °F (left). Bearings locked at 102 °F (right).

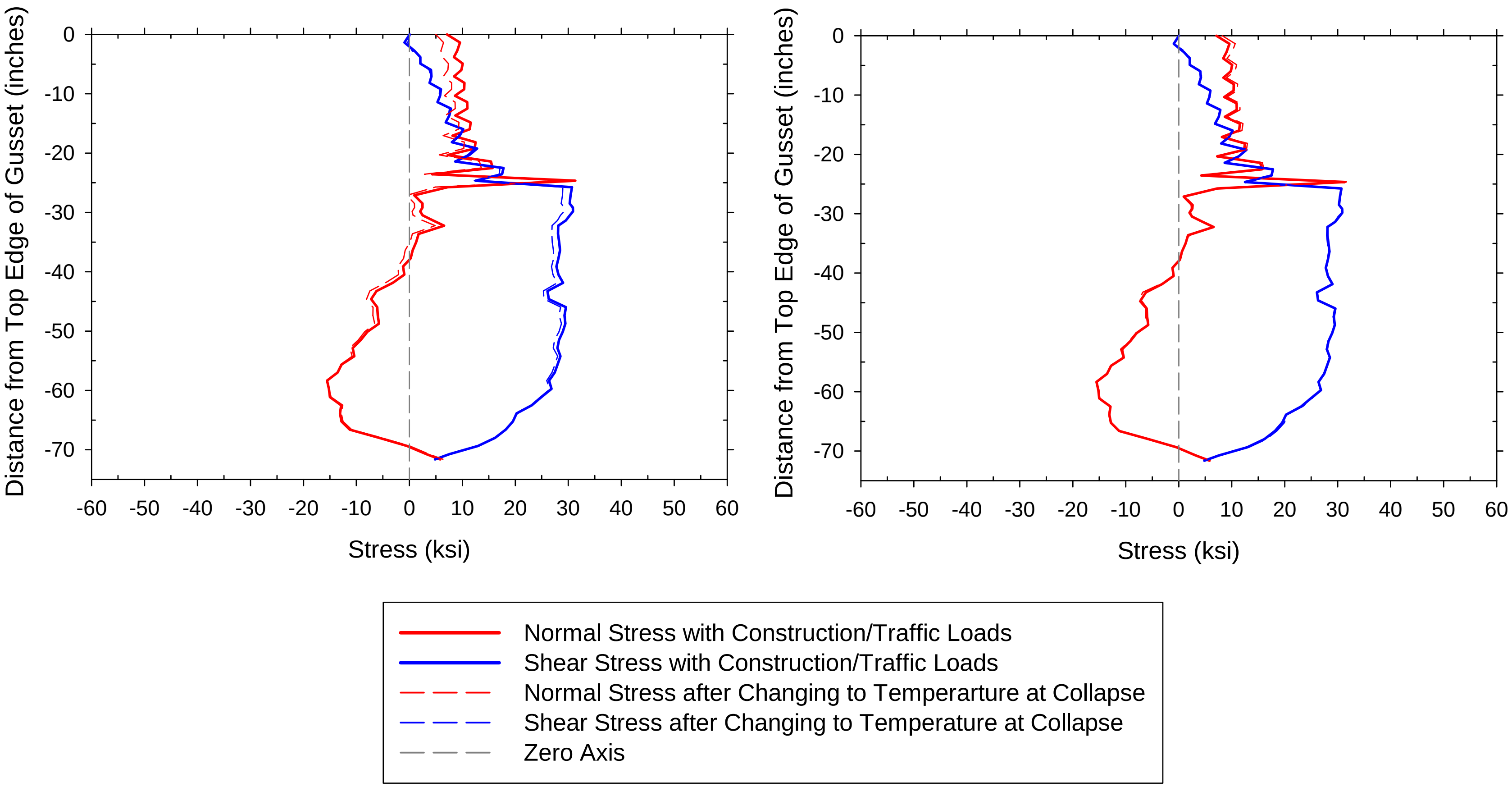

Figure 57. U10W-West plate section B-B stress distributions due to non-uniform temperature. Bearings locked at 59 °F (left). Bearings locked at 102 °F (right).

CHAPTER 6. DECK STIFFNESS

A sensitivity study was performed to determine if variations in concrete modulus have a significant effect on model results. Based on measurements taken in a few deck core samples, the concrete modulus was determined to be 4,800 ksi. However, the small sample size and the inherent variability of this test procedure reduces the overall confidence in this value. A parametric study was performed where the deck concrete modulus was varied from 1500-7000 ksi. This chapter discusses the results of this study that only used the As-Built (2007) model.

RESULTS

For this investigation, the area of interest is primarily the U10W connection; therefore the comparisons will involve only the U10W joint. Specifically, the translations and rotations of node 40328 (the intersections of the U10W members) will be compared as well as the axial forces of all members framing into the U10W joint.

Table 31 outlines the data collected for the U10W member axial forces at the end of step 4 for the six different deck modulus values. In addition, Tables 32 and 33 are similarly formatted showing the three components of translation and rotation for the node representing the intersection of all five U10W members. Also shown within these tables are normalized values using the data for a 4800 ksi (the measured average) as the basis.

The normalized data represented in Tables 31-33 are graphically shown in Figures 58-60. Most of the data are insensitive to the deck modulus value and are within 1% of the data produced with the measure modulus average of 4800 ksi. The outliers are the y-rotation and z-translation (transverse direction to bridge) of node 40328. Particularly the z-translation was very sensitive to the modulus with differences varying from 40 to 12% sweeping through modulus values of 1000-7000 ksi. This is an out-of-plane displacement of the main truss which is very small and the large variation in the normalized value is partly an aberration of comparing very small numbers. In addition, the main trusses are dominated by in-plane displacements and forces, therefore small variations in out-of-plane displacements would have little affect on the overall behavior of the truss.

Table 31 Effect of Deck Modulus on U10W Member Axial Forces

	Step 4 Member Axial Force (kips) [Normalized to 4800 ksi value]					
Member	E_{deck}=1500 ksi	E_{deck}=3000 ksi	E_{deck}=4500 ksi	E_{deck}=4800 ksi	E_{deck}=6000 ksi	E_{deck}=7500 ksi
U10U9	**1962** [0.998]	**1965** [0.999]	**1966** [1.000]	**1966** [1.000]	**1967** [1.001]	**1967** [1.001]
U10L9	**-2345** [1.000]	**-2345** [1.000]	**-2345** [1.000]	**-2345** [1.000]	**-2345** [1.000]	**-2345** [1.000]
U10L10	**392** [1.009]	**391** [1.005]	**389** [1.001]	**389** [1.000]	**387** [0.996]	**386** [0.992]
U10U11	**-662** [1.011]	**-657** [1.004]	**-655** [1.000]	**-654** [1.000]	**-653** [0.998]	**-652** [0.997]
U10L11	**1906** [1.002]	**1904** [1.001]	**1903** [1.000]	**1903** [1.000]	**1902** [0.999]	**1901** [0.999]

Table 32 Effect of Deck Modulus on Node 40328 Translation

	Node 40328 Translation (inches) [Normalized to 4800 ksi value]					
Component	E_{deck}=1500 ksi	E_{deck}=3000 ksi	E_{deck}=4500 ksi	E_{deck}=4800 ksi	E_{deck}=6000 ksi	E_{deck}=7500 ksi
Global X	**0.666** [0.993]	**0.669** [0.997]	**0.670** [1.000]	**0.671** [1.000]	**0.671** [1.001]	**0.672** [1.002]
Global Y	**-4.750** [1.002]	**-4.744** [1.001]	**-4.741** [1.000]	**-4.740** [1.000]	**-4.793** [1.000]	**-4.737** [0.999]
Global Z	**-0.003** [0.591]	**-0.004** [0.841]	**-0.005** [0.979]	**-0.005** [1.000]	**-0.005** [1.067]	**-0.005** [1.129]
NOTE: X-direction is aligned with bridge longitudinal axis, Y-direction is vertical through the bridge, Z-direction is aligned transverse to bridge						

Table 33 Effect of Deck Modulus on Node 40328 Rotation

	Node 40328 Rotation (radians) [Normalized to 4800 ksi value]					
Component	E_{deck}=1500 ksi	E_{deck}=3000 ksi	E_{deck}=4500 ksi	E_{deck}=4800 ksi	E_{deck}=6000 ksi	E_{deck}=7500 ksi
Global X	**-1.061E-03** [1.012]	**-1.054E-03** [1.005]	**-1.049E-03** [1.001]	**-1.048E-03** [1.000]	**-1.046E-03** [0.998]	**-1.043E-03** [0.995]
Global Y	**1.703E-05** [1.082]	**1.615E-05** [1.026]	**1.579E-05** [1.003]	**1.574E-05** [1.000]	**1.560E-05** [0.991]	**1.549E-05** [0.984]
Global Z	**4.291E-03** [1.004]	**4.281E-03** [1.001]	**4.277E-03** [1.000]	**4.276E-03** [1.000]	**4.274E-03** [0.999]	**4.272E-03** [0.999]
NOTE: X-direction is aligned with bridge longitudinal axis, Y-direction is vertical through the bridge, Z-direction is aligned transverse to bridge						

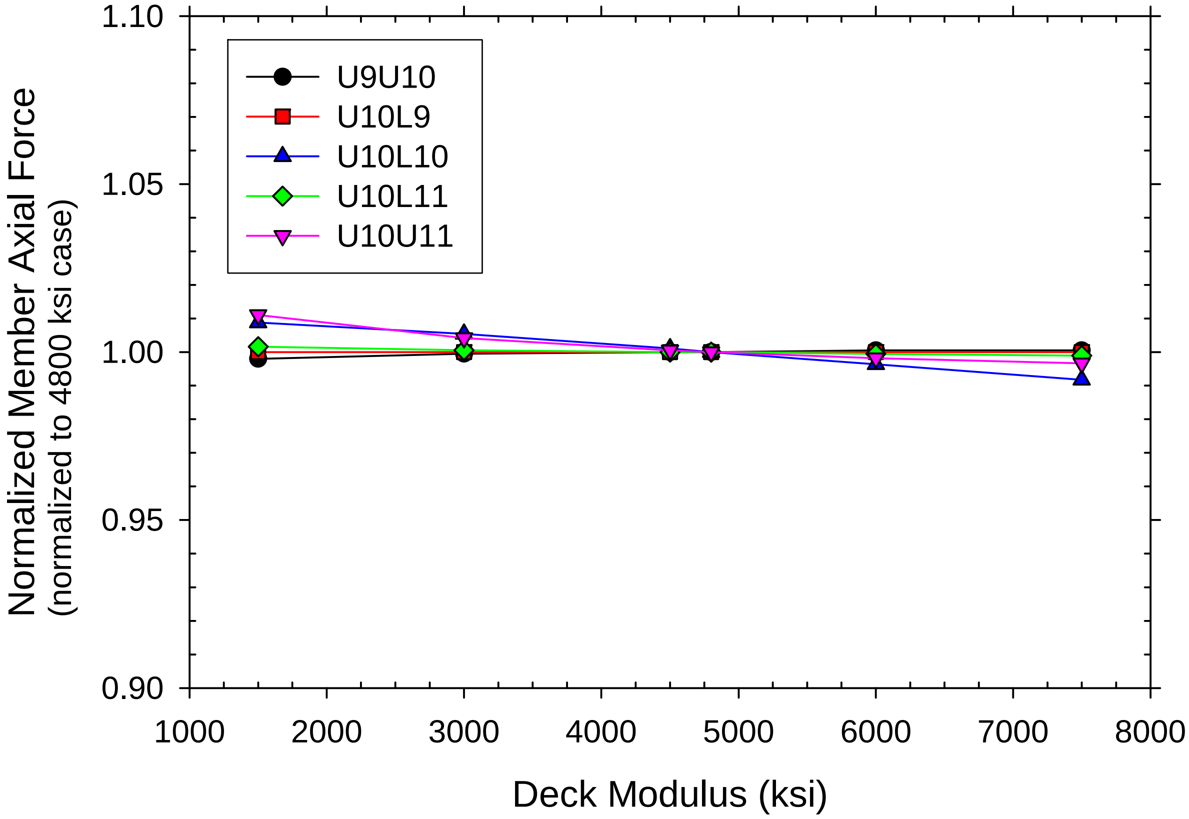

Figure 58. Effect of deck modulus on U10W member axial forces.

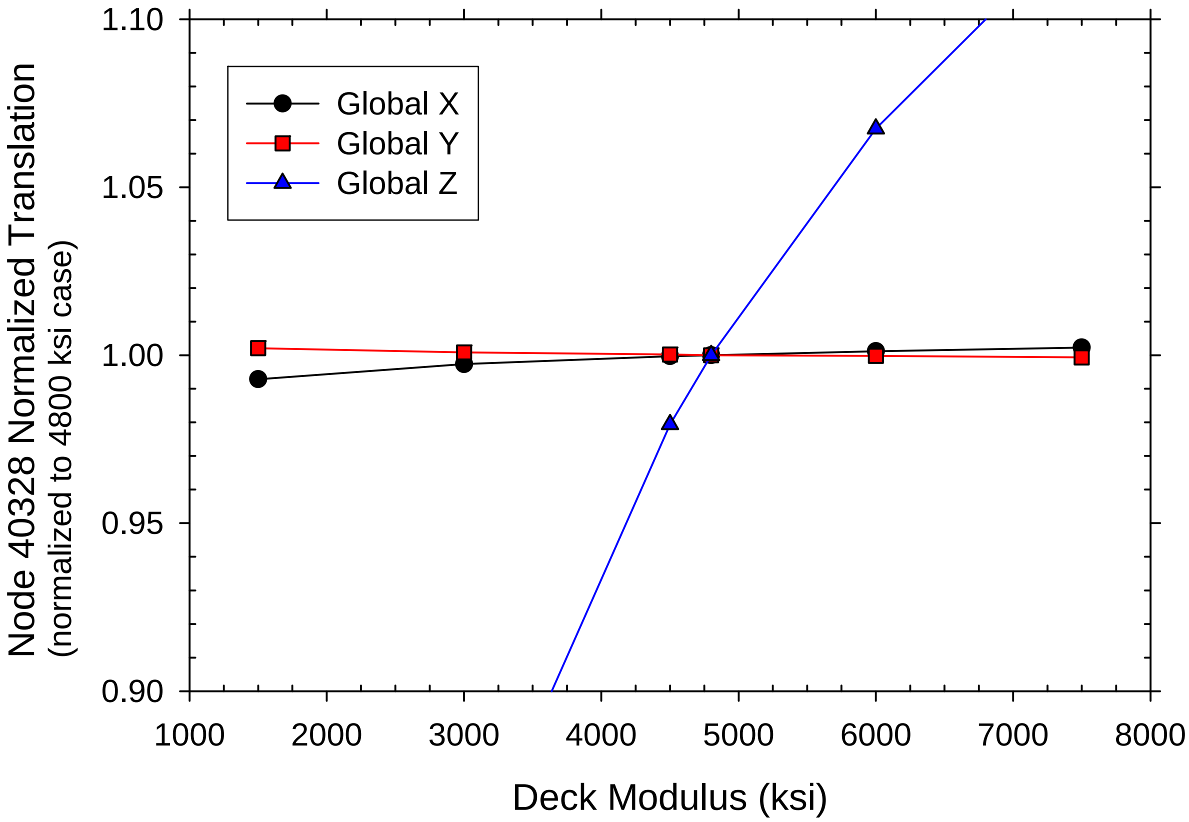

Figure 59. Effect of deck modulus on Node 40328 translation.

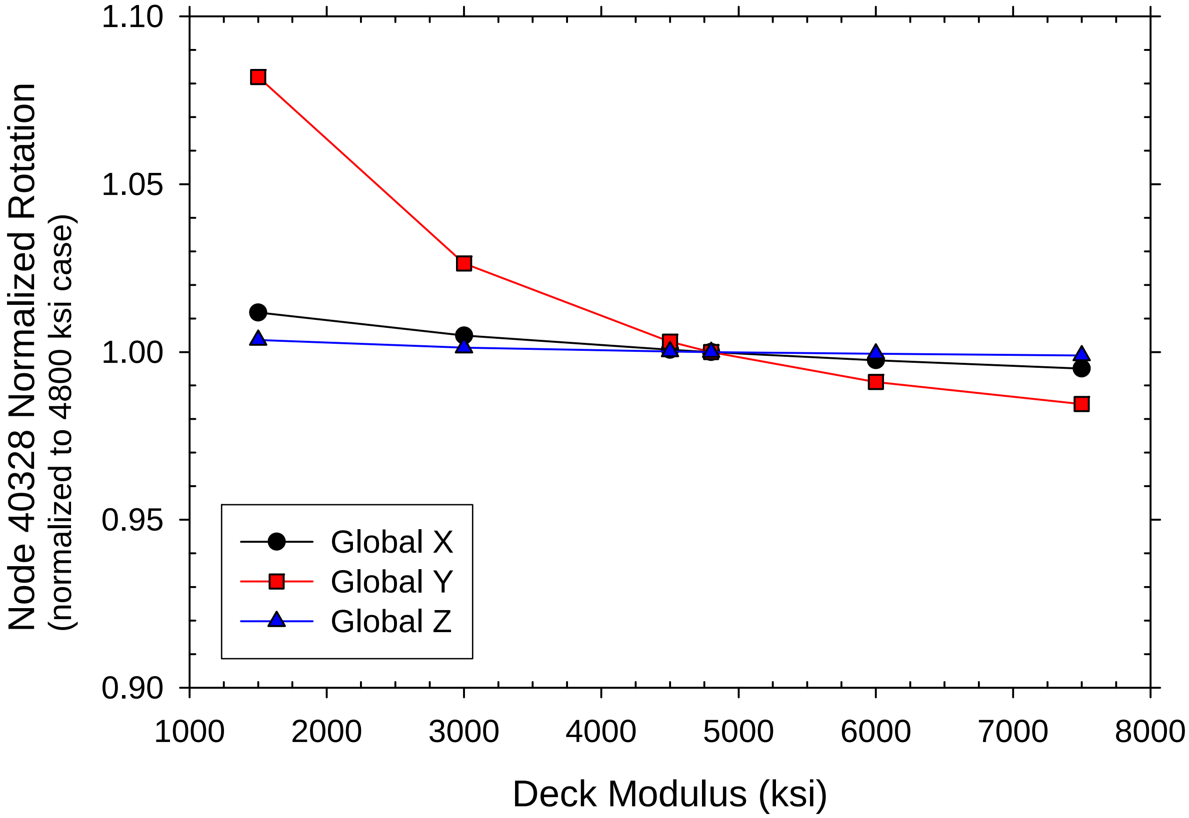

Figure 60. Effect of deck modulus on node 40328 rotation.

CHAPTER 7. INITAL IMPERFECTIONS

Photographic evidence of the four U10 connections prior to collapse distinctly show a “bowing,” or initial imperfection on the free edge of the gusset plate where the compression diagonal frames into the connection. One photo was taken by University of Minnesota personnel while applying strain gauges in August 1999. The remainder of the photos were taken during a URS inspection of the bridge in June 2003. It is not readily known when the imperfections formed nor their exact magnitude. However, the mere presence of the imperfections would locally reduce the strength of the gusset. This chapter will describe how the initial imperfections were integrated into the model and the results of their presence.

PHOTOGRAPHIC EVIDENCE

Shown in Figures 61-64 are pictures taken of the four U10 connections by URS provided to FHWA by the NTSB. In each connection, both gusset plates of each connection are shown to be bowed in identical directions. Table 34 summaries for each of the four connections the direction in which both gusset plates were bowed. All four plates on the south end of the bridge were bowed in the upstream direction (i.e. to the west) and all four plates on the north end of the bridge were bowed in the downstream direction (i.e. to the east).

The NTSB examined the photographs to estimate the magnitude and shape of the imperfections. The NTSB concluded that the imperfections had magnitudes of 0.6 inch plus/minus 0.15 inches.

MODELING

The detailed model was easily adapted to include the initial imperfections at the U10 joints. With the FEMAP preprocessor, a surface is defined in the desired shape of the imperfection, and the relevant nodes are projected onto that surface. Four edges must be specified to define the surface. Shown in Figure 65 are four red lines defining these four edges in the FHWA model. It may appear that the sides of the surface are random but the thought was to define the surface along the top edge of the U10L9 diagonal up to the snipe at the end of that member then straight up to the bottom edge of the U10U8 top chord (as shown by the black dashed line in Figure 65), along the bottom surface of the top chord, and finally down the free edge of the gusset. The left side of the surface was slightly inclined (the side connecting the diagonal and the top chord) because the surface was constructed around an existing mesh. The mesh was not changed so solid comparisons could be made between all the models.

A cubic spline defined the out-of-plane imperfection on the free edge of the plate with the maximum amplitude at the center and fading to zero displacement and zero rotation at the two ends. The other three edges of the surface were given no initial imperfection. FEMAP then fits a surface to these four edges. A picture taken from the model showing a portion of the gusset plate with an imperfection made with this technique is shown in Figure 66.

Modeling the imperfection in this manner introduces a stress-free imperfection in the plate from the beginning of the analysis. However, it is very likely that the imperfections shown in the photographs where due to some event within the life of the bridge between construction and 1999. No plausible scenarios were found that would cause an imperfection to initiate in the gusset using the computer models, so the proper stress state could not be represented within the plate.

Three additional models were made with imperfection amplitudes of 0.5, 0.7 and 0.75 inches. The three models with the imperfections and the original model were given a sixth analysis step and run in two different ways. The sixth step ramped up either the construction/traffic loads or dead load using the *AMPLITUDE command until Abaqus could no longer converge to a solution. Amplifying the dead load represents a general increase in load across the entire bridge, while amplifying the construction/traffic loads creates a more concentrated load effect. The point of non-convergence corresponds to the critical buckling capacity of the U10 gusset plates. The analysis was run with default Abaqus parameters for auto-incrementation where the program selects the appropriate increment size and terminates analysis when increment size must become smaller than 0.00001 to maintain convergence. This technique gives an indication of how close the gusset plates were to their buckling capacity under the two load scenarios.

RESULTS

Table 35 outlines the percentage increase in either the construction/traffic loads or dead load required to reach the critical buckling load of the U10 gusset plates. The additional load magnitude is also shown along with the percentage increase. With perfect geometry, the gusset plates buckled with 33.5% more construction/traffic load or 7.0% dead load. Figure 67 shows the deformed shape (x10 amplification) of the U10 east and west connections at the critical buckling load for the model with no initial imperfections. The critical buckling mode shape in this case shows both U10L9 diagonals are moving out-of-plane towards the inside of the bridge. This is contrary to the wreckage evidence that shows both U10L9 diagonal moved to the west.

When the imperfections were introduced into the gusset plates, the critical buckling load decreased as the imperfection amplitude was increased. With the maximum 0.75 inch initial imperfection, the model predicted only 1.8% additional construction/traffic load (17 kips) or 0.34% additional dead load (56 kips) to reach the critical buckling load. More importantly, Figure 68 shows that the buckled shape changes so that both U10L9 diagonals now buckle together to the west. This matches the evidence in the bridge wreckage. Figure 69 shows a deformed view of the U10W connection from outside the bridge depicting how the gusset plate is forced to wrap around the compression diagonal as it moves out-of-plane which again matches the physical evidence.

The NTSB mapping of the construction and traffic load on the bridge at the time of collapse is estimated to have a potential error of plus/minus 5%. This means the construction/traffic load could be as much as 48 kips higher than that applied to the model. As described in a previous chapter, the dead load was considered to be within 300 kips of that used in the model. Therefore, with the initial gusset plate imperfections shown in the pre-collapse photos (0.5 to 0.7 in.), the analysis model predicts that sidesway buckling of the gusset plate at U10 is expected within the best estimates of the total weight (live load + dead load) known to be on the bridge.

At the point when the U10 gusset plate first buckles, the maximum Von Mises stress was only 71.6 ksi at an equivalent plastic strain of 0.0282. However, based on the tension specimens made from the U10 gusset plates, they could achieve a stress on the order of 88 ksi at a strain in excess of 0.1. Therefore, even though conventional static analysis predicts the onset of buckling in the gusset plate, the bridge has yet to fail within the computer. To overcome this, some of the models were analyzed with the RIKS algorithm. The RIKS algorithm is a form of a static analysis that has the ability to predict post-buckling behavior. Specifically, the RIKS analysis was performed on the model with 0.5 inch initial imperfections that amplified the dead loads. In this analysis, the out-of-plane displacements of two nodes on the east and west diagonals were tracked throughout the entire analysis. The nodes were located on the gusset at the end of the U10L9 diagonals. Figure 70 plots the lateral displacement of these two nodes versus the total vertical load carried by the bridge. At the point the RIKS analysis was terminated, the west diagonal had moved over three inches laterally (shown in Figure 71) with a maximum stress of 94 ksi and a strain of 0.56. The peak load at the onset of buckling was never attained later in the analysis, indicating that the gusset plate was unable to achieve a stable equilibrium state after buckling. The stress and strain in the west gusset plate at the point where the analysis was terminated exceeds the expected tensile capacity of the material. Therefore, it can be concluded that material failure will occur before a stable equilibrium state can be attained for the buckled gusset plate.

Figure 61. Picture of U10E connection taken on 12 June 2003.

Figure 62. Picture of U10W connection taken on 10 June 2003.

Figure 63. Picture of U10’E connection taken on 12 June 2003.

Figure 64. Picture of U10’W connection taken on 10 June 2003.

Table 34 Direction of Initial Imperfections of U10 connections

Connection	Direction of Initial Imperfection
U10East (see Figure 61)	Upstream (west)
U10West (see Figure 62)	Upstream (west)
U10’East (see Figure 63)	Downstream (east)
U10’West (see Figure 64)	Downstream (east)

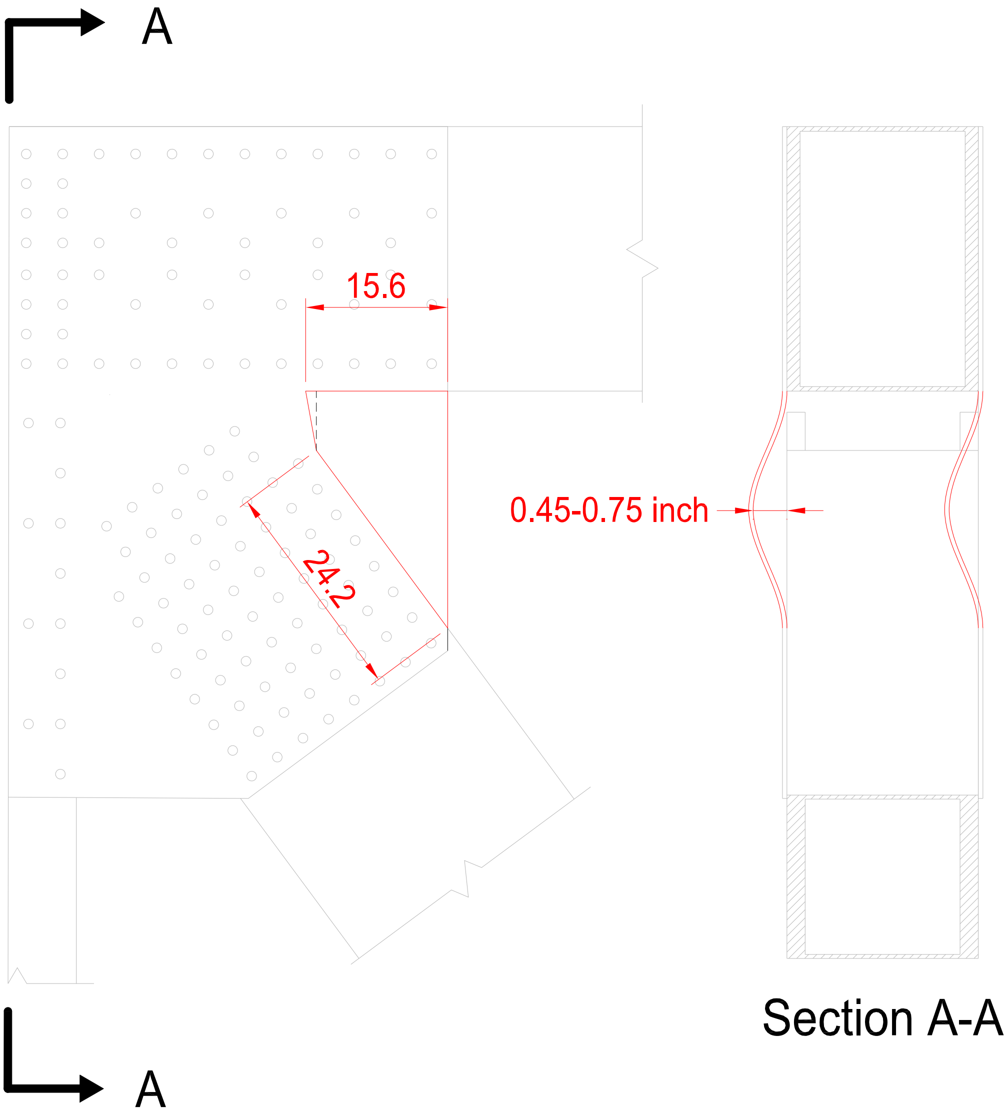

Figure 65. TFHRC modeling of gusset plate imperfections.

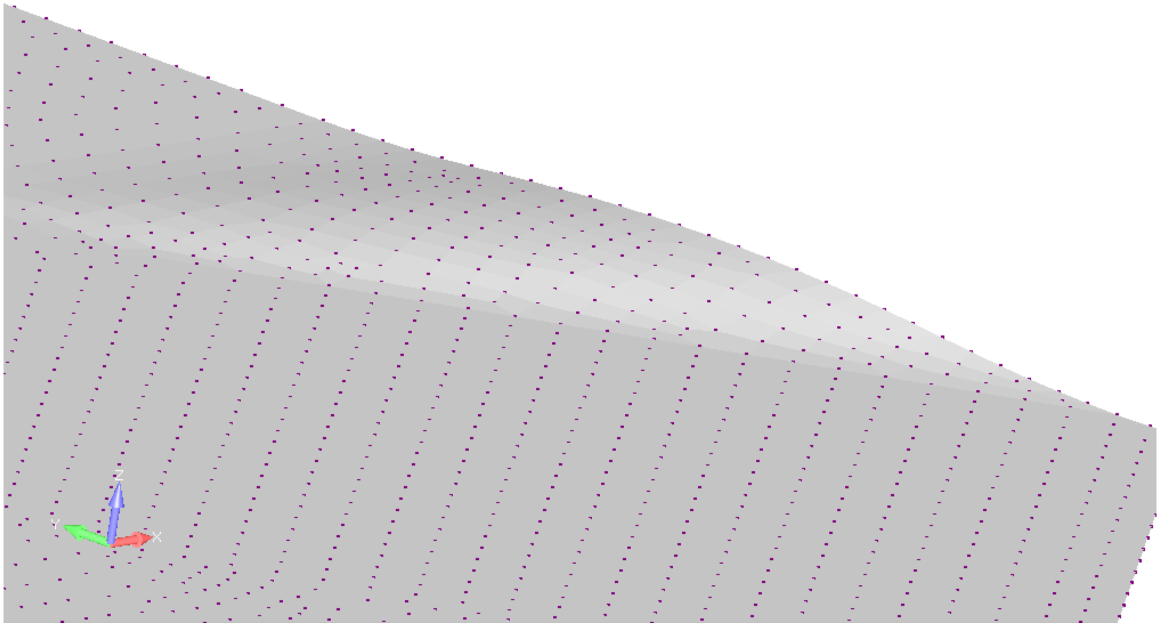

Figure 66. View of TFHRC imperfection surface.

Table 35 Percentage Increases in Load to Achieve the Limit Load.

	Percentage Increase in Load to Cause Non-Convergence [corresponding load, (kips)]	
Size of Imperfection	Construction/Traffic Load[a]	Dead Load[b]
Perfect Geometry	33.5 % [320 kips]	7.0 % [1156 kips]
0.5 inch	22.2 % [212 kips]	4.2% [701 kips]
0.7 inch	4.9% [47 kips]	1.0% [159 kips]
0.75 inch	1.8% [17 kips]	0.34% [56 kips]

[a] – Proportioned construction/traffic loads included only construction/traffic loads on the deck truss (did not proportion the approach span reactions) outlined in NTSB Report 07-115[1]

[b] – Proportioned dead load only included the weight of all the steel and the original 6.5 inch thick deck

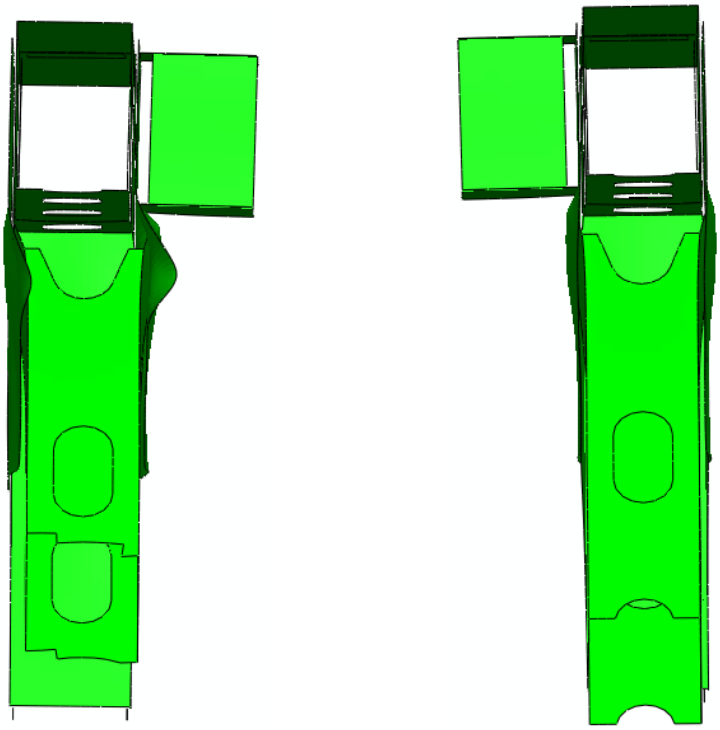

Figure 67. Deformed view (looking north) of U10W (left) and U10E (right) at the critical buckling load, with initial perfect geometry.

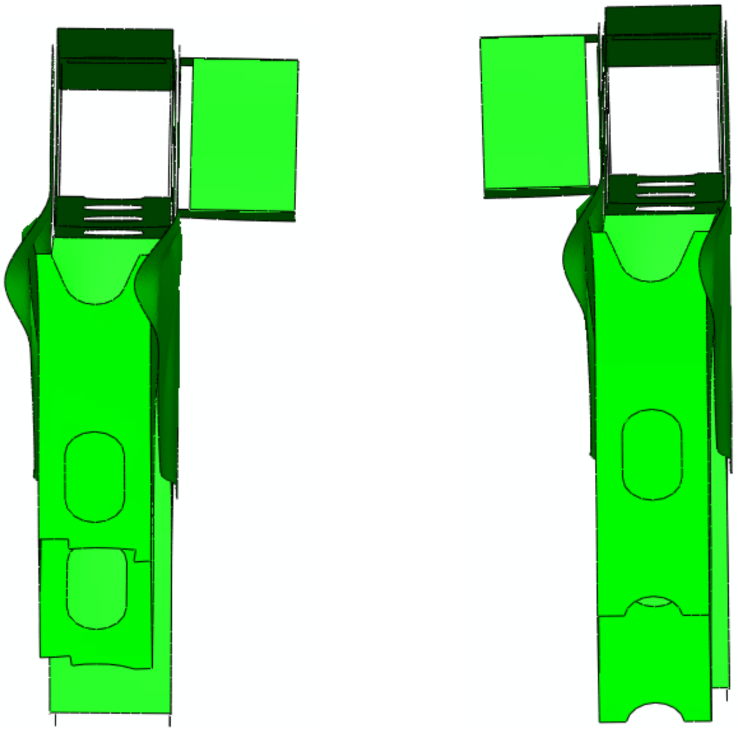

Figure 68. Deformed view (looking north) of U10W (left) and U10E (right) at the critical buckling load, with 0.7 inch initial imperfection.

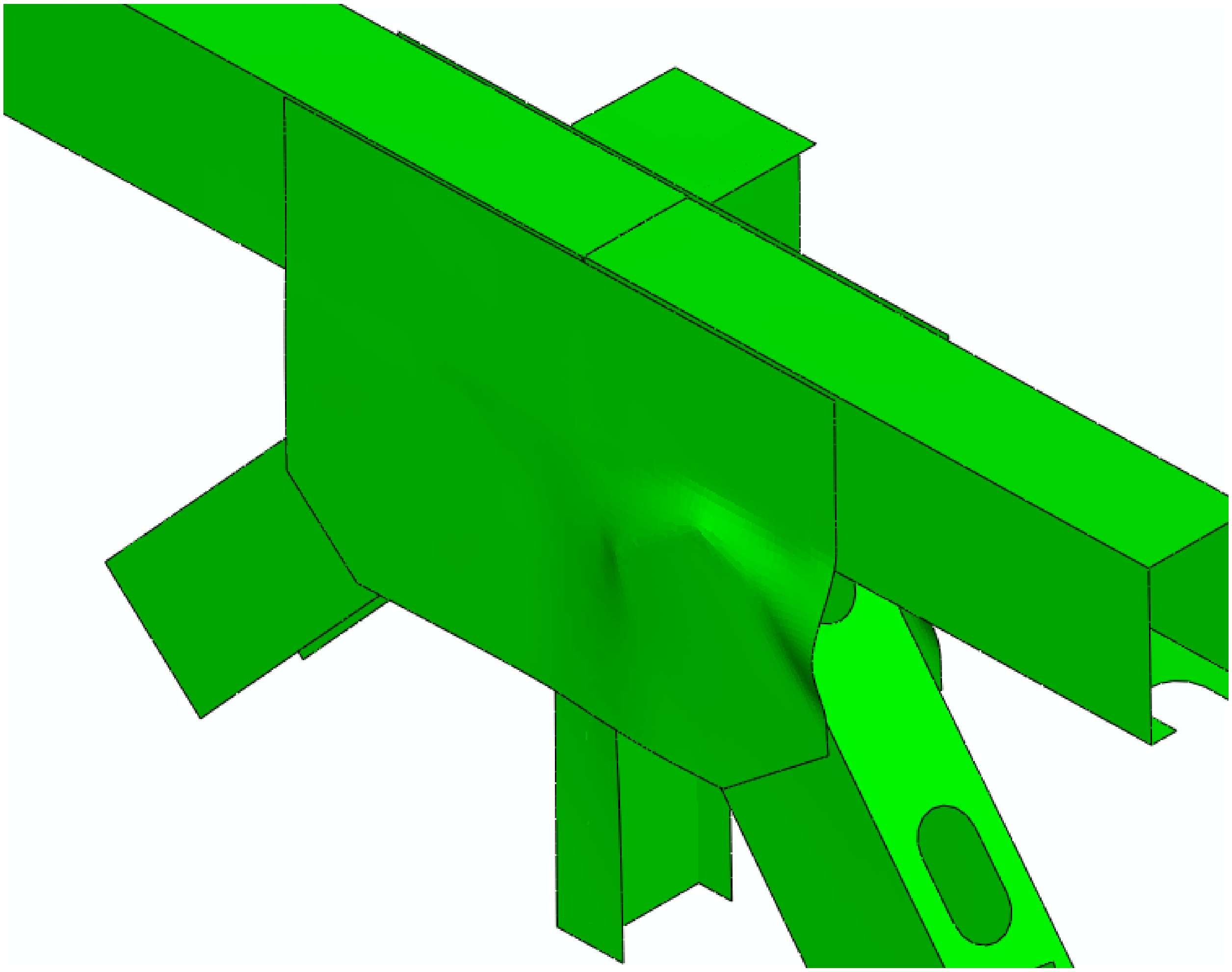

Figure 69. Exterior view of U10W at the critical buckling load with 0.7 inch initial imperfection.

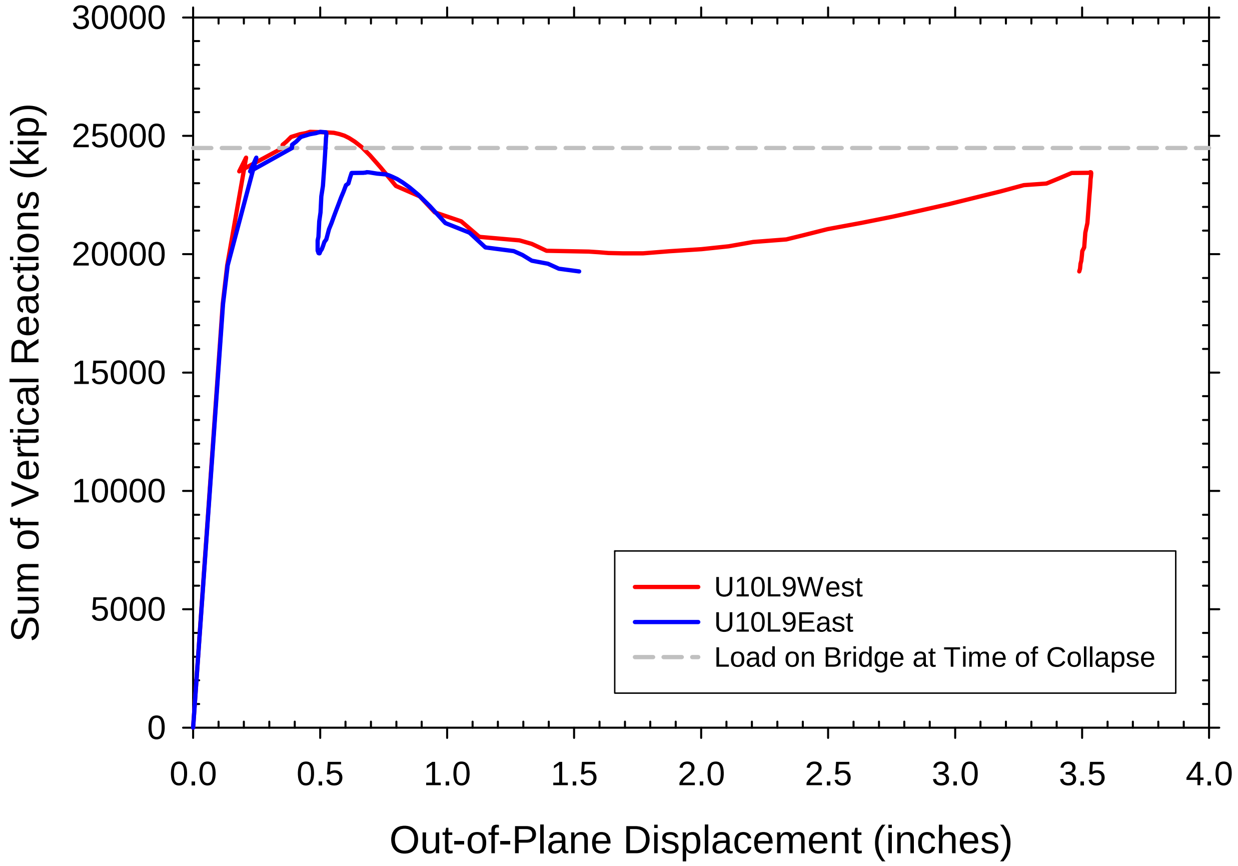

Figure 70. Equilibrium path of U10L9 diagonal throughout RIKS analysis.

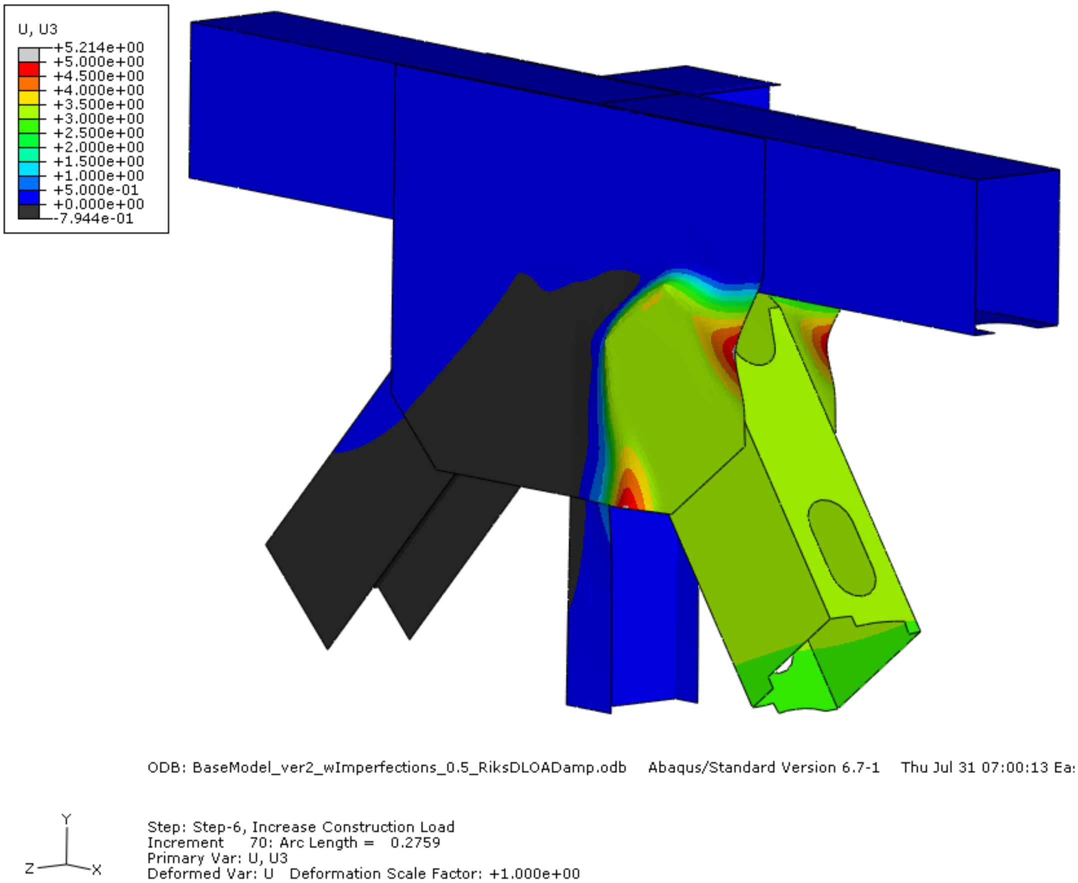

Figure 71. Out-of-plane displacement contour of U10W at termination of RIKS analysis with 0.5 inch initial imperfection.

CHAPTER 8. EFFECT OF MODEL COMPLEXITY

The FHWA model used shell element representations for both the L11 and U10 connections in both main trusses. However, the highly detailed solid model developed by the NTSB generally focused on the U10W connection alone at a detailed level, the L11W, U10E, and L11E connections were not specifically modeled. Depending on the failure mode, limiting the model to focus only on U10W could possibly alter the internal force redistribution in the bridge prior to failure. This could also mask the presence of any possible failure modes involving more than one joint. Therefore, the FHWA model was modified to understand how the critical buckling load predictions might change if the model only included detailed representations of either both U10 connections or just the U10W connection alone.

RESULTS

As was done with the initial imperfection study, construction and dead loads were amplified until the model could no longer converge to a solution. However, two additional models were created, the first did not include the detailed L11 joints. The second only included a detailed representation of only the U10W joint. Table 36 outlines how the percent increase in load changes as the model complexity is changed. As expected, the model is stiffer when the detailed models are not included and a higher critical buckling load is achieved. For instance, when transitioning from modeling both U10 and L11 joints to just modeling U10W, the critical buckling load increased by 61 kips when amplifying only the construction loads, and by 234 kips when amplifying only the dead loads. Therefore, modeling only the U10W connection tends to produce un-conservative critical buckling load predictions. However, the difference is a maximum of 6.4% in the case of amplifying the construction/traffic loads.

Table 37 outlines the axial forces in the ten members framing into the two U10 connections from each of the three models with different complexity. Again, differences are expected because inherently including a shell element representation of the connection would have to have more flexibility than a rigid node between five adjoining members. The forces do change from one model to the next, but the differences are small. In the worst case there was a 19 kip difference.

Table 36 Critical Buckling Load Predictions for Models with Different Complexity

	Percentage Increase in Load to Cause Non-Convergence [corresponding load, (kips)]	
Connections with Shell Element Representation	Construction/Traffic Load[a]	Dead Load[b]
Both U10 and L11 joints	33.5 % [320 kips]	7.0 % [1156 kips]
Both U10 joints	38.8 % [371 kips]	7.6 % [1263 kips]
Just U10West	39.9 % [381 kips]	8.4 % [1390 kips]

[a] – Proportioned construction/traffic loads included only construction/traffic loads on the deck truss (did not proportion the approach span reactions) outlined in NTSB Report 07-115[4]

[b] – Proportioned dead load only included the weight of all the steel and the original 6.5 inch thick deck

Table 37 Member Axial Forces for Models with Different Complexity

	Axial Load with all dead load and construction/traffic loads (kips)		
	Both U10 and L11 connections modeled	Just U10W and U10E	Just U10W
U10U9 West	1989.4	1992.4	1990.5
U10L9 West	-2391.6	-2393.9	-2390.7
U10L10 West	398.7	397.8	396.5
U10L11 West	1931.6	1933.5	1932.0
U10U11 West	-647.6	-647.2	-648.1
U10U9 East	1952.7	1955.1	1969.2
U10L9 East	-2294.3	-2296.4	-2298.8
U10L10 East	373.5	372.9	370.7
U10L11 East	1869.5	1870.5	1879.6
U10U11 East	-604.6	-604.1	-623.2

CHAPTER 9. ALTERNATE GUSSET PLATES

The designed thickness of the U10 and L11 gusset plates was determined to be an important aspect of the failure. It is estimated that the as-built U10 and L11 gusset plates were only half the thickness required for a proper design with grade 50 material Therefore, the FHWA model was used to explore the effects of these two alternate gusset plate designs. In one alternate model, the thickness of the shell elements in the U10 and L11 gusset plates was increased from 0.5 in. to 1.0 in. A second alternate model changed the non-linear material properties of the U10 and L11 gusset plates to that of a typical grade 100 steel. The following sections will describe the results of these two analyses.

CHANGES TO THE MODELS

Since the localized models of the U10 connections were meshed with shell elements, input files for these two models were easy to change for the alternate models. Element groups were setup for the U10 gusset plate elements. Changing the thickness or material for these elements was literally a matter of changing a couple numbers in the input files. This created a minor error for the 1.0 inch gusset plate model since the centroidal distance of the gusset plate elements was not updated to reflect the additional plate thickness. This assumption is expected to have little effect on the results.

RESULTS

As in the previous sections, the two alternate designed models were each subjected to two load amplification scenarios. After all the known load was applied to the model, an additional final step was added to the analysis. This final step continued to proportion either the dead or construction/traffic loads until the bridge reached its critical failure load.

Table 38 shows the non-convergence load for three design cases for each of the two load amplification scenarios. As expected, the two altered models attained much higher loads than the as-built bridge that used ½ inch, 50 ksi gusset plates. Recall that the model of the as-built bridge assuming perfect geometry needed 33.5% more construction load or 7% more dead load to reach the critical buckling load. These numbers increased to 547% or 81% respectfully for the 1/2 inch thick gusset plate with grade 100 material and 654% or 75% for the 1 inch thick gusset plates with grade 50 material.

Similar to the ½ in. thick grade 50 model, the point of non-convergence corresponded to the critical buckling load of the gusset plates at the four joints where the detailed connection models exist. The buckled shape, however, differed somewhat for the alternate gusset plate designs. It should be noted that buckling failure was only possible at the detailed shell model locations in the model. This may have artificially forced the first failure to occur at the U10 and L11 joints.

Failure Mode of ½ in. Plate, Grade 100 Material

When the construction/traffic load was amplified, the critical buckling load was reached when the U10L9 diagonal on the west truss moved out-of-plane to the inside of the bridge at U10. This is shown in Figure 72. Simultaneously, the U12L11, and U11L11 members at the L11W connection were beginning to move out-of-plane to the outside of the bridge as shown in Figure 73. This suggests the bridge would have ultimately failed by gusset plate buckling at multiple locations. A Von Mises stress contour plot is shown in Figure 74 of the U10W-west gusset plate at the critical buckling load when the construction/traffic load was amplified. The plot is scaled to show stress levels between 100-115 ksi, therefore elastic portions of plate are shown in black. This plot shows that the yielding in the gusset plate was limited to two small areas around the tip of the compression diagonal. This indicates the failure mode was predominately elastic, side-sway buckling of the U10 gusset plates.

When the dead loads were amplified in the model, the failure mode was different. In this case, the critical buckling load was reached when the U12L11W diagonal swayed out-of-plane to the outside of the bridge at the L11 joint, similar to the mode depicted in Figure 73. A Von Mises contour plot of the U10W-west gusset plate is shown in Figure 75 at the point where the critical buckling load is reached at L11. There appears to be a larger area of yielded material at the end of the compression diagonal compared to that shown for the construction/traffic load amplification scenario. However, no side-sway buckling was observed at U10.

Regardless of the load amplification scenario, the yielded area in the grade 100 gusset plate was significantly smaller than in the case with the grade 50 plate. For instance, the yielded area pattern shown in the top of Figure 27 for the as built bridge with ½ inch, grade 50 plate is very similar the pattern shown in Figure 75 for the grade 100 material. However, the major difference between the two scenarios is the load on the bridge at the point the contour was generated. In the case of the grade 50 plate material, the bridge was holding 19,530 kips of total load versus 36,825 kips for the grade 100 material, nearly a 100% difference.

Failure Mode of 1 in. Plate, Grade 50 Material

In both load amplification scenarios for the 1 inch U10 gusset plates, the critical buckling load occurred when the both the U12L11 and U11L11 members in the L11W connection swayed to the outside of the bridge. In the dead load amplification scenario, the U12L11 member of L11E connection also swayed to the outside of the bridge coincident with the two members in the L11W connection.

Figures 76 and 77 plot the Von Mises contour plots of the U10W-west gusset plate for the two loading scenarios when the critical buckling load was reached at L11. The contours are scaled from 50 to 70 ksi so the black area indicates elastic material. In both scenarios, the yielded area was primarily limited to a small region at the end of the compression diagonal.

Table 38 Additional Load Needed to Reach Critical Buckling Load

	Percentage Increase in Load to Cause Non-Convergence [corresponding load, (kips)]	
Type of gusset plate	Construction/Traffic Load[a]	Dead Load[b]
½ inch, 50 ksi yield	33.5 % [320 kips]	7.0 % [1156 kips]
½ inch, 100 ksi yield	547 % [5224 kips]	81 % [13327 kips]
1 inch, 50 ksi yield	654 % [6244 kips]	75 % [12369 kips]

[a] – Proportioned construction/traffic loads included only construction/traffic loads on the deck truss (did not proportion the approach span reactions) outlined in NTSB Report 07-115[4] (955.2 kips)

[b] – Proportioned dead load only included the weight of all the steel and the original 6.5 inch thick deck (16531.6 kips)

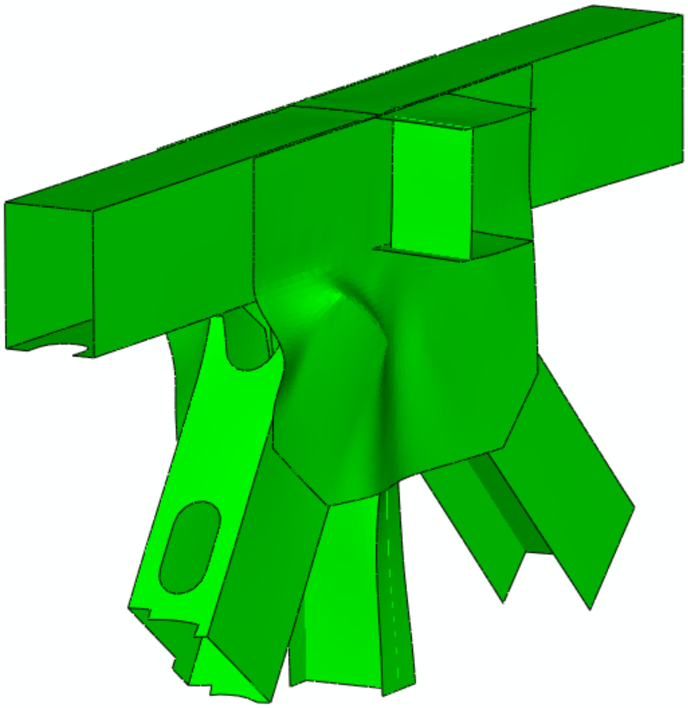

Figure 72. Deformed view of U10W connection with ½ inch, grade 100 gusset plates for the construction load amplification scenario (x10 deformation).

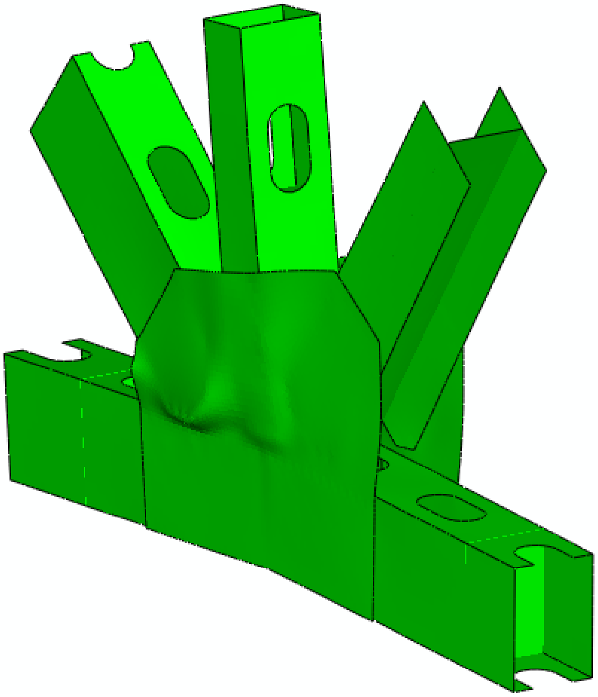

Figure 73. Deformed view of L11W connection with ½ inch, grade100 gusset plates for the construction load amplification scenario (x10 deformation).

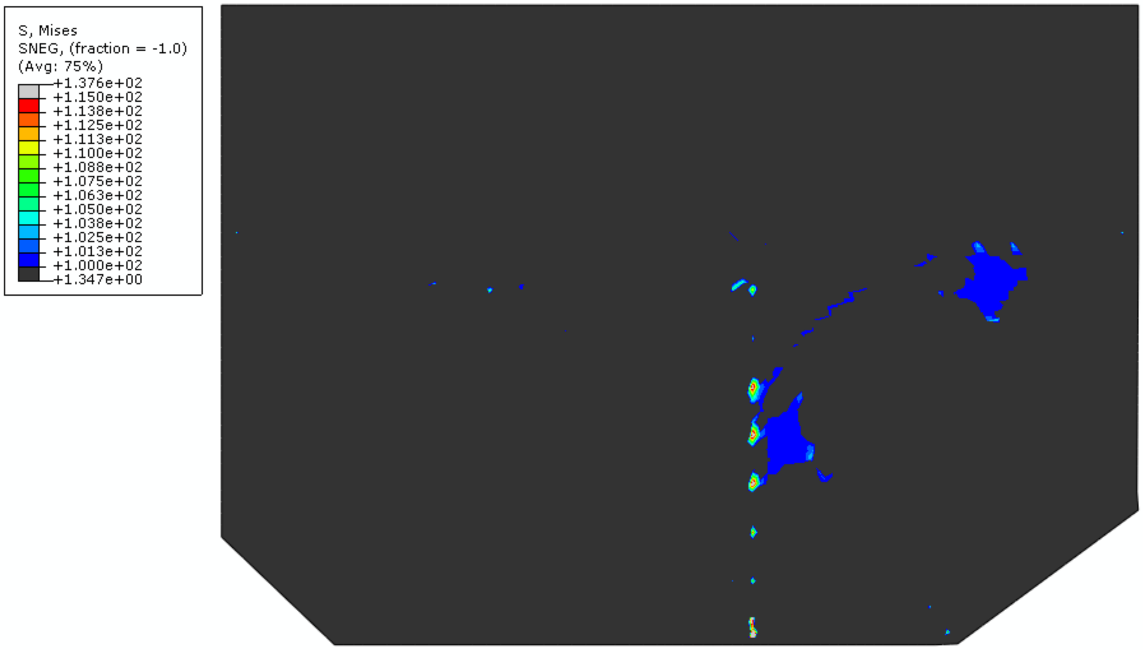

Figure 74. Von Mises stress contour (100-115 ksi) at the critical buckling load of U10W-west gusset plate with ½ inch, grade 100 material and the construction/traffic load amplification scenario.

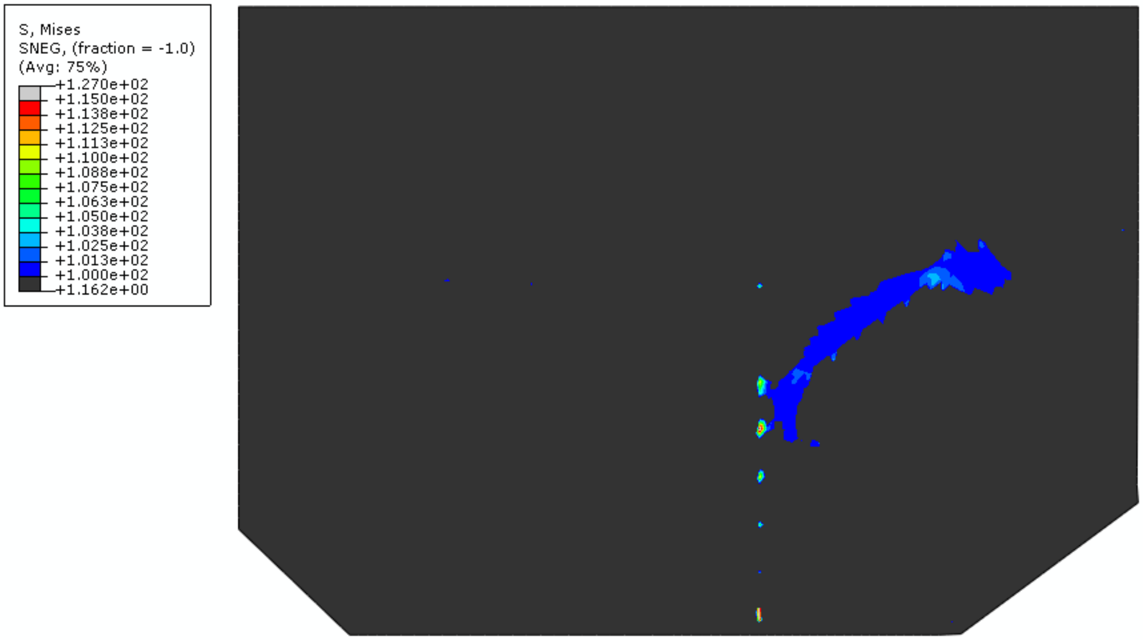

Figure 75. Von Mises stress contour (100-115 ksi) at the critical buckling load of the U10W-west gusset plate with ½ inch, grade 100 material and the dead load amplification scenario.

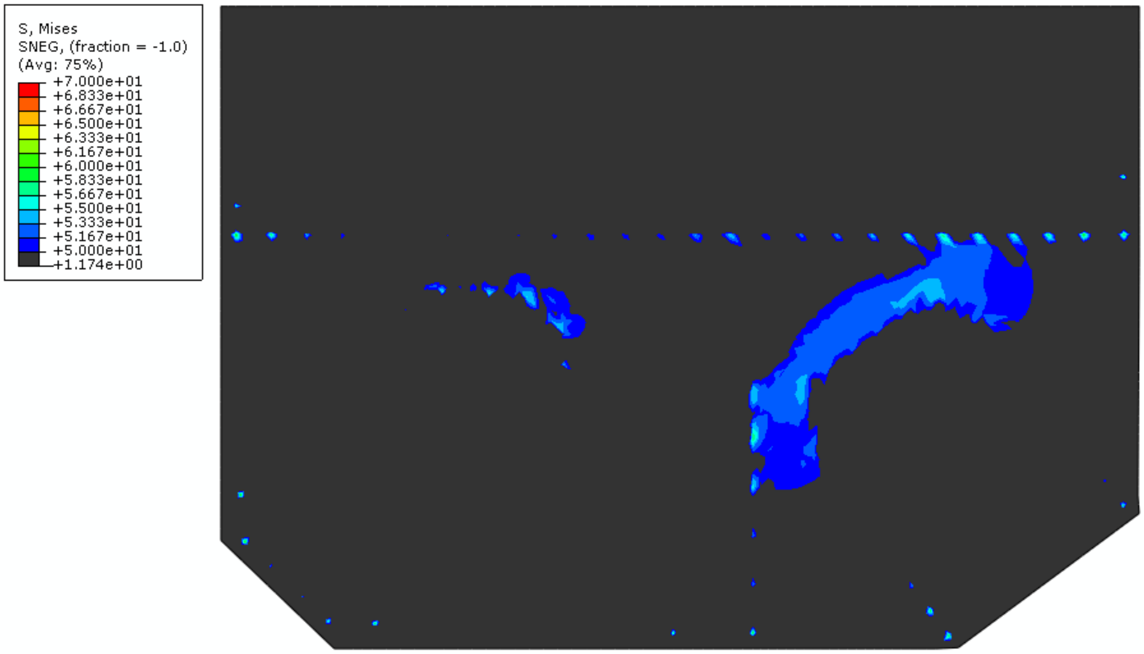

Figure 76. Von Mises stress contour (50-70 ksi) at the critical buckling load of the U10W-west gusset plate with 1 inch, grade 50 material and the construction/traffic load amplification scenario.

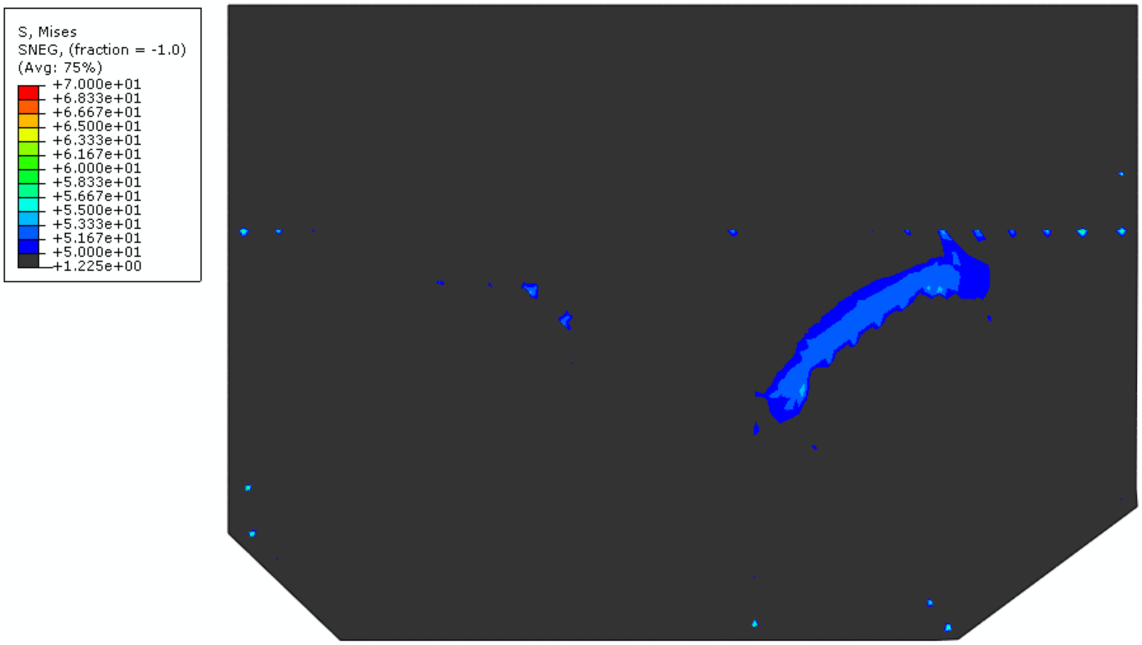

Figure 77. Von Mises stress contour (50-70 ksi) at the critical buckling load of the U10W-west gusset plate with 1 inch, grade 50 material and the dead load amplification scenario.

CHAPTER 10. CONCLUSIONS

Various finite element models were created using Abaqus to provide insight into the failure mechanism of the I-35W bridge collapse. A significant effort was put towards constructing a model with the capability to capture the true behavior of the bridge. The overall FHWA global model was calibrated to live load data collected by the University of Minnesota in 1999. This eliminated many of the unknowns common to bridge modeling related to boundary condition assumptions. The FHWA global model results were compared to results from an independent model constructed by BSDI. Good correlation was shown between the two models, thus providing a source of peer review and verification of accuracy.

Evidence from the wreckage site pointed strongly to failure initiating at the U10 connections. However, there was also concern that corrosion subsequently identified on the L11 connections may have also contributed to the collapse mechanism. The FHWA global model was amended by embedding detailed shell models of the U10 and L11 connections on both the east and west trusses. This model could then be used to explore the various possible scenarios that may have initiated the collapse. The FHWA detailed model was specifically used to investigate the effect of thermal loading and gusset plate corrosion at the L11 joints. The following specific conclusions can be drawn based on this work:

- The gusset plates at joints U10 and L11 were clearly under sized for both the design forces and for the forces present in the I-35W bridge at the time of collapse. Non-linear stress analysis of the U10 gusset plates without initial imperfection predicts that the region immediately at the end of the compression diagonal (U10L9) would have been at its yield strength when the bridge was initially constructed in 1967. From the time the bridge was first opened to traffic up to the late 1990’s, the weight of the bridge (steel and concrete) increased by 24% from 19531 kips to 24085 kips. The additional dead load greatly expanded the region of yielding around the end of the compression diagonal and across the horizontal A-A plane through the gusset plates. The presence of construction/traffic loads at the time of failure increased the area of yielded material even further. Similar results are observed in the L11 gusset plates, with yielding primarily at the end of the compression diagonal (U12L11). Even though significant areas of the two L11 gusset plates were at their yield criteria, no yield failure planes were observed and there was no significant plastic strain in the plates. In all cases, elastic material surrounding the yielded areas provided sufficient constraint to prevent total yielding failure.

- Two different alternate design scenarios were investigated for the gusset plates at U10. In one case the plate thickness was increased from 0.5 inch to 1.0 inch. In the second case the yield strength of the 0.5 inch gusset plates was increased to 100 ksi. Both of these alternate scenarios eliminated the areas of yielding observed in the as-built gusset plates. Although a thorough design check of these alternates was not performed, the analytical results show that either of these two alternates would have resulted in stress levels that would be consistent with a proper design. It should be noted that the 0.5 inch, 100 ksi re-design would not have met the edge slenderness limit present in the 1961 AASHTO Standard Specifications for Highway Bridges for low-alloy steels.

- Thermally induced forces in the truss members are difficult to accurately predict since they are based on numerous assumptions. While the ambient temperature is accurately known from weather data, the bridge temperature can vary significantly due to thermal lag and gradient effects. More importantly, assumptions must be made concerning operation of the bearings. Evidence from the wreckage and the thermal movement study conducted by URS indicate that the bearing behavior ranged from fully to partially operational and were certainly moving during winter-summer temperature cycles. This study investigated two cases where the bearings were locked with respect to minor temperature changes that might be expected for a day-night cycle in the summer. Though the axial force within certain members framing into U10 increased significantly from thermal changes (up to 20% of the dead load), the stresses on the critical planes within the U10 gussets either were unchanged or benefited from a decrease in stress. Using the non-uniform temperature data provided by NTSB only produced marginal differences in member axial forces when compared to results from a uniform temperature change. Therefore, it can be concluded that temperature did not have a significant effect, if any, on buckling failure of the U10 gusset plate.

- The failure mode predicted by the detailed model was inelastic buckling of the gusset plates at the end of the compression diagonal in both the east and west U10 joints. The presence of initial bowing of the free edge of the gusset plates had a significant effect on the critical buckling load and the mode shape. Without accounting for the bowed edge each gusset side-sway buckled to the inside of the bridge. When an imperfection was added in accordance to photographic evidence, the failure mode of the U10 gusset plates changed to side-sway buckling to the west with significant lateral movement of the compression diagonal. This side sway mode resulted in a bent shape that is consistent with the damage patterns documented in the bridge wreckage. Therefore, there is a strong probability that the model is capturing the failure mode of the U10 gusset plates. In no case did failure occur at the L11 joint prior to buckling failure at U10. This strongly suggests that U10 was the primary point of failure and that any damage observed at the L11 joints occurred later in the collapse sequence.

- The magnitude of initial bowing in the U10 gusset plates has a significant effect on the critical buckling load predicted by the model. In all cases run, the model did not predict failure under the load conditions present at the time of collapse. The loads had to be proportionally increased until failure occurred. For the case where the dead load was proportionally increased, it took 1156, 701, 159, and 56 kip of additional load to get failure in the unbowed, 0.5, 0.7, and 0.75 inch imperfection models, respectively. Similar trends are observed when the traffic/construction loads are proportionally increased.

Since the margin of error for the known loads was determined in Chapter 2 to be about 300 kips, it can be concluded that the models with the 0.7 and 0.75 in. imperfection are providing plausible predictions of the critical buckling load. Photographic evidence shows that the U10 gusset plates had pre-existing imperfections prior to collapse measuring between 0.45 and 0.75 in. Therefore, the model did predict a failure mechanism significantly consistent with the physical evidence and within the resolution of the loads known to be on the bridge at the time of collapse provided the model included the documented imperfections in the gusset plates.

- The effect of corrosion section loss in the L11 joints was studied to determine if its presence altered the failure mode. A line of shell elements with 20% reduced thickness was added to the L11 gusset plates along a horizontal plane above the top edge of the bottom truss chord (A-A). This addition caused elevated stress levels in the reduced section but did not result in a completely yielded failure plane in the L11 gusset plates. The failure mode for the model was still inelastic buckling of the gusset plates at U10. Although failure of the A-A plane was observed in the bridge wreckage, the model results strongly suggest this was not the initial failure point for the bridge. Additionally, the presence of corrosion at L11 did not significantly alter the load needed to cause buckling at the U10 joints. Therefore it can be concluded that corrosion at L11 had no significant effect on the failure.

- The static finite element models used in this study terminated when the critical buckling load was reached in the U10 gusset plate. The final failure model was run beyond the critical buckling load using the RIKS algorithm to estimate post-peak behavior. The results show that the gusset plates probably jumped suddenly out-of-plane when the critical buckling load was reached. The results also show that the plates eventually stiffened and may have reached a second equilibrium state at a lower load level in their buckled condition. However, the stress and strain observed in the deformed plate exceeded the expected tensile capacity of the material. Therefore, it is likely that the gusset plate would have failed by tensile fracture prior to achieving post buckling equilibrium. This suggests that buckling of the gusset plates at U10 likely could have set off a more complex failure scenario involving large deformation and tensile rupture of the gusset plates.

CHAPTER 11. REFERENCES

1 Sverdrup & Parcel and Associates, Inc., “State of Minnesota Department of Highway Construction Plan for Bridge No. 9340 – Balance of Bridge and Approaches,” St. Louis, MO, Approved 15 June 1965.

2 Allied Structural Steel Company, “General Management Plan, Elevation, & Sections for Bridge No. 9340 Over the Mississippi River, Hammond, IN, Revised 24 March 1966.

3 Hall, D.H., Lawin, A.R., and Grubb, M.A., “Investigation of I-35W Deck Truss Bridge Collapse – Minneapolis, MN,” Bridge Software Development International, Ltd. (BSDI), Coopersburg, PA, March 2008.

4 Morrison, J,. Brazy, D., and Schultheisz, C., “*NTSB Report No. 07-115*,” National Transit Safety Board, Office of Research and Engineering, Materials Laboratory Division, Washington, D.C. November, 2007.

5 Graybeal, B.; “Mechanical Properties of the Minneapolis I-35W Bridge Deck and Pier Concrete,” FHWA Turner-Fairbank Highway Research Center, McLean, VA Feb. 2008.

6 O’Connell, H., Dexter, R., and Bergson, P., “Fatigue Evaluation of the Deck Truss of Bridge 9340, Report No. MN/RC – 2001-10,” University of Minnesota Department of Civil Engineering, Minneapolis, MN, March 2001.

7 http://ggweather.com/climate/extremes_us.htm, “United States Extreme Record Temperatures & Differenences,” accessed on 1 April 2008.

8 URS Corporation, “Fatigue Evaluation and Redundancy Analysis, Bridge No. 9340 I-35W over Mississippi River, Draft Report,” URS Corporation, Minneapolis, MN, July 2006

9 NTSB, “Structural Investigation Group Chairman Factual Report, Report No. 08-115,” National Transportation Safety Board, Washington D.C., March 5, 2008.

10 Email communication between Carl Schultheisz (NTSB) and Justin Ocel (PSI) on 22 September 2008.

CHAPTER 12. APPENDIX

Composite weight density of I35W deck slab
Sheet 56, lower right corner (**U8-U14, east side**)

Total Volume of Slab

$V_{total} := (2in + 2ft + 6in + 52ft + 2ft + 9in)\cdot 228ft\cdot 6.5in$ $\qquad V_{total} = 7.091\times 10^{3}\cdot ft^{3}$

No. 6 transverse top bars

$V_1 := 456\cdot\frac{\pi\cdot(0.75in)^2}{4}\cdot[(33ft + 5in) + (25ft + 2in)]$ $\qquad V_1 = 81.958\,ft^3$

No. 6 transverse bottom bars

$V_2 := 456\cdot\frac{\pi\cdot(0.75in)^2}{4}\cdot[(37ft + 6in) + (21ft + 1in)]$ $\qquad V_2 = 81.958\,ft^3$

No. 4 longitudinal top bars

$V_3 := \frac{\pi\cdot(0.5in)^2}{4}\cdot[56\cdot 7\cdot(33ft + 7in) + 55\cdot(2ft + 8in)]$ $\qquad V_3 = 18.151\cdot ft^3$

No. 5 longitudinal bottom bars

$V_4 := 72\cdot 6\cdot\frac{\pi\cdot(0.625in)^2}{4}\cdot(39ft + 3in)$ $\qquad V_4 = 36.125\,ft^3$

Volume of steel

$V_{steel} := V_1 + V_2 + V_3 + V_4$ $\qquad V_{steel} = 218.191\cdot ft^3$

Weight of steel

$W_{steel} := V_{steel}\cdot 490\frac{lb}{ft^3}$ $\qquad W_{steel} = 1.069\times 10^{5}\cdot lb$

Volume of concrete

$V_{conc} := V_{total} - V_{steel}$ $\qquad V_{conc} = 6.873\times 10^{3}\cdot ft^{3}$

Weight of concrete

$W_{conc} := V_{conc}\cdot 150\frac{lb}{ft^3}$ $\qquad W_{conc} = 1.031\times 10^{6}\cdot lb$

Composite Density

$\rho := \frac{W_{conc} + W_{steel}}{V_{total}}$ $\qquad \rho = 160.462\frac{lb}{ft^3}$

Composite weight density of I35W deck slab
Sheet 57, upper right corner (**U0'-U4', west side**)

Total Volume of Slab

$$V_{total} := (2in + 2ft + 6in + 52ft + 1ft + 3in)\cdot(150ft + 9.5in)\cdot 6.5in \qquad V_{total} = 4.567\times 10^{3}\cdot ft^{3}$$

No. 6 transverse top bars

$$V_1 := 299\cdot\frac{\pi\cdot(0.75in)^2}{4}\cdot[(33ft + 5in) + (25ft + 2in)] \qquad V_1 = 53.74\, ft^3$$

No. 6 transverse bottom bars

$$V_2 := 299\cdot\frac{\pi\cdot(0.75in)^2}{4}\cdot[(37ft + 6in) + (21ft + 1in)] \qquad V_2 = 53.74\, ft^3$$

No. 4 longitudinal top bars

$$V_3 := \frac{\pi\cdot(0.5in)^2}{4}\cdot[56\cdot 5\cdot(31ft + 1in) + 55\cdot(2ft + 8in)] \qquad V_3 = 12.067\, ft^3$$

No. 5 longitudinal bottom bars

$$V_4 := 72\cdot 4\cdot\frac{\pi\cdot(0.625in)^2}{4}\cdot(38ft + 10in) \qquad V_4 = 23.828\, ft^3$$

Volume of steel

$$V_{steel} := V_1 + V_2 + V_3 + V_4 \qquad V_{steel} = 143.375\, ft^3$$

Weight of steel

$$W_{steel} := V_{steel}\cdot 490\frac{lb}{ft^3} \qquad W_{steel} = 7.025\times 10^{4}\cdot lb$$

Volume of concrete

$$V_{conc} := V_{total} - V_{steel} \qquad V_{conc} = 4.424\times 10^{3}\cdot ft^{3}$$

Weight of concrete

$$W_{conc} := V_{conc}\cdot 150\frac{lb}{ft^3} \qquad W_{conc} = 6.636\times 10^{5}\cdot lb$$

Composite Density

$$\rho := \frac{W_{conc} + W_{steel}}{V_{total}} \qquad \rho = 160.673\frac{lb}{ft^3}$$

LOADING SCENARIO WITH TEMPORARY JERSEY BARRIERS

When the barriers were modified in the late 90's, temporary Jersey barrier had to be setup to protect worker while the modification were made. There were two rows of temporary barriers placed down the entire length of the deck truss positioned differently depending on the barrier being modified. The model was used to investigate the effects of this loading scenario on the U10 connection, specifically what loads are generated by the temporary barriers and if it caused any permanent deformation in the gusset plate.

Implementation

The model with the embedded U10 and L11 connection was used to investigate the effects. At the request of NTSB, the gusset plates were assigned imperfections in the same fashion as those described in Chapter 7, however the magnitude of the imperfection was only 0.05 inches. The step order was also modified because this scenario was meant to understand the effects of the modifying the barriers under construction, whereas in the previous analyses this was assumed to occur in one step.

Step one and two remained unchanged. Step three only applied the equivalent pressure loads to represent the increase in deck thickness. Step four altered the line loads for the inner barriers to reflect the newest design in addition to two additional line loads to represent the temporary Jersey barriers. Abaqus did not allow line loads to be specified onto interior deck shell elements to represent the temporary Jersey barriers. Instead, a pressure distribution was applied to a line of elements centered 125 inches from the centerline of the bridge. The pressure distribution had a magnitude to represent an equivalent line load of 392 lb/ft, the weight of the standard Mn/DOT temporary barrier. In step four, the loads for the temporary barrier on the inner-west lane was moved to the outer-west, centered 136 inches from the edge of the deck. In step six, the east-inner barriers were moved to their outer-east location. In addition, the exterior barrier line loads were altered to represent the modified design. In the final step, the temporary barriers are removed. These steps are schematically shown in Figure 78.

Results

Figure 79 plots the axial force history of the five members of the U10W connection through the seven step in this analysis. In this scenario, none of the member forces exceed their design capacities. Contrasting to the results shown in Figure 20 where the U10L9 member exceeded its design capacity under the construction/traffic loading scenario indicates that the Jersey barrier loading scenario was not as severe as the bridge saw on the day of the collapse.

Since the gusset plate was given an initial imperfection, a permanent deformation was expected after the Jersey barriers were removed. Once the temporary barriers were removed, the four gusset plates had an additional out-of-plane deformation of:

- 0.025 inches to the west for the U10W-W plate

- 0.029 inches to the west for the U10W-E plate
- 0.058 inches to the west for the U10E-W plate
- 0.041 inches to the west for the U10E-E plate

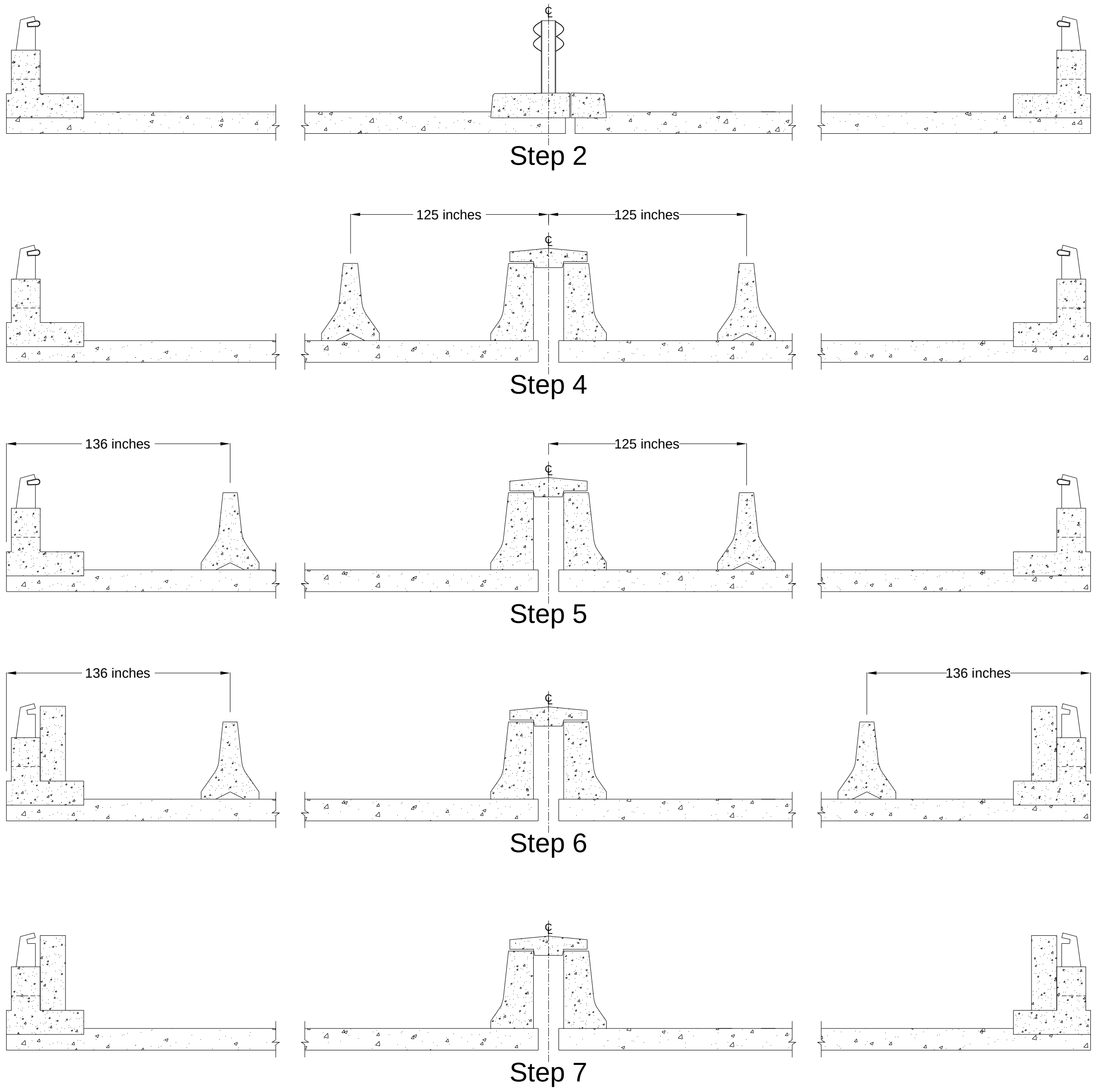

Figure 78. Schematic of loading steps for temporary barrier scenario. View looking North.

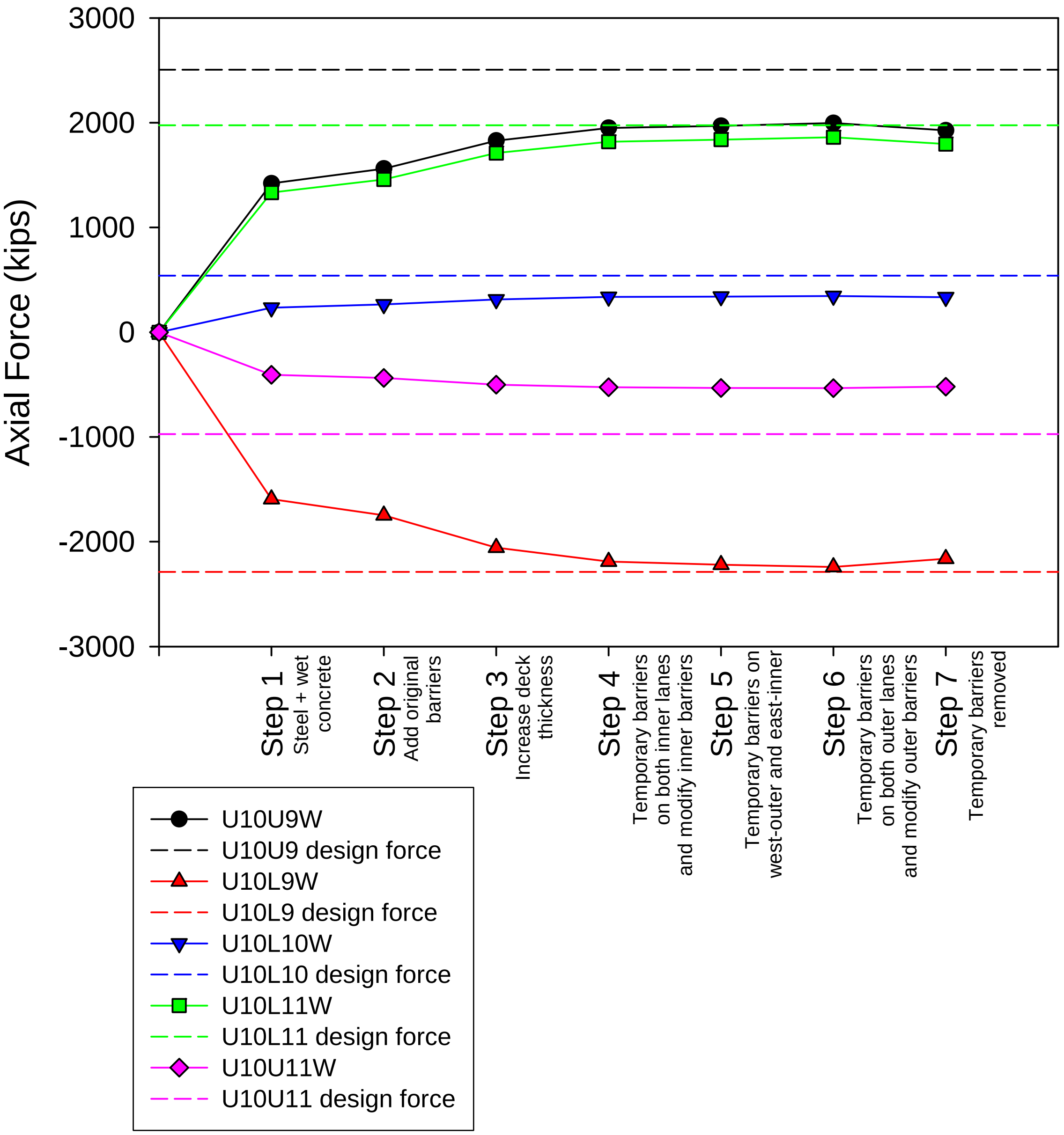

Figure 79. Force point traces of U10W member loads through temporary barrier load scenario.